THE SLURRY EROSIVE-CORROSIVE WEAR OF A SELECTION OF ALUMINIUM ALLOYS, PARTICULATE REINFORCED ALUMINIUM METAL MATRIX COMPOSITES AND A SELECTION OF STEELS.

by

J.A. Bester

A thesis submitted to the Faculty of Engineering, University of Cape Town, in fulfillment of the degree of Master of Science in Engineering.

Department of Materials Engineering
University of Cape Town

December 1992

ACKNOWLEDGEMENTS

I wish to thank all the people who assisted me in my research work and contributed to its final completion and in particular I am indebted to Professor A. Ball, my supervisor for his valuable advice and assistance during the research.

Messrs N. Dreze and G. Newins are thanked for their useful suggestions and technical assistance.

I am grateful to Messrs B. Greeves and J. Petersen for their photographic work.

Furthermore my fellow students are thanked for their interest and advice, in particular Marc Gammon and Scott Wilson.

Hulett Aluminium (Pty.) Ltd. is gratefully acknowledged for the provision of the material and research funding. In particular Dr.T. Hurd and Mr.B.I. Dennis are thanked for their support and interest.

Finally I thank my parents for their support and encouragement.

ABSTRACT

A range of aluminium alloys and particulate reinforced aluminium metal matrix composites has been tested in an apparatus which simulates the erosive-corrosive action of a slurry. The slurry consisted of silica sand suspended in either distilled water or synthetic mine water. Several steels were also tested in order to clarify certain concepts relating to the synergistic effects of erosion and corrosion.

In general both the heat-treatable and non heat-treatable aluminium alloys exhibit lower slurry erosion rates with increasing hardness and work to fracture values. The slurry erosion rates of the aluminium matrix alloys increas with increasing amounts of reinforcement particles.

For the steels a good work hardening capacity and/or high hardness values are found to promote good slurry erosion resistance. All the steels exhibit lower slurry erosion rates than the aluminium alloys.

A corrosion cell was developed to allow *in situ* electrochemical measurements to be made.

The addition of corrosive ions to the distilled water results in increased material removal rates, increasing by as much as 40% for some of the aluminium alloys and 41% for the 304 stainless steel.

The aluminium alloys and the steels which have increased corrosion resistance due to passivity, display poor performance under the slurry erosion-corrosion conditions tested. Paradoxically corrosion resistance was found to have a detrimental effect on the slurry erosion-corrosion resistance of a material.

CONTENTS

CHAPTER 1

INTRODUCTION

Slurry erosion concerns the removal of material by impingement of solid erodent particles suspended in a carrier fluid. Moving solids as a slurry is an efficient means of transport and is therefore widely used. In practise this occurs in the solid-liquid transport in pipelines in the mining, civil and chemical engineering industries, and the dredging of navigable rivers and water-coal slurry spraying in power generation industries. The movement of these slurries can cause significant erosion and corrosion, especially in positions where the slurry flow changes direction. Pumps, elbows, tee junctions and valves are only some of the parts in the systems that are subject to slurry erosion and corrosion. In a slurry, erosion is produced by the solid particles and corrosion may occur due to the liquid. These two factors may interact (synergism), to produce wear rates that are greater than the sum of their separate effects. This work concerns a materials ability to resist the synergistic action of slurry erosion and corrosion. Other factors that are also important for material selection in an engineering application, are cost, weight and ease of manufacture, namely castability, formability and machinability.

Aluminium is the most widely used non-ferrous metal in the engineering industry, owing to its attractive properties such as light weight, ductility, corrosion resistance, availability and low cost. However aluminium is soft and cannot be used to in applications involving tribological contacts[1], this has prompted research into the addition of ceramic reinforcement to enhance its mechanical properties.

The experimental work was performed to determine what effect material composition, the corrosion media and the impact angle has on slurry erosion performance. An attempt has been made to establish the mechanisms and factors which constitute the wear process in order to quantify their contributions. Thus the thesis examines the mechanisms of material removal by the slurry erosion as well as the synergistic effects of slurry erosion and corrosion of the aluminium alloys, the aluminium metal matrix composites and of the steels.

CHAPTER 2

LITERATURE SURVEY

The slurry erosion rate of a material is governed by a number of factors which control the micro-machining and micro-fracture processes. The following parameters are considered to be important for slurry erosive wear and will be considered in the following sections:

impact angle
erodent size, shape and properties
solid particle concentration in the liquid carrier
properties of the carrier fluid including corrosivity
mechanical and corrosion properties of the target material

2.1 Erosion Mechanisms

Three dominant mechanisms having been identified for material removal under gas/air borne solid particle erosion[2-47] :

microcutting (dominant for high angle erosion of ductile materials)

microploughing (dominant for low angle erosion of ductile materials)

microfracture (dominant for brittle materials)

Solid particle erosion theory assumes that for small impact angles ($\alpha \approx 30°$), erosion is due to a process of chip formation as a result of the microploughing action of the erodent particles. The mode by which erodent particles remove material from a ductile target surface involves the displacement of material from a damage crater produced by the impact event, i.e. ploughing. An impacting particle pushes material forward leaving a groove in its wake and a lip at the end of the groove when it leaves the impact site, this is shown schematically in fig. 2.1(a).

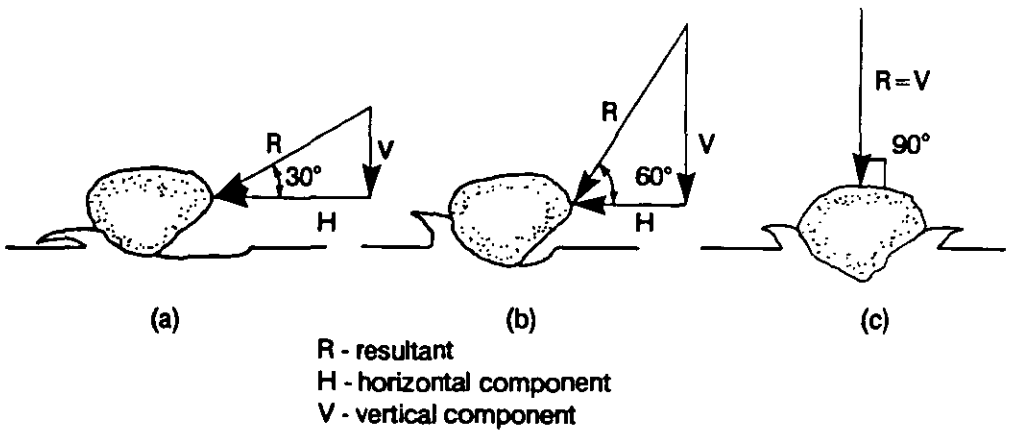

Figure 2.1 The effect of impact angle on the mode of material removal.

For large values of impact angle ($\alpha \approx 90°$), the mechanism of erosion ceases to be one of cutting and could be described as one of repeated impact wear. In the case of ductile materials plastic deformation usually results from the particles impacting the surface, fig. 2.1(c). When the impingement energy exceeds some limit, under steady state conditions, the surface layer is heavily deformed resulting in ductile microfractures. Further impacts of solid particles thereafter removes material.

For impact angles between ≈10° and 90°, both mechanisms contribute to the erosion process, fig. 2.1(b).

Another method of material removal is by repetitive-impact induced flake formation and the fatigue process of flake detachment by crack formation at their roots[38]. Hutchings[12] and Field[7] studied the detachment of crater lips in detail. They found that the lips are detached along localised adiabatic shear bands, formed beneath the surface near the lips. The formation of lips at the edges of impact craters, and their removal by other particles impacting nearby was also pointed out by Tilly[35].

The above models describe wear in gas-borne particle erosion but do not adequately explain erosion due to particles in a liquid carrier. Additional factors associated with liquid borne solid particle erosion are the deceleration of the particle near the target surface due to the viscosity of the liquid, the differences in heat transfer and corrosion processes[48-66].

2.2 Effect Of Erodent Size And Reinforcement On Erosion

It has generally been found for ductile metals that erosion rate increases with impacting particle size until some threshold particle size is reached. Further increases in particle size have no effect on erosion rate[67-76]. Typical threshold values are about 100μm and the threshold appears to increase with increasing velocity[73,9]. For a given mass of erodent striking a surface, as particle size increases fewer particles impact the target, but the total energy of the impacting erodent particles is independent of particle size. It is not obvious, therefore, why erosion rate should be affected the erodent diameter at all[82].

The energy absorbed by impacting particles is a function of size, and once a certain size is reached fragmentation of the erodent occurs; these fragments induce secondary damage as they are ejected, leading to additional erosion[9].

Although fragmentation of impacting particles is important in some erosive conditions, particle-size thresholds have been shown to occur in their absence[43].

Steady state airborne solid particle erosion rates were measured for pure aluminium and an Al-12wt.%Si eutectic alloy at an impact angle of 30°, by Hovis, Talia and Scattergood[70]. Norton E17 Al_2O_3 erodent particles, having mean diameters ranging from 63 μm to 406 μm, were used as erodent. Erodent particle velocities of 70m/s were achieved using an air stream apparatus. The erosion rates of the Al-12wt.%Si alloy was found to be significantly higher than those of pure aluminium under identical erosion conditions.

Material	*Steady state erosion rates ($\times 10^{-4}$ g/g) for the following erodent particle diameters*			
	406 μm	*266 μm*	*142 μm*	*63 μm*
Pure Al	2.77	2.49	2.60	1.91
Al-12wt%Si	3.45	3.01	2.80	1.70

Table 2.1 Steady state erosion rates for pure aluminium and the Al-12wt.%Si alloy, given as a function of erodent particle sizes in micrometers[70].

The data, presented in Table 2.1 , shows that as the erodent particle size decreases, the differences between the aluminium and the Al-12wt.%Si decrease until finally a cross-over point is reached at the smallest particle size. Hovis, Talia and Scattergood[70] inferred that the effect of erodent size must be partly related to the microstructural size scales.

The micromachining and chip fracture processes in the Al-12wt.%Si alloy should be less dominant as the impact crater size decreases and becomes comparable with the spacing between the silicon eutectic platelets. The silicon platelet size and spacing in the Al-12wt.%Si alloy were each about 3-5 μm, and for the conditions used the impact crater sizes were about one-tenth of the erodent particle sizes. For the smallest particle size of 63 μm the microstructural size scale was found to become comparable with the impact crater size[70]. For the Al-12wt.%Si alloy the silicon acts as an efficient chip breaker, which assists material removal, when the size and spacing of the eutectic silicon platelets are less than the impact crater size. The impact crater size depends primarily on factors such as the relative hardness of the target and the erodent and the kinetic energy of the impacting particle.

Since the indentation hardness of the alloy is about a factor of 3 greater than that of pure aluminium, this implies that the hardness, or flow stress, is itself insufficient as a measure of erosion resistance in this alloy system[70].

Even though the individual impact craters will be larger in pure aluminium than in the Al-12wt.%Si alloy mentioned above, for erosion, the material removal mechanism is less efficient in the pure aluminium. This is due to the difference in ductility or strain-to-fracture differences that occur between the pure aluminium and the Al-12wt.%Si alloy[70].

In pure aluminium the ductility is large and rather than a simple removal of a lip, or a micromachining chip, from an individual impact crater site, there is instead a refolding of the displaced material when subsequent particle impacts occur. Under steady state conditions this refolding process continues to accumulate strain (work hardens) and failure must finally result in the removal of material that has undergone sufficient prestrain, so that incipient displacement of a lip of material will exceed a critical (accumulated) fracture strain. The strain accumulation must persist as the erosion surface moves downward into the material and thus, in terms of energetics of the process, some of the incident particle energy will be consumed as a result of strain accumulation without material removal. For pure aluminium, it is also likely that dynamic recovery processes[71](quoted by Hovis, Talia and Scattergood[70]) will enhance the strain accumulation effects and reduce the efficiency of the material removal mechanism.

Scanning electron microscopy surveys were made by Hovis, Talia and Scattergood[70] of single-impact crater sites on both pure aluminium and Al-12wt.%Si alloy. While chip removal did appear more prevalent for the Al-12wt.%Si alloy, such single impact studies are not really conclusive unless considerable effort is spent in developing

statistical measurement and analysis techniques. Optical microscopy of cross sections were found to manifest the intrinsic differences in the steady state material response between pure aluminium and Al-12wt.%Si alloy more clearly[70].

The use of reinforcing particles is not always beneficial for the erosion resistance. Under some conditions it can increase the material loss compared with the unreinforced alloy, especially when reinforcement fracture occurs under high impact loads[77-108].

Metal matrix composites have been developed to yield superior mechanical properties. In general, metal-matrix composites erode more rapidly than do unreinforced metals, although differences in erosion rate are seldom more than about 50%[82]. Solid particle-erosion of 2014 Al has been studied by Wu, Goretta and Routbourt[82]. The alloy was either unreinforced or contained 20 vol.% particulate SiC or Al_2O_3. The materials were tested in the as cast, annealed, as-quenched and T6 heat-treated conditions. The erosion tests were conducted in an evacuated slinger-type apparatus [83]. Angular Al_2O_3 (Norton Alundum 38), with average particle size of 23, 42, 63, 143 or 390 μm, was used for most tests. For comparison, angular SiC (Norton Crystolon 37) was used for some tests. The erodent velocities were 50, 75, or 100 m/s and the impact angles ranged from 10-90°. No incubation period was observed for any of the MMCs tested under the above conditions. The matrix alloys also exhibited little or no transient response at low angles of incidence. For normal incidence, however, the specimens gained mass initially because of imbedding of the erodent. Embedding was least severe for the T6 heat treated specimens. This effect of angle of impact was similar for all combinations of impact velocity and erodent particle size. For the aluminium matrix alloys, under every set of conditions, the maximum erosion rate was at the 15° impact angle and the minimum rate was at 90°. For the MMCs, the maximum erosion rate occurred from 15° to 30°, with the maximum for impact by smaller particles tending to occur at 15°. The minimum was always at 90°. The composites eroded more rapidly than the matrix alloys under all conditions.

Wu *et al.*[82] explained that since each of the materials exhibited maximum erosion at oblique incidence and minimum erosion at normal incidence, then the erosion of each material is due to ductile mechanisms. The differences in erosion response are attributed to details of microstructure and mechanical properties. For metals, shifting of erosion maxima to higher angles has been ascribed to decreases in ductility[79]. Aluminium metal matrix composites generally have much lower ductilities than the unreinforced alloys[107]; heat treating to the T6 condition reduces the ductility even further. The shifting of the maximum erosion rate to higher angles for the

composites, with a more pronounced shift for the heat-treated specimens, is consistent with the relative ductilities. Although the target ductility plays an important role in erosion, hardness is also important. Hardness and ductility are inversely related in most metals and it is generally not possible to optimise both properties simultaneously. It was therefore proposed that the erosion data presented can be analysed in terms of these competing factors: ductility decreases caused by hardness increases[82].

The erosion rates of the Aluminium-SiC and Aluminium-Al_2O_3 composites were virtually the same. Erosion rates of monolithic SiC and Al_2O_3 can vary by a factor of approximately five. It appears, therefore, that the erosion rate of aluminium metal matrix composites will not be strongly influenced by the composition of the particulate ceramic reinforcement.

Wu *et al.*[82] concluded that the reinforcement phase should be well dispersed and should not have sharp edges. The composition of the reinforcement is of secondary importance. Especially for erosion at normal incidence ductility appears to be more important to erosion resistance than does the strength and should be maximised. Abrasive shape affected material removal in that the flat abrasives induced less wastage.

Two mechanisms have been identified for the slurry erosion of particulate-reinforced aluminium alloys by Christman and Shewmon[69]:

(1) For small impingement angles (fig. 2.2), only part of the matrix is exposed to incident erodent particles.

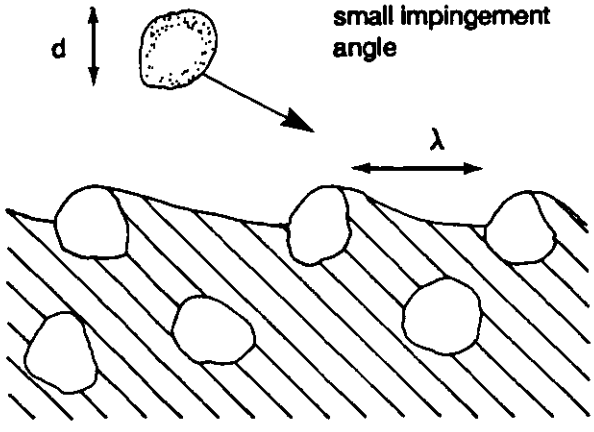

Figure 2.2 For small impingement angles, during slurry erosion of the particulate-reinforced metal matrix, the protection effect, gives rise to protruding particles. (after Christman and Shewmon[69])

This phenomenon corresponds to the case where the mean free path (λ) between the reinforcing particles is much larger than the damage (or crater) size produced by a single erodent particle. This allows the usual cutting mechanism, for ductile materials to take place[69].

The slurry erosion associated with the protection effect results in protruding particles on the worn surface, (fig. 2.2).

(2) If the impacting particles have sufficient energy, particularly for large impact angles, fracture of the reinforcing particles can occur, which is detrimental from a slurry erosion resistance point of view, fig. 2.3.

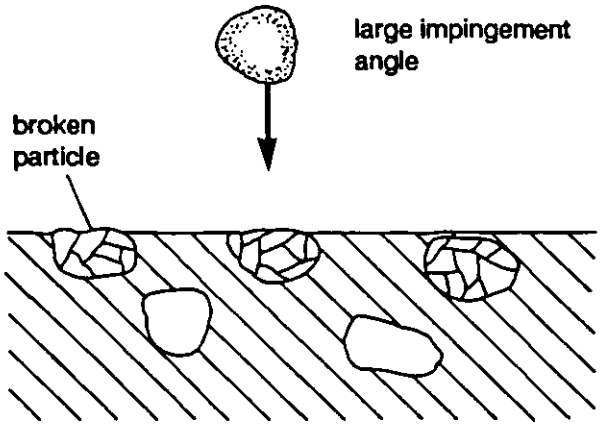

Figure 2.3 For large impingement angles during slurry erosion, coupled with sufficient erodent mass, fracture of the reinforcing particles in the particulate-reinforced metal matrix occurs. (after Christman and Shewmon[69])

The fracture of the reinforcing particles eliminates the presence of protruding particles. The wear of the entire surface is then uniform with the same slurry erosion rate for the particles and the matrix. This results in an even surface free from protruding particles[69].

It can be seen from the curves in fig. 2.4 that reinforcing particles improve the wear resistance of the aluminium alloy (5083 as received) except for slurry erosion at 90° with coarse erodent. This was been shown to be due to the fracture of the reinforcing particles[69].

There is an absence of a maximum in the curves for the MMC. The absence can be attributed to the inhibition in the cutting process of the material. The maximum found in the case of ductile materials is associated with the high efficiency in the cutting mechanism related to a small impact angle[69].

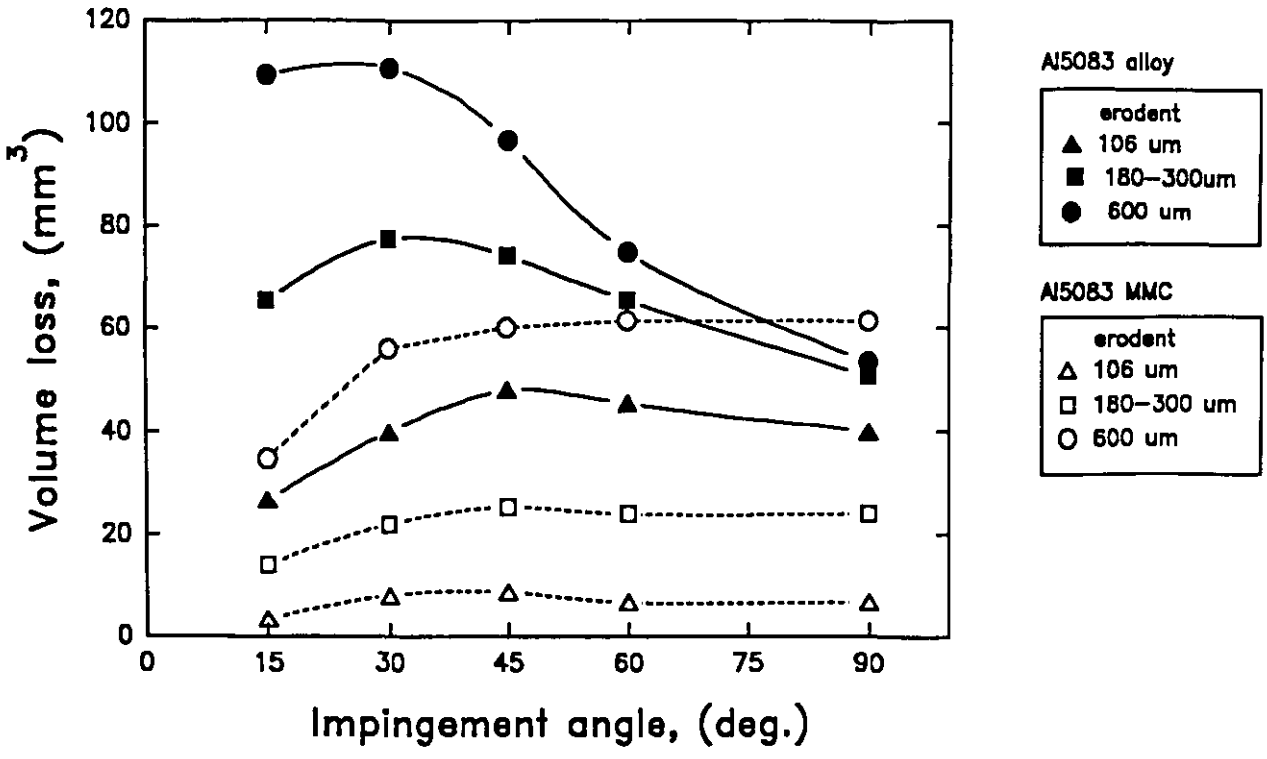

Figure 2.4 Slurry erosion wear of aluminium alloy 5083 and a 35vol.% of 180 μm alumina particulate-reinforced aluminium 5083 alloy as a function of the impingement angle of the slurry jet. The slurry velocity was 15m/s and the silica erodent concentration was 10wt.% for all 3 erodent sizes used. (after Christman and Shewmon[69])

2.3 Carrier Fluid

A study was made by Zu[65,66] to compare the differences between aqueous slurry erosion and airborne solid particle erosion, under the same conditions. Zu found that a heterogeneous surface composite layer, due to embedment of fine silica erodent particle fragments in the aluminium surface, only forms during airborne solid particle erosion. The slurry erosion surface being free from embedment. This led Zu to the conclusion that a fluid cleaning effect must be operative during slurry erosion. The fluid washes debris of detached target material away before they can be reattached onto the target surface by subsequent impacting particles. Water also washes broken fragments of erodent particles away preventing adhesion and embedment[65,66].

The surface composite layer that formed under the airborne erosion conditions resulted in a surface layer that was harder than that formed during slurry erosion. This difference in hardness was partly accounted for by the higher erosion resistance shown by the aluminium specimens subjected to airborne erosion[65,66], (fig. 2.5). The

steady state mass loss is reached only when the rate of adhesion and embedment is surpassed by material removal caused by airborne impacting particles.

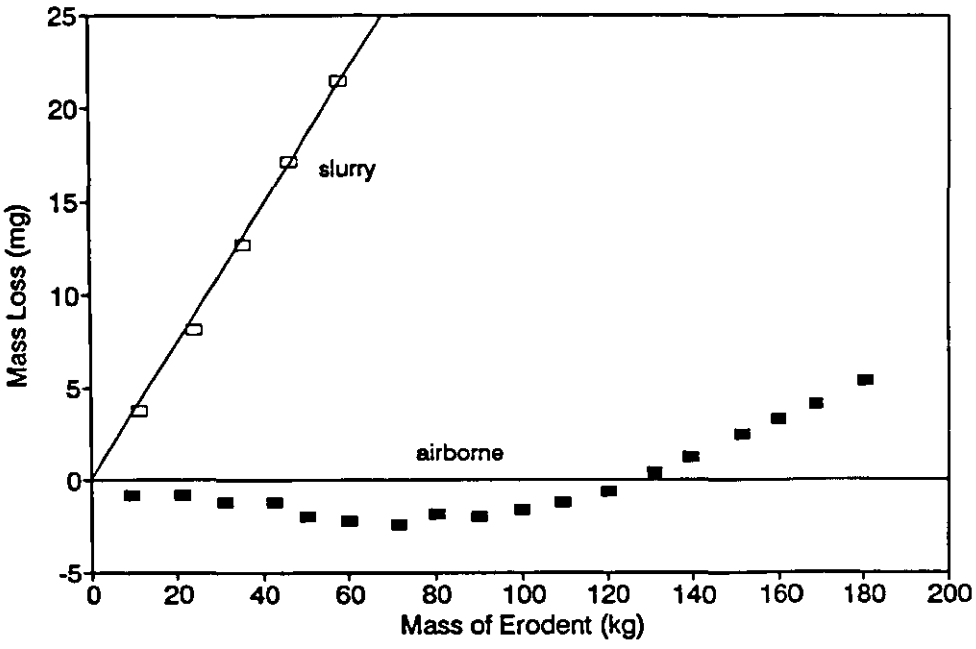

Figure 2.5 Erosion wear of an aluminium alloy as a function of mass of erodent used. Both the slurry and airborne particle velocities were 4.5m/s, the mean silica sand erodent particle diameters being 700 μm. An impact angle of 40° was used. (after Zu[66])

It is not noted by Zu[65,66] that another factor why embedment under slurry erosion conditions is less likely, is because the fluid greatly reduces the velocity of the erodent particles near the surface and hence the kinetic energy of the particles on impacting the surface. The prevention of embedment, due to the fluid protection effect in slurry erosion is probably the reason why there is an incubation period only under the airborne erosion conditions.

The fluid dynamic forces acting on the erodent particles due to the flow patterns over the target also affects the actual impact angle. When a fluid jet impacts on a flat surface, the jet will spread out along the surface. In the air solid-particle erosion, the direction of the erodent will not be affected by the spreading the air 'jet' because the viscosity of air is very small. In slurry erosion however, the direction of the erodent will be the direction of the flow because of the large viscosity of the liquid. With a slurry jet the majority of the particles impact the target at oblique angles. For ductile materials the erosion rates are greater at oblique angles. This should account for the greater erosion rate observed for slurry erosion, as compared with airborne erosion, by Zu[65,66] for the ductile aluminium.

2.4 Corrosion of Aluminium and Aluminium MMCs

According to thermodynamics, aluminium should be a reactive metal, with low corrosion resistance. Also aluminium is one of the least noble of the common commercial metals. It is remarkably stable in many oxidising environments. It owes its stability and resistance to many environments to the continuous, thin, compact film of adherent aluminium oxide film that rapidly grows on the nascent aluminium surface that is exposed to oxygen, water or to the oxidants. Whenever a fresh aluminium surface is created and exposed to either air or water, a surface film of aluminium oxide forms at once and grows rapidly[84]. The normal surface film present in air is about 5 nm thick.

The composition of microconstituents, their size, quantity, location, continuity and corrosion potential relative to that of the adjacent aluminium solid solution matrix, are the important aspects of microstructure that affect corrosion behaviour[100] (as referenced by Hatch[84]).

Meyer-Rodenbeck, Hurd and Ball[109] found that pitting with low volume losses and corrosion rates occurs for the unreinforced aluminium alloys 1200, 3004, 5083, 6261 and 7017 due to small localised differences in electrode potential at constituent sites. Synthetic mine water, detailed in Table 2.3, was used for the corrosive medium.

pH	*5.7*
sulphates chlorides	715ppm 350ppm

Table 2.3 Corrosive synthetic mine water solution based on an analysis of mine water[110].

Chlorine and other halogens are probably the most aggressive elements in their tendency to cause corrosion of alloys at both low and high temperatures[85].

Galvanic corrosion is characteristic of MMCs since the mismatch of the electrochemical potential between the matrix and reinforcement provides a local cell if they are immersed in an aqueous solution[89-94].

In general, MMCs can be more susceptible to corrosion than the unreinforced alloy as a result of the galvanic coupling, selective corrosion in the interfacial region, from crevice corrosion when gaps exist in the interfacial region and from MMC defects such as voids[99].

Thermal problems have a detrimental effect on MMC properties because both the particulates and the aluminium alloy posses different thermal properties. This

difference may result in high residual stresses and high dislocation densities at the interfaces after heat treating cycles which may affect both the kinetics of corrosion[99,93].

2.5 Slurry Erosion-Corrosion

The the effect of corrosion on mechanical wear rates has been studied by a number of researchers[116-156] and it is generally agreed that the synergism between the erosion and corrosion is very important in regard to the slurry wear rates of metal alloys. The processes governing material wastage are however still poorly understood.

Erosion-corrosion may be referred to as a conjoint action involving corrosion and erosion in the presence of a corrosive substance. Wood and Hutton[156] proposed that the synergistic effect of erosion and corrosion can be analysed by following an experimental programme which includes three types of test: (1) pure erosion tests to determine the erosive wear rate; (2) pure corrosion tests to determine the corrosive wear rate; (3) combined tests to determine the total wear rate when conditions in both test(1) and test(2) are acting. These experiments allow evaluation of the synergistic effect by using the equation.

$$S = T - (E + C) \tag{2.1}$$

where S is the synergistic wear rate, T the total wear rate, E the erosive wear rate and C the corrosive wear rate.

Wood *et al.*[156] used their equation to analyse results taken from the literature. The results of aqueous slurries containing 2% silica sand particles eroding various steels in a slurry pot[142] and of vibratory-type silica-sand slurry impingement in various corrosive solutions[146] were analysed. Wood *et al.*[156] explained that the synergistic mechanism is one of erosion-enhanced corrosion. The effect of erosion being to mechanically remove the corrosion product from the surface, by solid particle impact, generating fresh highly reactive surfaces. Wood *et al.*[156] also proposed that the fatigue strength of the target metal is lowered by corrosion. Further possible corrosion-enhanced mechanisms postulated are, the removal of work-hardened surfaces by corrosion exposing the softer base material to erosion mechanisms, the preferential attack at grain boundaries resulting in grain loosening and the increase in the number of stress-concentrating defects resulting from corrosion micropitting[156].

In the work by Madsen[142] a slurry test was developed for the measurement of wear rates and electrochemical corrosion rates during slurry wear in order to establish relationships between erosion and corrosion of metal specimens. Slurries of silica sand and aqueous solutions were continuously fed into the slurry pot test chamber, where they abraded and corroded the test specimens, a low alloy steel, a stainless steel and a wear-resistant low alloy steel. The test parameters were temperature, solids concentration and impeller speed. The test results showed that the combined effects of erosion and corrosion resulted in total wear rates that were much greater than the additive effects of each process taken alone, thus showing a strong synergism between erosion and corrosion[142].

When the total wear rates of the three materials tested by Madsen[142] where compared it was evident that the wear-resistant alloy REM 500 was more wear resistant than either the A514 steel or the 316 stainless steel under all test conditions. This was ascribed to the high hardness of REM 500, namely 496HV as compared with 284HV and 128HV for the A514 steel and the 316 stainless steel respectively.

When the 316 stainless steel was subjected to the erosive slurry, its electrochemical corrosion rate was much greater than its corrosion rate when no solids where present. The removal of the chromium oxide film is believed by Madsen[142] to be responsible this phenomenon. Anodic passivation of the wear surface was experienced to some extent under all the test conditions and an increase in the passivation current density resulted when the temperature, per cent solids or impeller speed was increased[142].

The corrosion rates of the A514 and the REM 500 steels were only moderately affected by the amount of solids in the slurry. The results indicated that oxidation products from both these alloys did not result in passivation. The synergism between the erosion and corrosion components of wear was found to account for one-third to nearly to nearly two-thirds of the wear[142].

A pilot investigation on the wear of grinding balls in a tumbling mill indicated that in wet conditions, the corrosive wear is not a simple addition of dry wear and corrosion[129]. Investigations by El-Raghy, Abd-El-Kader and Abou-El-Hassan[130], have shown higher amounts of dissolution, with higher current densities being observed on the abraded metal surfaces. In their experimental work a low-alloy steel (see Table A.1), was worn with grinding paper immersed in 1%NaCl aqueous solution. At a potential of -700 mV (SCE) (sufficient to bring about cathodic protection of the specimen) the amount of dissolution was only 10% of the mass loss but at -400 mV (SCE) it was 54%, associated with an increase in the total mass loss.

Abrasion corrosion was found to be a joint effect of mechanical forces and electrochemical processes at a newly generated metallic surface[130].

For sliding wear the amount of dissolution was found to be about 50% by Lazarev, Charlamova and Vevejkin[138] (quoted by Wandke, Möser and Tscherny [155]).

Burstein, Ashley and Marshall[124] conducted experiments not only aimed at producing a qualitative picture of the types of reactions occurring during the mechanical disruption of a metal surface in aqueous solutions, but also to quantify the rates at which they occur.

Wandke, Möser and Tscherny[155] showed that mass loss due to corrosion was less than 2% of the total. Their electrochemical investigations were carried out on 'unalloyed steel ST 38' and the high-alloyed stainless steel X8 CrNiTi 18.10 (AISI 304), using a solution of 0.1N H_2SO_4 with 0.1N Na_2SO_4 as electrolyte.

Under erosive-corrosive slurry conditions, the mechanical damage may be restricted to surface layers or to both surface layers and base metal[134], depending on the energy and/or frequency of the particles hitting the surface. Heitz[134] has distinguished three cases of increasing energy or frequency of the particles hitting the surface, these are illustrated in fig. 2.6.

(1) The particle energy is too small to damage even the passive layer of the passivated metal or the impact events are too rare to have a measurable effect on the slurry erosion rate.

(2) The particle energy is sufficient to account for damage to the passive or other surface layers and to deform the outer regions of the base metal mechanically. The activated surface of the metal corrodes in the presence of aggressive agents. Erosive wear and corrosion rates are of the same magnitude. Damage and healing kinetics of passive or other layers are involved. In materials with two-phase structures (e.g. hardened alloys with chromium carbides), local corrosion on a micro scale is observed.

(3) The particle energy is so great that the base metal is preferentially eroded and the attack is mainly erosive wear.

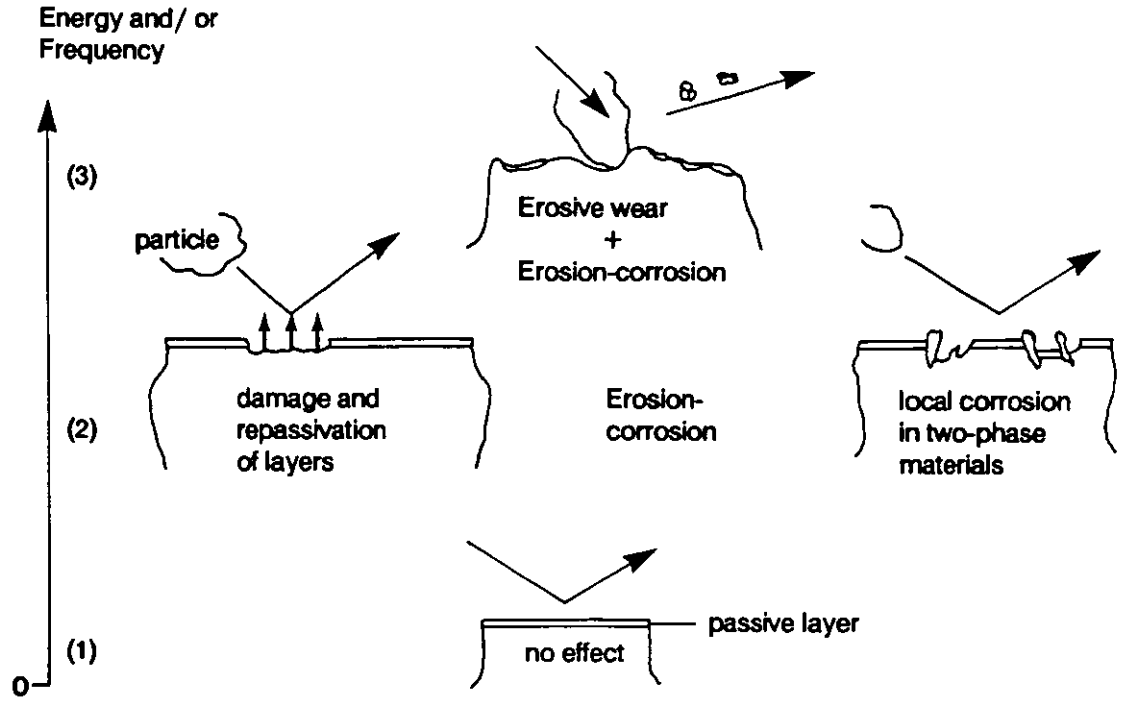

Figure 2.6 Chemo-mechanical effects of a particle impact on a metal surface. (after Heitz[134])

In a study of the corrosion of 5456-H117 aluminium (see Table A.2), in high velocity sea water, Gehring and Peterson[132] found that the removal or disruption of the oxide film is a primary factor affecting both the mode and rate of corrosion. They observed that at low velocities where the oxide layer is stable, corrosion appears to proceed in the classical manner generally acknowledged for aluminium alloys in sea water. At higher velocities, however, the oxide layers become unstable and corrosion increases sharply while changing from a macropitting mode to a micropitting mode.

When wear occurs in a corrosive environment, accelerated corrosion takes place at the wear sites[116]. This is likely to happen particularly in the case of those metals and alloys that depend on the existence of a passive film for their corrosion resistance, for example, stainless steels and aluminium alloys. If the wear is continuous or nearly so, repassivation may be difficult and active/passive cells will enhance metal degradation[116]. In the work conducted by Abuzriba, Dodd, Worzala and Conrad[116], on an apparatus that permits the separation of the wear and corrosion components of wear corrosion, a loaded ruby ball was used to describe a circular track on a sheet specimen in a corrosive environment, with and without cathodic protection applied to the specimen to produce wear and wear corrosion respectively. Preliminary results

on type 304 stainless steel demonstrated that corrosive-wear removed approximately 2.5 times as much material as wear alone under cathodic protection.

Postlethwaite and co-workers[148-151] investigated the corrosion-erosion in slurry pipelines made of carbon steel. They concluded that the presence of solids can bring about a sharp increase in metal wastage, and that the effect is dependent on the concentration of solids and the slurry velocity. An explanation for this effect is given in terms of the erosive disruption of surface films, which normally hinders the diffusion of oxygen to the corroding surface.

Postlethwaite[148] used both weight loss and electrochemical measurements to study the effects of chromate($K_2Cr_2O_7$) inhibitor on the erosion-corrosion of carbon steel specimens in a 5 cm diameter slurry pipeline carrying a 20 vol.% aqueous slurry of silica sand (size range 0.3 to 0.6 mm) over a velocity range 2-3.5 m/s. In the absence of inhibitors the total wear rate of a 5 cm long x 1 cm wide specimen located at the 4 o'clock position in the pipe wall was 2.7 to 17.5 mm/year. In the presence of inhibitor, the wear rate was reduced to values in the range 0.48 to 0.82 mm/year. The electrochemical measurements showed that erosion was the major mode of metal loss. However, there is a major interaction between the erosion and the corrosion components and a reduction in the corrosion component, which leads to much smoother surfaces, resulting in greatly reduced erosion losses. It was proposed, based on the state of the surfaces following the tests, that the large reduction in the mechanical wear experienced relates to the much smoother surfaces formed when the corrosion component is eliminated or greatly reduced.

In a paper on the cavitation erosion and corrosion of cast iron under cavitation conditions Tomlinson and Talks[154] discuss wear damage in terms of the erosion, corrosion and corrosion-induced erosion of the cavitation damage. In a range of cast irons in various metallurgical conditions, Tomlinson *et al.*[154] showed that a fraction, 0.05 of the damage arises from the electrochemical corrosion and that typically a fraction 0.70-0.85 of the damage arises from corrosion-induced erosion. Blount, Moule and Tomlinson[120] showed that the synergistic effect of cavitation and corrosion is greater than their separate actions.

2.6 Hydrogen Embrittlement

Wandke, Möser and Tscherny[155] showed that mass loss for 'blast wear', in the presence of an aqueous medium, significantly increases when the samples are charged with hydrogen before and/or during blasting. Cathodic protection was found to be ineffective[155] due to the generation of hydrogen on the metal surface. It

is suggested by that hydrogen uptake is the result of tribosorption processes at the impact sites. The conversion of kinetic energy into deformation work (*i.e.* heat) should produce locally such high temperatures that hydrogen is thermally dissociated. The hydrogen atoms are then swept into the lattice by dislocations[155].

Hydrogen, as the lightest element, has the smallest atomic diameter, nearly 0.1 nm. As a consequence, atomic hydrogen easily enters the metal lattice where it has a high mobility. This is especially true for ferritic steels owing to their b.c.c. lattice. In the more closely packed f.c.c. lattice of austenitic (Cr-Ni) steels, the diffusion coefficient is nearly four orders of magnitude smaller than for ferritic steels[87,88] which generally results in a lower susceptibility to hydrogen in the temperature range below 80°C[155].

2.7 Effect Of Target Material Properties

"One of the most striking features of erosive wear is the lack of influence of conventional metallurgical strengthening mechanisms on the resistance of metal to erosion"[12].

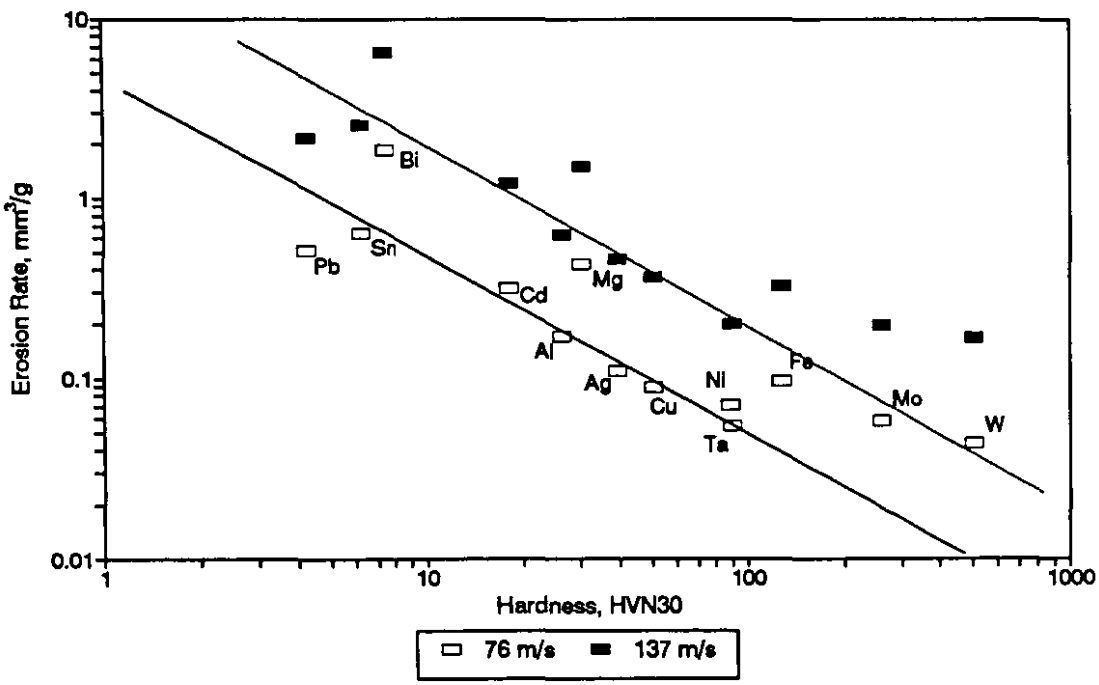

Figure 2.7 Volume removal as a function of VHN for the metals eroded at an impingement angle of 20° and velocities of 76 and 137 m/s. All the metals except cadmium were in the annealed condition. (after Finnie, Wolak and Kabil[159]).

Various physical parameters have been suggested in order to predict the ability of metals to withstand erosion due to solid particle impingement[158]. Finnie, Wolak and

Kabil[159] have shown that erosion varies inversely with indentation hardness, for many, although not all, pure metals (fig. 2.7).

Vijh[160] has demonstrated a similar correlation with metal-metal bond energy. In addition, an approximate relationship has been shown to exist between erosion resistance and melting temperature[161]. Notwithstanding temperature increases due to frictional heating and adiabatic effects, Rickerby[158] proposes that erosion remains essentially a mechanical process governed by local deformation and removal of surface material. It appears reasonable to therefore to look for a correlation between erosion and mechanical properties[158].

2.7.1 Hardness

McCabe, Sargent and Conrad[162] studied the erosion of two high carbon steels which were heat treated to obtain spheroidised, pearlitic, martensitic and tempered martensitic structures. The two steels tested were a hypereutectoid steel (AISI - SAE 10105) and a steel close to the eutectoid composition(AISI - SAE 1078) . Alumina particles of 240 mesh size were used as erodent in a sand-blasting type of erosion tester. The tests revealed a general trend of decreasing erosion resistance with increasing hardness of the microstructure, at an angle of 90° and a velocity of 99 m/s, (fig. 2.8).

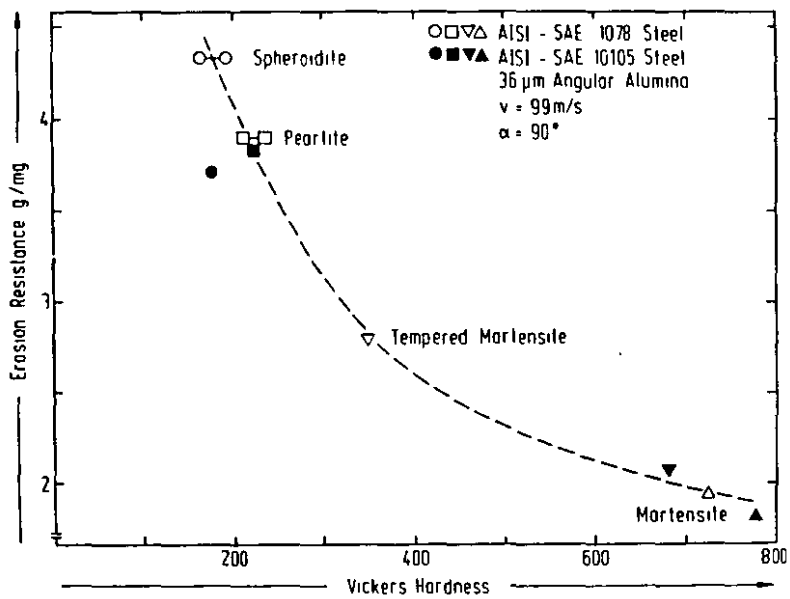

Figure 2.8 Airborne erosion resistance at an impingement angle of 90° of different structures of the steels AISI-SAE 1078 and 10105 as a function of hardness. (after McCabe, Sargent and Conrad[162]).

The work of Brass[163] (as referred to by Hutchings[12]) was specifically directed towards examining this effect and demonstrated that the erosion rates of an aluminium copper alloy and a carbon steel did not correlate with hardness measurements and varied only slightly despite major microstructural changes induced by thermal treatment. Similar conclusions have been pointed out by Sheldon[164].

2.7.2 Work Hardening Capacity

During erosive wear, localised regions on the metal surface experience high stresses, strains and strain rates. The ability of a material to withstand strain and to resist microfracture is influenced by strain hardening capacity. Ball[165,166] discusses the interaction of abrasive wear and strain-hardening for different classes of materials. Figure 2.9 shows the stress strain curves and a basic model of the wear behaviour of Materials I, II and III.

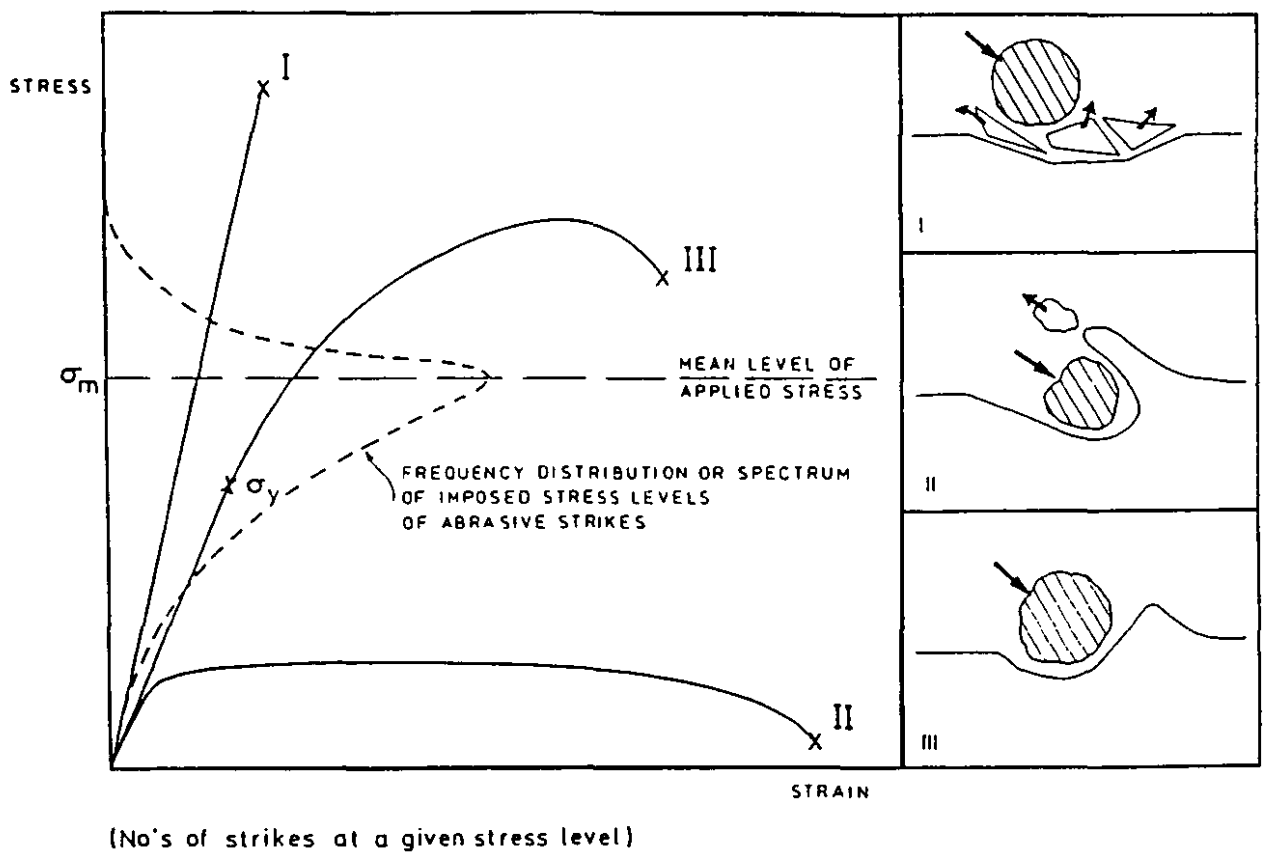

Figure 2.9 Hypothetical stress-strain wear curves for hard, brittle material (I), a soft, ductile material (II) and a material that has a capacity to strain-harden and resists brittle fracture(III). (after Ball[166])

Stress strain curve I is representative of hard brittle solids. During abrasive wear microfracture is initiated by small defects in the material and low resistance to crack propagation of the microstructure results in high wear losses.

Material II represents soft, ductile metals. The mean level of stress (σ_m) associated with abrasive wear is such that critical stresses and strains required for microfracture are easily achieved and wear loss occurs by ductile cutting. These materials have poor wear resistance.

The rapidly rising stress-strain curve of material III indicates a good combination of strength and strain-hardening capacity. In this case, abrasive stress levels are such that localised regions on the metal surface accumulate strain and become work hardened. Strength-and-hardness increases through work hardening also affords a degree of toughness and in effect a higher resistance to wear is achieved.

2.7.3 Work To Fracture

The mechanical energy density required to cause failure in a tensile test is equivalent to ρW, the work done per unit volume, and corresponds to the area under the stress-strain curve. An approximate estimation of this quantity can be made using[167]

$$\rho W = \tfrac{1}{2}(\sigma_y + \sigma_u)\epsilon_f \qquad (2.2)$$

where σ_y is the yield stress, σ_u is the ultimate tensile stress and ϵ_f is the strain at failure.

Erosion rate data for a number of annealed metals, at two different impingement velocities, were plotted by Rickerby[158] against the mechanical energy density, or work to fracture, (fig. 2.10).

The experimental values where taken from the work of Finnie *et al.*[159] and where calculated from equation (2.2) by Rickerby[158]. Mechanical properties were obtained from published tabulations [168-170] and are tabulated in Table A.3 in the Appendix. An inverse relationship between volume erosion and the work to fracture is evident.

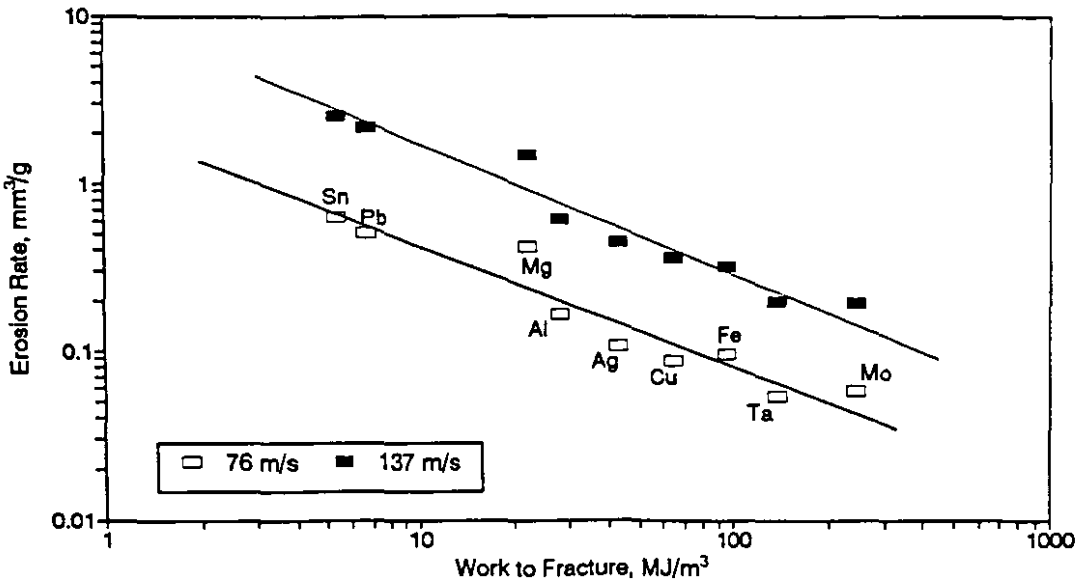

Figure 2.10 Correlation between erosion rate at impingement velocities of 76 and 136 m/s with work to fracture values for tensile failure. (after Rickerby[158])

2.8 Ripple Formation

The ripple structure in ductile unreinforced materials has been widely observed for erosion at low impact angles[52]. It occurs for all erodent particle sizes, although it has a shorter wavelength and smaller amplitude as the particle size decreases at fixed particle velocity[66].

Though a ripple-covered erosion surface of plate glass (a nominally brittle material) has been reported by Sheldon *et al.*[164,31], Finnie[8] and Ruff and Wiederhorn[29], reports of surface ripples on brittle materials are very rare. This is presumably because extensive plasticity is involved in the ripple formation mechanism.

The extensive folding and lateral displacement of material is evident in the erosion of pure aluminium as observed by Hovis, Talia and Scattergood[70]. Subsurface bands result from the folding and refolding of material onto itself as erosion progresses. Subsurface cavities and embedded Al_2O_3 fragments were also observed[66]. Embedded erodent particle fragments are commonly observed in ductile materials under airborne solid particle erosion.

The extensive folding of material in pure aluminium samples is also reflected in the fact that the ripple structure is dynamic and moves in a downstream direction during erosion, with the breaking and reforming of individual ripple lines[66].

CHAPTER 3

MATERIALS EVALUATED

A range of materials were tested, these include most of the major classes of wrought aluminium alloys, aluminium metal matrix composites, mild steel, stainless steels, a corrosion resistant steel and heat treated medium carbon steel. All the materials tested are listed below with the condition they were tested in.

Unreinforced Aluminium alloys

	Fabrication Route	Temper Designation
1070	Cast	
1200	R	H2
2014	E	T6
3004	R	H2
5083	R	H2
6061	E	T6
6261	E	T6
7017	R	T6
7075	R	T6

Matrix Al Alloys	Reinforcements	
6061	15vol.%.Al_2O_3	T6
	20vol.%.Al_2O_3	T6
2014	15vol.%.Al_2O_3	T6
	20vol.%.Al_2O_3	T6

Temper Designations
T6 - solution heat-treated and then artificially aged
H2 - strain-hardened then partially annealed.

Fabrication Routes
R - rolled
E - extruded

Steels

	Heat Treatment
304SS	Solution Treated
431SS	Annealed
3CR12	Tempered
EN3B (Mild Steel)	Normalised
EN8	Spheroidised
EN8	Tempered
EN8	Quenched

The chemical compositions of all the materials tested are tabulated in the Appendix, see Tables A.7 to A.12.

3.1 Test Specimens

Sample discs 4mm thick and 15.7mm in diameter were machined for the various alloys to be tested. The specimens were cut so that the surface to be exposed to the slurry jet is parallel to the rolling direction or extrusion direction, depending on the manufacturing route, see fig. 3.1.

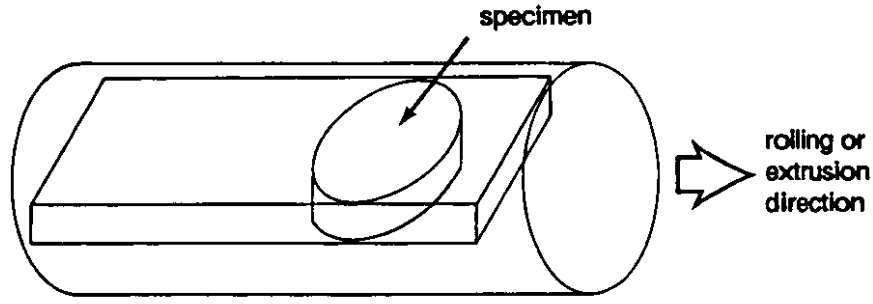

Figure 3.1 Diagrammatic representation of sampling technique.

3.2 Mechanical and Physical Properties

Vickers hardness values were obtained, using a 20kg load for the aluminium based materials and a 30kg load for the steels, in order to facilitate comparisons between hardness and slurry erosion resistance.

Values for material density was determined by weighing specimens to find their various masses and then dividing by their respective volumes, found by measuring their dimensions.

Charpy-V-notch impact tests have been made undertaken in order to obtain a measure of material toughness at high strain rates according to BS131:1972 (striking velocity 5m/s, room temperature).

Tensile tests have been conducted on the aluminium alloys, the results being manipulated to yield work to fracture values. The values represent the amount of energy that can be imparted to a volume of material before fracture will occur. The units are given as MJ/m^3 since the values are obtained by calculating the area under the load *vs.* strain curves.

The results of the above tests are tabulated in the Appendix.

3.3 Examination Techniques

3.3.1 Microscopy

Polishing and etching of the aluminium alloys, MMCs and steels was done using conventional polishing equipment in order to facilitate optical metallography. Micrographs were taken at 400, 200 and 100 times magnification using an optical microscope.

3.4 Microstructures of the Aluminium Matrix Alloys

Wrought aluminium alloys are divided into seven major classes according to their principal alloying elements. Each class represents a different class of microstructure because of these alloy differences. Furthermore, alloy classes can be divided into two categories according to whether they are strengthened by work hardening only or by heat treatment (precipitation hardening). The former applies to 1XXX, 3XXX, 4XXX and 5XXX alloys, while the latter applies to 2XXX, 6XXX and 7XXX alloys. Two different aluminium MMC alloys were investigated, namely Al2014 and Al6061, reinforced with alumina particulates. Each composite and matrix alloy was received in the extruded state having been solution treated and artificially aged to peak hardness (T6) by Hulett Aluminium.

3.4.1 Commercially Pure Aluminium, 1070 and 1200 Aluminium Alloys

Iron and silicon are ever-present impurity elements and the solid solubility of iron in aluminium is very small, phases of aluminium-iron or aluminium-iron-silicon are seen in microstructures of all but refined super-purity aluminium. In the as-cast condition, all of the phases that come into equilibrium with aluminium may be found - $FeAl_3$, Fe_3SiAl_{12} or $Fe_2Si_2Al_9$. Minor impurity or addition elements such as copper and manganese that are not in sufficient quantity to form their own phases, however they influence the type and quantity of less stable phases[84].

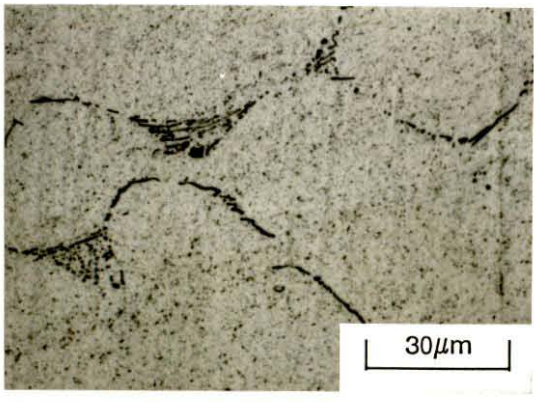

Figure 3.2 Photomicrograph of the 1070 series aluminium alloy (99.7% minimum Al) in the as cast condition. Note the $FeAl_3$ dendrites, with Fe_3SiAl_{12} particulates predominating in the interstices. 0.5% hydrofluoric acid etch.

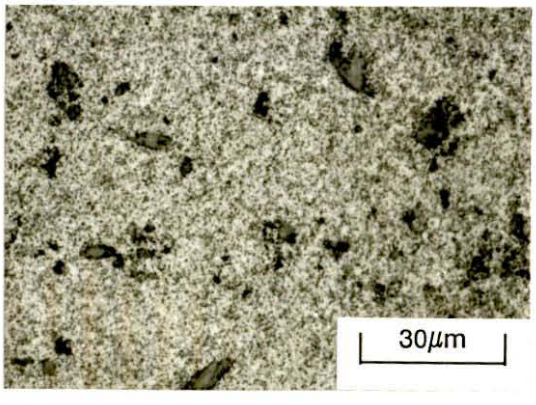

Figure 3.3 Photomicrograph of the 1200 series aluminium alloy (99% minimum Al) in the annealed condition, showing a fine dispersion of fragmented $FeAl_3$ constituent particles and Fe_3SiAl_{12} particulates, due to mechanical working. 0.5% hydrofluoric acid etch.

3.4.2 Aluminium-Manganese Alloy, 3004 Aluminium Alloy

The dominant constituent phases are $(Mn,Fe)Al_6$ and $(Fe,Mn)_3SiAl_{12}$. The magnesium in this alloy tends to shift the phase proportioning towards $(Mn,Fe)Al_6$ because of its affinity for silicon[84].

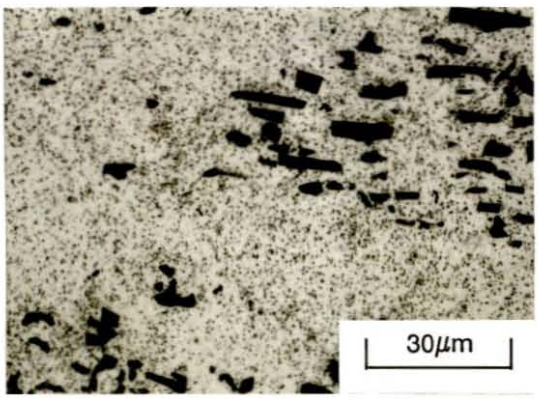

Figure 3.4 Photomicrograph of the 3004 series aluminium alloy (Al-Mn) in the annealed condition. Primary and eutectic particles are found in the microstructure, consisting of intermetallic phases of Mn with Al, Si and Fe; the dark particles are $(Fe,Mn)_3SiAl_{12}$. 0.5% hydrofluoric acid etch.

3.4.3 Aluminium-Magnesium Alloy, 5083 Aluminium Alloy

Magnesium is largely present in solid solution in wrought alloys, but appears as Mg_2Si when solubility limits are reached. In the case of the 5083 aluminium alloy having a magnesium content exceeding 3.5%, Mg_2Al_3 or metastable Mg_2Al_3' may precipitate in grain boundaries or within grains.

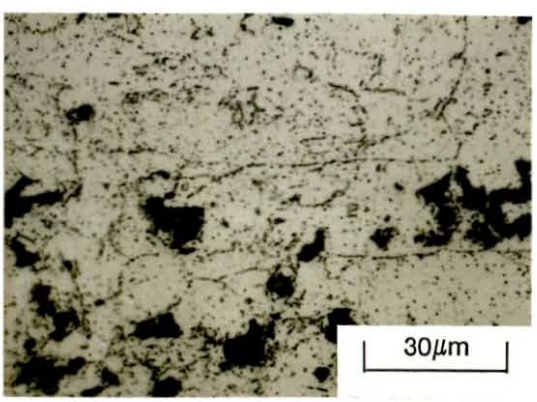

Figure 3.5 Photomicrograph of the 5083 series aluminium alloy (Al-Mg) in the annealed condition. The microstructure consists of eutectic particles of Al with Mg and Si as well as intermetallic phases containing Cr and Mg, such as Mg_2Si. Note the continuous network of Mg_2Al_3 particles precipitated at the grain boundaries. 0.5% hydrofluoric acid etch.

3.4.4 Aluminium-Magnesium-Silicon Alloys, 6061 and 6261 Aluminium Alloys

Magnesium and silicon combine to form magnesium-silicide (Mg_2Si), which in turn forms a simple eutectic system with aluminium. It is the precipitation of the Mg_2Si, after artificial ageing (temper T6), which allows these alloys to reach their full strength. These alloys are charaterised by excellent corrosion resistance and are more workable than other heat-treatable aluminium alloys[171].

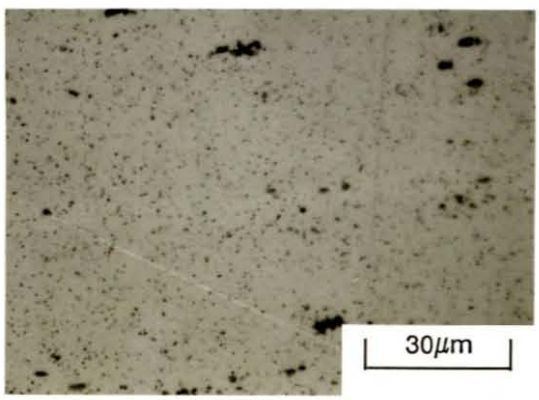

Figure 3.6 Photomicrograph of the 6061 series aluminium alloy in the artificially aged condition. A fine dispersion of $(Fe,Mn,Cr)_3SiAl_{12}$ particulates with larger Mg_2Si particles are evident. 0.5% hydrofluoric acid etch.

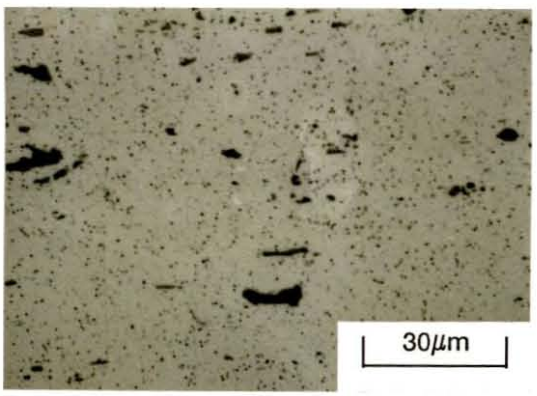

Figure 3.7 Photomicrograph of the 6261 series aluminium alloy, showing a fine dispersion of $(Fe,Mn,Cr)_3SiAl_{12}$ particulates with larger excess soluble Mg_2Si particles. 0.5% hydrofluoric acid etch.

3.4.5 Aluminium-Copper Alloy, 2014 Aluminium Alloy

This is a complex alloy because of the many additives used for strength, corrosion resistance and grain structure control. The high silicon content of the 2014 aluminium alloy stabilises the only-iron rich phase, $(Mn,Fe)_3SiAl_{12}$ [84].

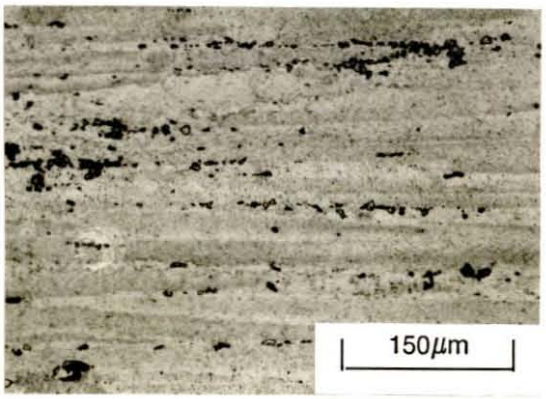

Figure 3.8 Photomicrograph of the 2014 series aluminium alloy. The structure consists mainly of dark, insoluble particles of the complex Fe, Mn, Si and Al phase and a few particles of $CuAl_2$ (light, outlined). 0.5% hydrofluoric acid etch.

3.4.6 Aluminium-Zinc Alloy, 7017 and 7075 Aluminium Alloy

Zinc, by itself, is highly soluble in aluminium and exerts no appreciable influence on the microstructure[84]. Commercial wrought alloys contain zinc, magnesium and copper with smaller additions of manganese and chromium. These alloys develop the highest tensile strengths obtainable for aluminium alloys [171]. The 7017 aluminium alloy is a moderate strength version of the 7075 aluminium alloy.

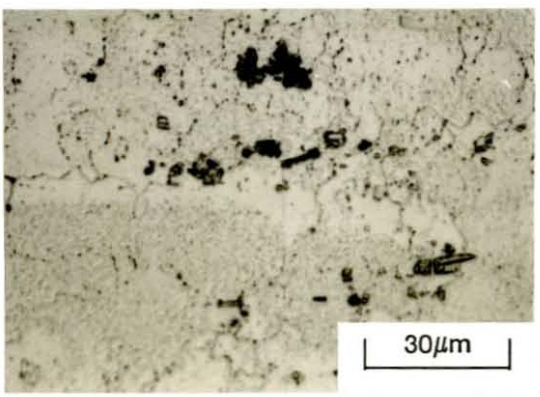

Figure 3.9 Photomicrograph of the 7017 series aluminium alloy, showing $Cr_2Mg_3Al_{18}$ dispersoid banding and larger Mg_2Si particles. 0.5% hydrofluoric acid etch.

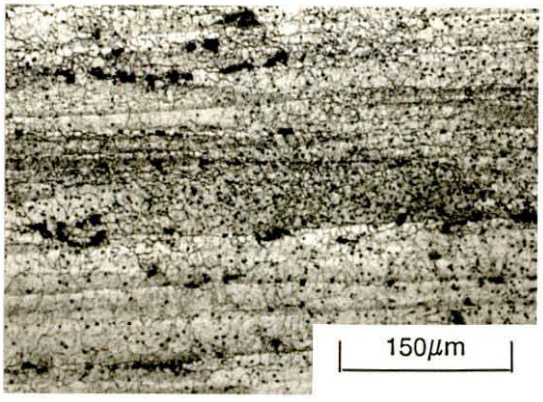

Figure 3.10 Photomicrograph of the 7075 series aluminium alloy, showing $Cr_2Mg_3Al_{18}$ dispersoid banding, with larger Mg_2Si particles. 0.5% hydrofluoric acid etch.

3.5 Microstructures of the Aluminium Metal Matrix Composites

The aluminium metal matrix composites investigated where comprised of two different aluminium alloys, namely 2014 and 6061, reinforced with alumina particulates. The MMC's where tested in the same heat treatment conditions as their corresponding matrix alloys, namely solution treated and artificially aged to peak hardness(T6). Lineal analysis was used to calculate the mean particle sizes as well as the mean particle spacings λ. Lineal analysis was also used to verify the particulate concentrations. The results are tabulated below.

Alloy	*Volume Fraction*	*Particulate Diameter*	*Particulate Spacing*
	volume percent	μm	μm
Al2014 15 vol.% Al_2O_3	21	14	47
Al2014 20 vol.% Al_2O_3	26	21	59
Al2014 15 vol.% Al_2O_3	19	13	58
Al2014 20 vol.% Al_2O_3	25	19	57

Table 3.1 The results of the quantitative metallography performed on the MMC's.

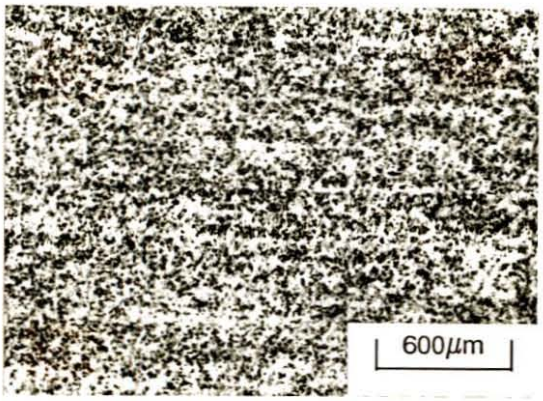

Figure 3.11 Photomicrograph of the 6061 15vol% Al_2O_3 aluminium MMC.

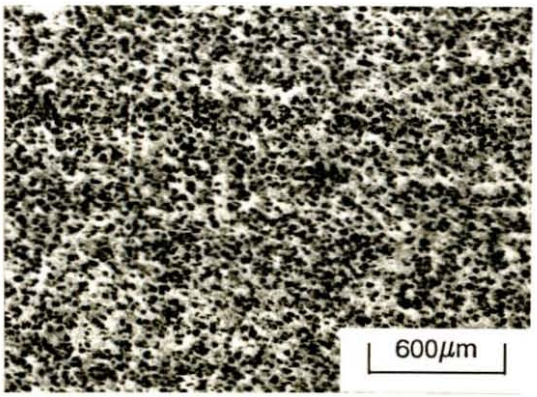

Figure 3.12 Photomicrograph of the 6061 20vol% Al_2O_3 aluminium MMC.

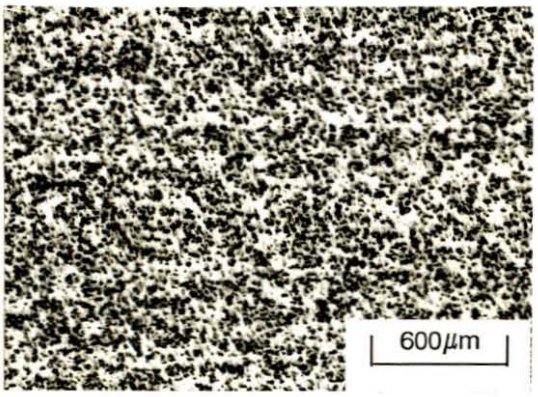

Figure 3.13 Photomicrograph of the 2014 15vol% Al_2O_3 aluminium MMC.

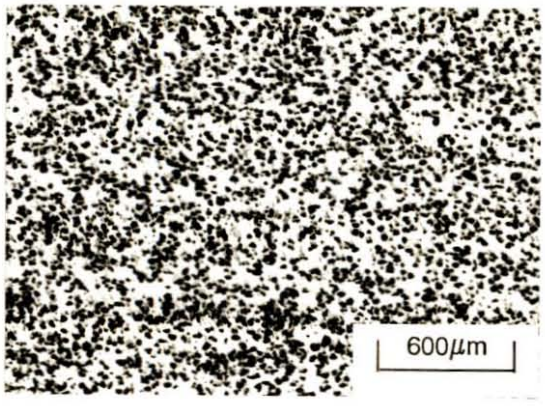

Figure 3.14 Photomicrograph of the 2014 20vol% Al_2O_3 aluminium MMC.

3.6 Microstructures of the Steels

Several steels were tested to investigate the effect of heat treatment and hardness on erosion resistance as well as the effect of corrosion resistance on the erosion-corrosion rates.

3.6.1. 304 Stainless Steel

AISI 304 is an austenitic stainless steel and has a high resistance to corrosion which is usually better than that of the martensitic or ferritic stainless steels. This steel is not hardenable by heat treatment but work hardens rapidly.

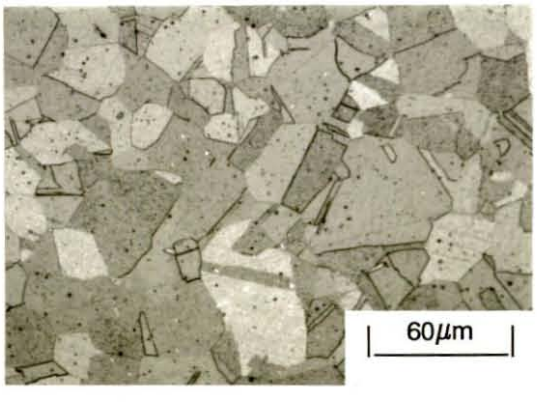

Figure 3.15 Photomicrograph of the AISI 304 stainless steel having an austenitic microstructure. Oxalic acid electrochemical etch.

3.6.2. 431 Stainless Steel

AISI 431 is a heat treatable, martensitic stainless steel with high mechanical properties. The material was tested in the hot rolled and annealed condition.

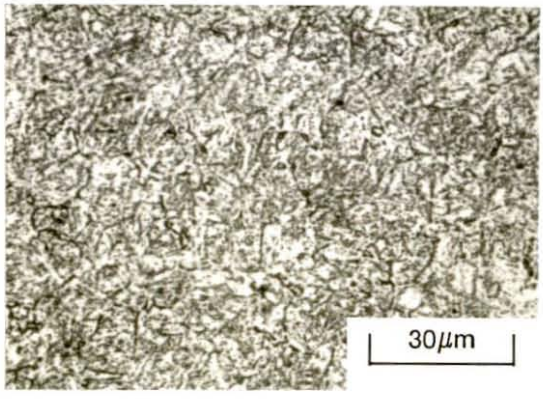

Figure 3.16 Photomicrograph of the AISI 431 stainless steel showing the martensitic microstructure. Oxalic acid electrochemical etch.

3.6.3. 3CR12 Corrosion Resistant Steel

The microstructure of 3CR12 in the hot rolled and tempered condition is fully ferritic. In this condition it has mechanical properties that are comparable to mild steel, but with corrosion resistance far superior to that of conventional mild steels.

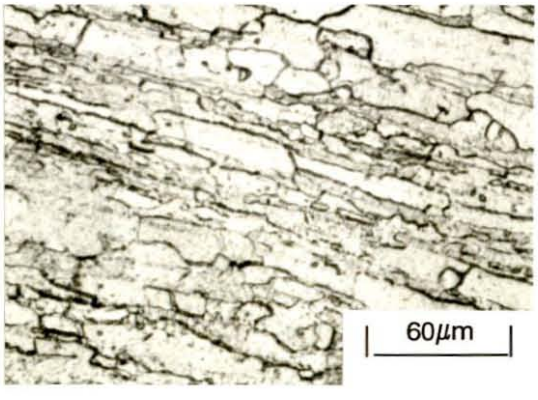

Figure 3.17 Photomicrograph showing the ferritic microstructure of the 3CR12 alloy in the hot rolled and tempered condition. $CuSO_4$ and HCl acid etch.

3.6.4. Mild Steel

Specimens were machined from commercial bright bar and were tested in the as-received normalised condition. The microstructure is consists of equiaxed grains of ferrite with pearlite at the triple point boundaries.

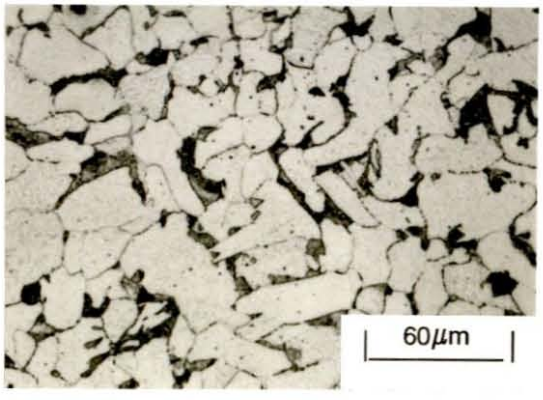

Figure 3.18 Photomicrograph of the mild steel microstructure in the normalised condition. Light grains of ferrite with the dark pearlite grains are visible. 5 per cent Nital etch.

3.6.5. Medium Carbon Steel, EN8

The medium carbon steel was subjected to three different heat treatments in order to achieve different hardness values. The specimens were soaked at 830°C for half an hour followed by an oil quench. Some of the specimens were then tempered at 650°C for half an hour followed by an air cool and some were subjected to a spheroidizing heat treatment at 700°C for 1 hour.

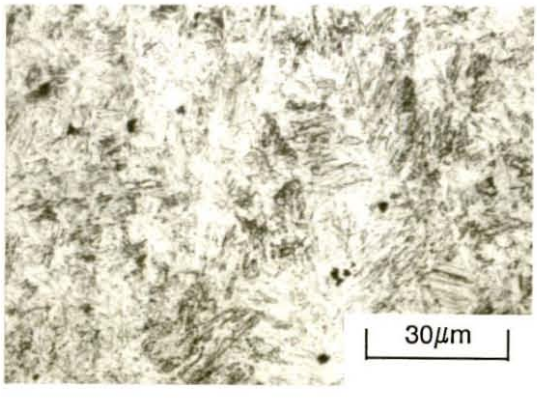

Figure 3.19 Photomicrograph of the EN8 medium carbon steel in the quenched condition having a lath martensitic matrix. 5 per cent Nital etch.

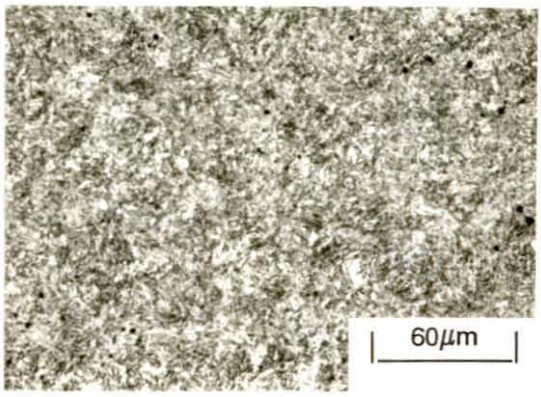

Figure 3.20 Photomicrograph of the EN8 medium carbon steel in the quenched and tempered condition. 5 per cent Nital etch.

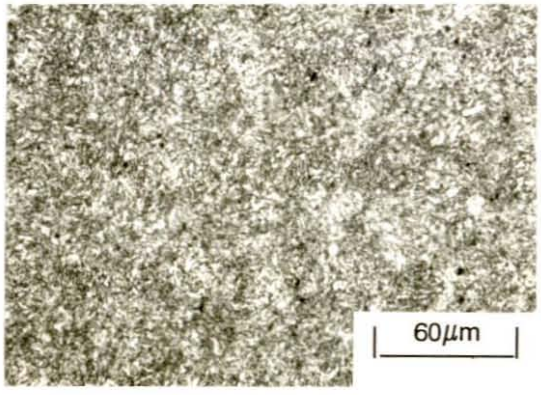

Figure 3.21 Photomicrograph of the EN8 medium carbon steel in the quenched and spheroidised condition. 5 per cent Nital etch.

CHAPTER 4

EXPERIMENTAL WORK

4.1 The Slurry Erosion Rig

A slurry jet erosion apparatus, based on that of Zu[66], was constructed.

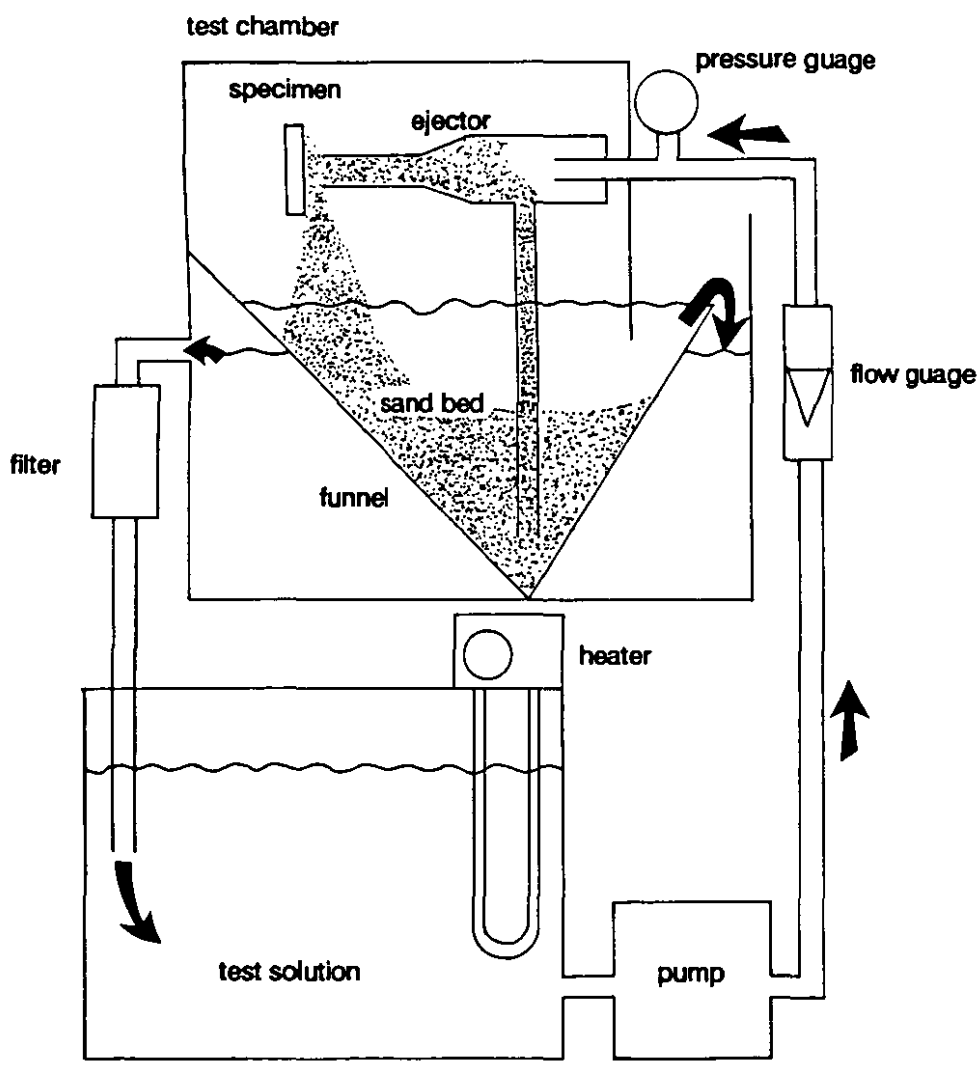

Figure 4.1 The slurry erosion test apparatus.

The rig permits the effect of impact angle, erodent size, erodent concentration, velocity, temperature and carrier fluid parameters to be changed. A schematic diagram of the experimental rig is shown in fig. 4.1. The carrier fluid is circulated from the holding tank and fed to the ejector by the centrifugal pump.

The design of the ejector ensures a pressure drop in the ejector, the resulting vacuum draws a mixture of carrier fluid and erodent particles up through the vertical suction tube, the bottom of which reaches into the submerged bed of erodent. This mixture of erodent and carrier fluid is further mixed with the carrier fluid and the resulting slurry is then accelerated through the exit nozzle and strikes the specimen surface enclosed in a transparent Perspex test chamber.

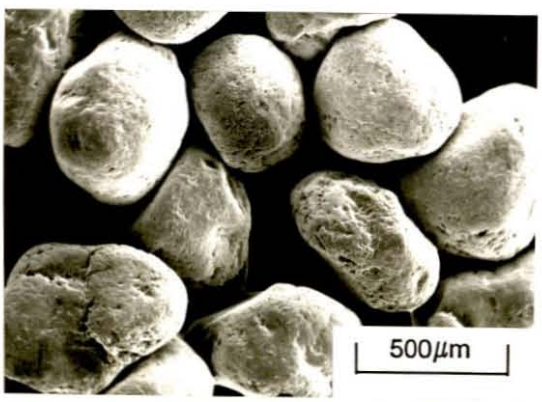

Figure 4.2 Unused silica sand erodent particles.

The different impact angles are obtained by rotating the specimen holder about its horizontal axis. This makes it possible for the slurry which is ejected horizontally from the exit nozzle, on the ejector, to impact the specimen at any preset angle between 0° and 90°. Further the specimen holder was designed to permit *in situ* electrochemical measurements.

After striking the specimen the slurry falls back into the slurry-tank. The erodent particles settle out while the carrier fluid flows through a filter back into the holding-tank. In this manner the slurry is prevented from being circulated through the pump and pipeline, which consequently do not meet with erosive wear damage.

The testing temperature of 55°C was decided upon as this is the equilibrium temperature of the slurry erosion rig under continuous operation. The system is always heated to this temperature by means of thermostatic control before any testing commences.

The following test parameters have been selected,

an impact velocity of 11 m/s,
an erodent concentration of 12% by mass in water,
500 μm silica sand as erodent, (see appendix Table A.4 & A.5)
impact angles of 90° and 60°,
and distilled and synthetic mine water (detailed in the appendix, Table A.6) as carrier fluid.

4.1.1 Electrochemical Measuring

The external circuit used for the electrochemical measurements is shown in fig. 4.3. The specimens are inserted in the sample holder which is then connected in the circuit. A platinum wire serves as the counterelectrode and encircles the specimen. This arrangement allows for an unobstructed passage of electrolyte, but protects the various electrodes from damage by the erodent particles.

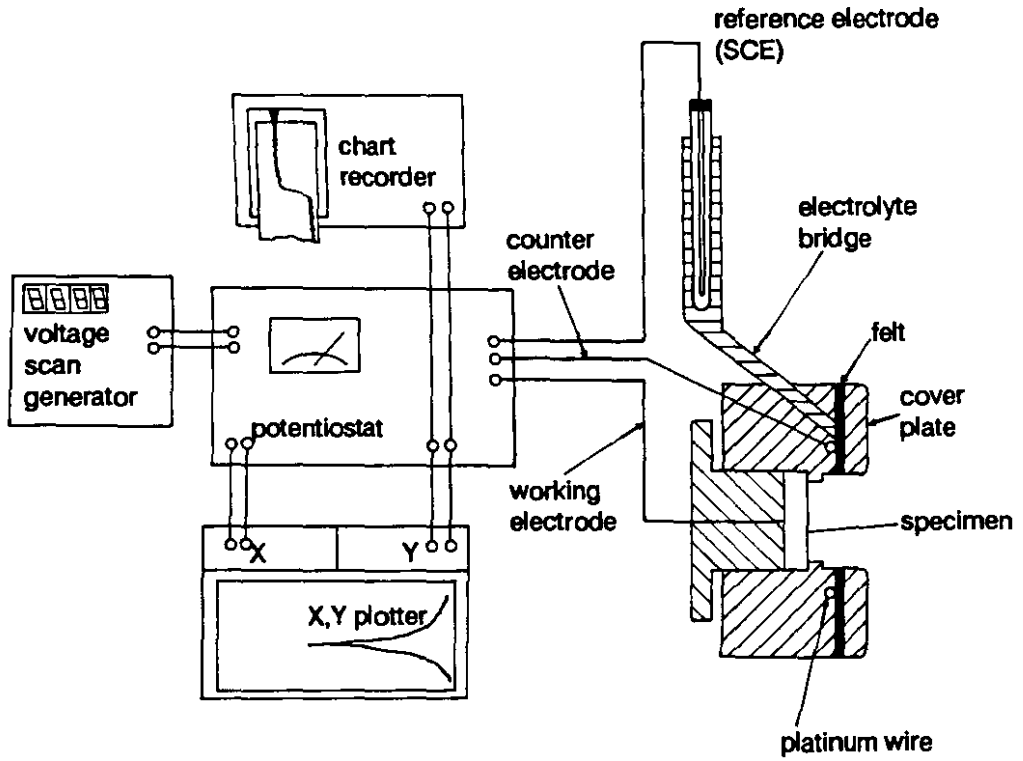

Figure 4.3 The arrangement for the electrochemical measurements.

The reference electrode which is a saturated calomel electrode (SCE) is placed in a holder arranged outside the specimen chamber, and is connected to the system by an electrolyte bridge. The open end of the electrolyte bridge, which is flushed and

filled with carrier fluid from the holding tank, prior to the start of each test, is located flush with the felt cover. The working electrode makes contact with the back of the specimen.

It is important to stress that both polarities of current are present when the specimen is at E_{CORR}. If the specimen is polarised slightly in the positive direction, i.e. made to function more as an anode than it would at E_{CORR}, the anodic current predominates at the expense of the cathodic current. As the specimen potential is driven further positive, the cathodic current component becomes negligible. Experimentally one measures polarisation characteristics by plotting the current response as a function of the applied potential. Since the measured current can vary over several orders of magnitude, the log current is plotted *vs.* potential on a semi-log chart. This plot is termed a potentiodynamic polarisation plot. Note that the use of a semi-log graphs prevents indication of polarity on such plots. Cathodic potentials are negative with respect to E_{CORR} and anodic potentials are positive with respect to E_{CORR}.

4.2 Standard Test Procedures

Each individual test was conducted with fresh erodent, for which 1kg has been found to be sufficient, to ensure that the any degradation of the erodent is insignificant. The erodent is first weighed and then thoroughly washed with the test solution, either distilled or synthetic mine water, prior to being used.

All the test specimens are polished to a 1 μm finish, cleaned ultrasonically in alcohol, weighed, subjected to erosion and or corrosion tests, cleaned again ultrasonically in alcohol and then weighed for mass loss.

The tests in distilled water were done to provide a base comparison with those tests conducted in the synthetic mine water.

Two tests were conducted in all cases with both test results being within 5% of the average.

When a metal is immersed in a corrosive medium, both reduction and oxidation processes occur on its surface. Typically the specimen oxidises (corrodes) and the medium (solvent) is reduced (liberation of hydrogen). The specimen must function as both anode and cathode, and both anodic and cathodic currents occur on the specimen surface. Any corrosion processes that occur are usually as a result of anodic currents.

In studying corrosion processes, it is advantageous to control the electrochemical function of the specimen, i.e. to cause the specimen to act separately as either an anode or cathode but not both simultaneously. By separating the processes in this manner and studying the anodic and cathodic processes separately, a better understanding of how a material will behave electrochemically in an environment can be achieved.

When a specimen is in contact with a corrosive liquid and the specimen is unconnected to any instrumentation, as it would be in service, the specimen assumes a potential termed the corrosion potential, E_{CORR}. A specimen at E_{CORR} has both anodic and cathodic currents present on its surface. However, these currents are exactly equal in magnitude so there is no net current to be measured. The specimen is at equilibrium with the environment. E_{CORR} can be defined as the potential at which the rate of oxidation is exactly equal to the rate of reduction.

Three different electrochemical test procedures are presently being used to evaluate the erosion-corrosion properties of the specimens. In the first test procedure (see Test 1) the corrosion potential of the specimen is monitored for the duration of the slurry erosion test, in order to plot the potential *vs.* time curves of the specimen, under the open circuit potential. The weight loss measurements are also made under the open circuit potential condition. In the second test procedure (see Test 2), which is solely an electrochemical test, a controlled potential scan is applied to the specimen in order to obtain its current density *vs.* potential curve. In the third procedure the test specimen is cathodicly protected, in distilled water, to prevent any corrosion from taking place. This was done to isolate the mechanical component of the mass to be measured.

4.2.1 Test 1

The potential *vs.* time test is conducted because it gives a good indication of when steady state conditions are reached, i.e. when the potential no longer significantly changes with time. This is very valuable since weight loss measurements should be made under steady state conditions.

This test procedure is conducted for 130 min. and the rest potential of the specimen is monitored from the start of the test. For the first 60 minutes the specimen is eroded by the slurry jet, the erodent is then removed from the fluid jet for the next 60 minutes, in the case of the 130 min. test. For the last 10 min. of the 130 min. test the erodent is again added to impacting fluid jet in order to achieve the steady state eroded surface to facilitate examination by optical and electron microscopy.

The mass loss measurements are also made at rest potential with the specimen subjected either to the slurry jet or the carrier fluid jet.

4.2.2 Test 2

This test is known as potentiodynamic polarisation and allows for the characterisation of a specimen by its current *vs.* potential relationship. The specimen potential is scanned slowly in the anodic direction. The curves generated are used to determine corrosion characteristics of metal specimens in the environment of interest, in this case either distilled water or synthetic mine water. Data gathered in the course of a potentiodynamic scan can be used to produce a Tafel plot, which is in turn used to determine the corrosion rate of a material. This test is also performed in order to establish the relative magnitudes of the corrosion current densities (i_{CORR}) and to investigate the degree of passivation encountered in the aluminium alloys the MMCs and the steels.

The polarisation of the aluminium alloys is started at -2000 mV (SCE) and is ended at 1500 mV. For the steels the polarisation is started at -1500 mV (SCE) and is ended at 2000 mV. This results in the starting potential being between 500 and 1200 mV more negative than the rest (corrosion) potential, depending on the alloy concerned. This potential range ensures that both the cathodic and the anodic curves are included for all the specimens.

4.2.3 Test 3

In this procedure the test specimens are cathodically protected, in distilled water, to prevent any corrosion from taking place. Knowing the rest potential, E_{CORR} value, which is determined using either of the above test procedures, a potential can be impressed on the specimen to make it the cathode of the electrochemical cell. This should allow the mechanical component of the mass loss due only to the slurry erosion to be measured.

4.2.4 Reproducibility

The following points have been identified as primary sources of error in the standard tests:

(i) inconsistencies of the erodent particles size and shape, which may vary from batch to batch, and degradation of the erodent during the test

(ii) the water temperature varying ± 2°C

(iii) the amount of corrosive ions dissolved in solution varying, due to weighing and mixing inaccuracies

(iv) increase in dissolved ions due to the evaporation of the test solution and the erosion-corrosion of the test specimens, 60 *l* of carrier fluid is used to keep this factor to a minimum

Due to the design of the test rig, the erodent concentration in the slurry remains constant for the duration of any test as well as for any set of tests. This was verified experimentally and remains true as long as the ejector nozzle is not adjusted, the viscosity of the fluid remains constant and there is sufficient erodent present in the system.

The reproducibilities of the tests were quantified using the aluminium 5083 alloy. Table 4.1 gives the results and the error values for five mass loss slurry tests conducted in synthetic mine water on the Al5083 alloy.

Mass Loss, mg	*Time, min.*
4.62	10
4.59	10
4.74	10
4.56	10
4.29	10
Average = 4.56 mg Standard deviation = 0.17 mg or 3.6%	

Table 4.1 Regression analysis on a set of data, also using the zero mass loss at time zero as a data point.

All mass loss tests and electrochemical tests were conducted twice. The electrochemical tests were also reproducible, as illustrated by the superimposing of two potentiodynamic polarisation scans on the same alloy under the same conditions, in fig. 4.3.

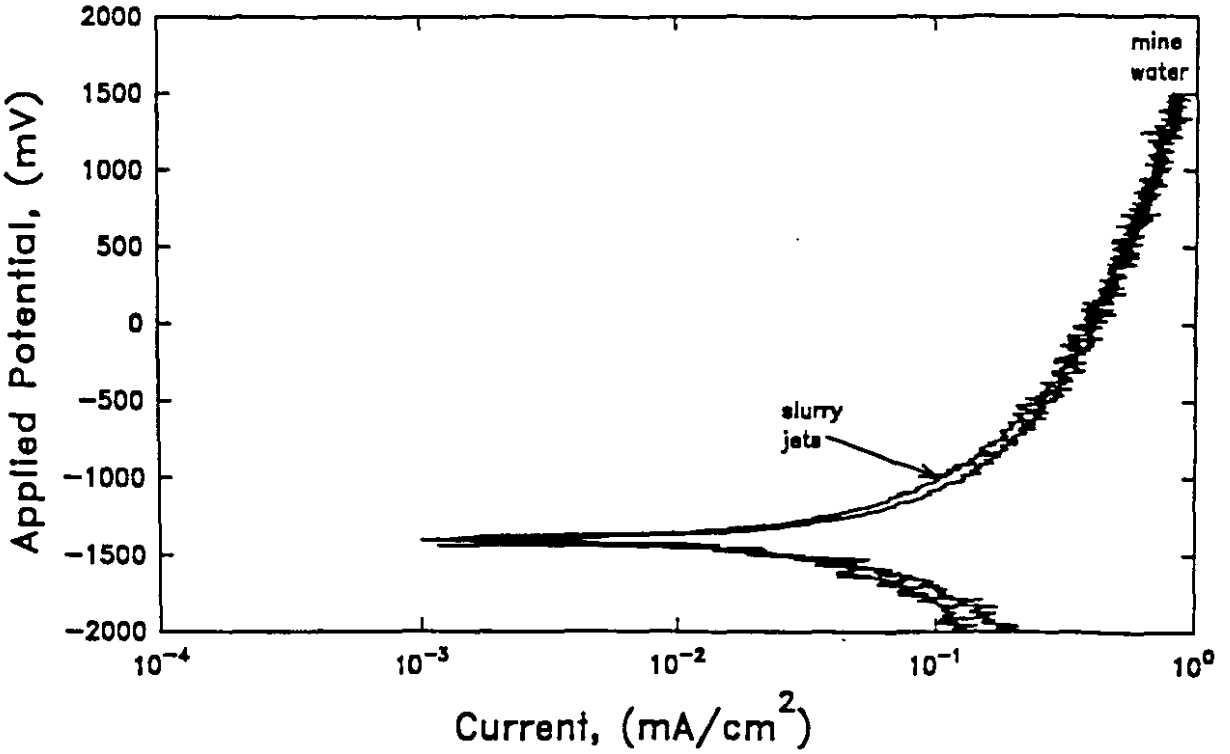

Figure 4.3 Potentiodynamic polarisation scans on the Al 5083 alloy: erodent silica sand (500 μm); carrier fluid, synthetic mine water(pH 5.7); temperature, 55°C; impact velocity, 11 m/s; rate of polarisation 4mV/sec.

CHAPTER 5

RESULTS

The erosive loss of a metal surface is directly proportional to the mass of eroding particles that have impacted the surface, under a given set of test conditions[12]. Under steady state conditions erosion follows a linear relationship and may therefore be quoted as mass loss per unit mass of impacting particles. Figure 5.1 shows the slurry erosion rate of the aluminium 6261 alloy as a function of mass of particles impacted on the target. The mass loss increased linearly with time throughout the period of measurement, with the intercept of the graph at the origin.

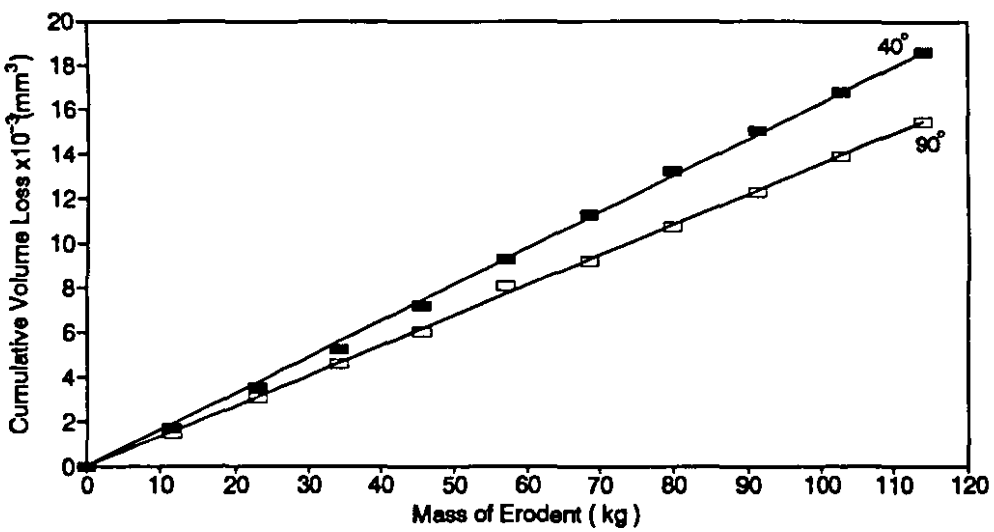

Figure 5.1 Slurry erosion volume losses, of the aluminium 6261 alloy, plotted as a function of mass of erodent impacted on the target; erodent, silica sand (500 μm); carrier fluid, distilled water; temperature, 55°C; impact angles, 90° and 40°; impact velocity, 11 m/s.

Hence the slurry erosion rates will be quoted as a volume loss per unit mass of erodent, which in engineering applications is a more important measure of material loss[12]. Note that the erosion rate is greater when tested at the lower impact angle of 40°.

5.1 Aluminium Alloys

The performance of the different aluminium matrix alloy materials were evaluated in distilled and synthetic mine water, in an attempt to evaluate the erosion and corrosion components. The results of all the tests performed are tabulated in the Appendix, Table A.15 and A.16 and are presented graphically below.

The slurry erosion rates, as tested at 90° in distilled water, when plotted as a function of hardness exhibits a general trend of decreasing slurry erosion rates with increasing in hardness, see fig. 5.2. This is particularly evident when the aluminium alloys are separated into non heat-treatable and heat-treatable alloys.

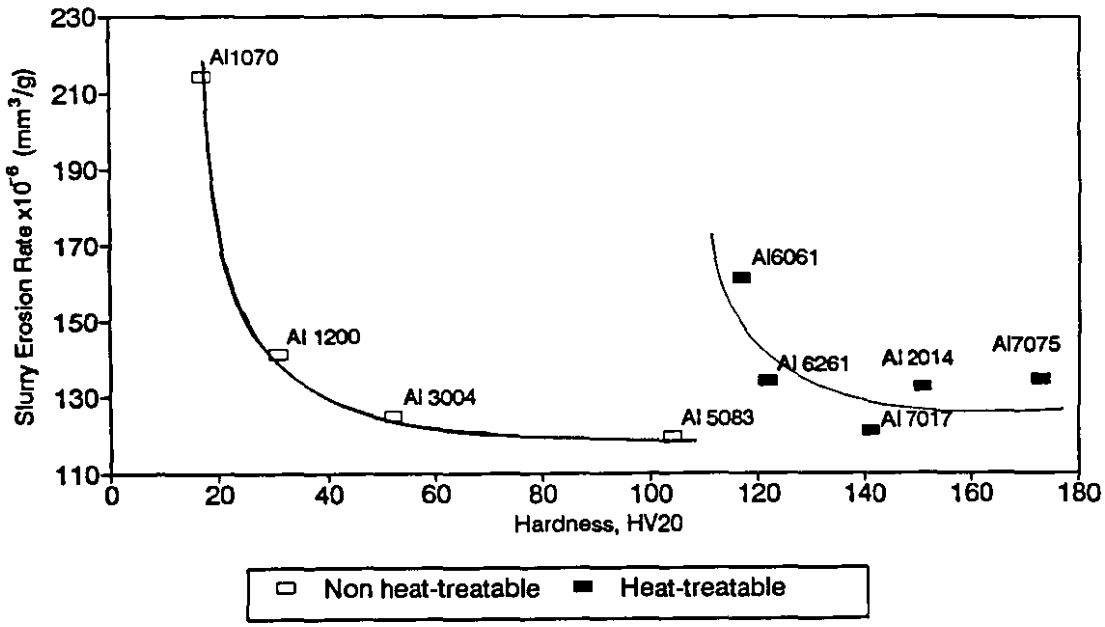

Figure 5.2 Slurry erosion rates of the aluminium alloys tested plotted as a function of initial surface hardness; erodent, silica sand (500 μm); carrier fluid, distilled water; temperature, 55°C; impact angle, 90°; impact velocity, 11 m/s.

Figures 5.3 through to 5.5 are macrophotographs of the specimens after 10min. of slurry erosion in distilled water. The erosion profiles of both 40° and the 90° impact angles are shown.

After undergoing slurry erosion at an impact angle of 40°, figs. 5.3(a) and 5.4(a), the ductile low strength 1070, 1200, 3004 series aluminium alloys exhibit a pronounced ripple structure that consists of a series of hills and valleys oriented to the incident particle direction. The higher strength 5083, 6061, 6261, 7017 and 7075 unreinforced aluminium alloys all had similar erosion profiles and did not display a ripple structure, fig. 5.5(a). The ripple structure was not observed for the 90° impact angle.

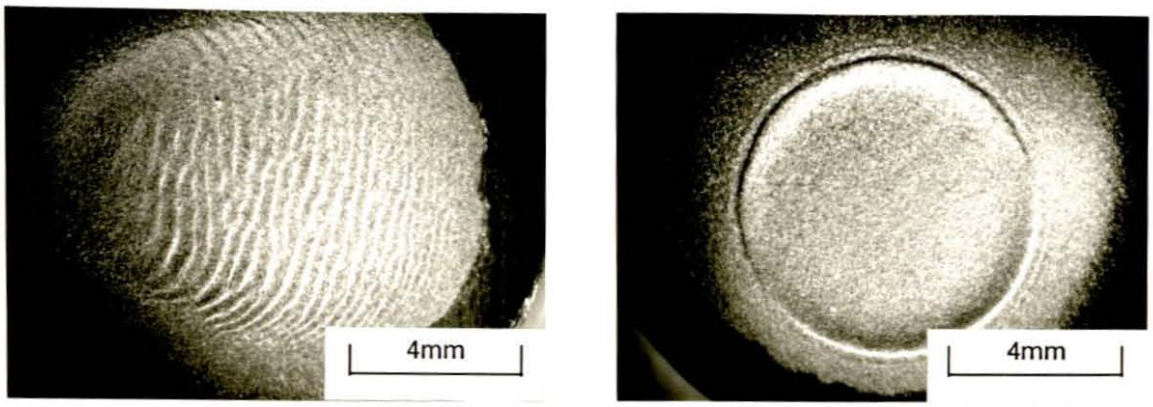

(a) (b)

Figure 5.3 The 1200 series alloy (31HV), (a) eroded from left to right at 40° displaying ripple formation and (b) eroded at 90°.

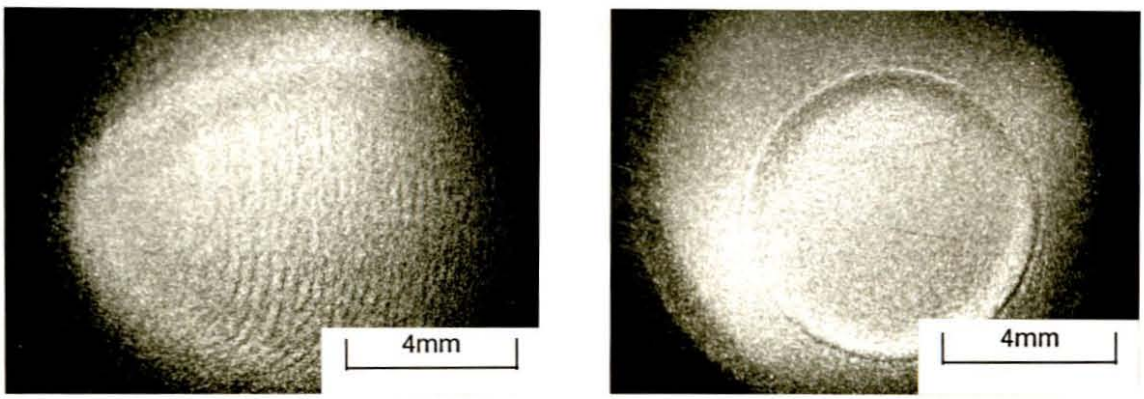

(a) (b)

Figure 5.4 The 3004 series alloy (52HV), (a) eroded from left to right at 40° displaying ripple formation and (b) eroded at 90°, with material displaced to the edge of the eroded area.

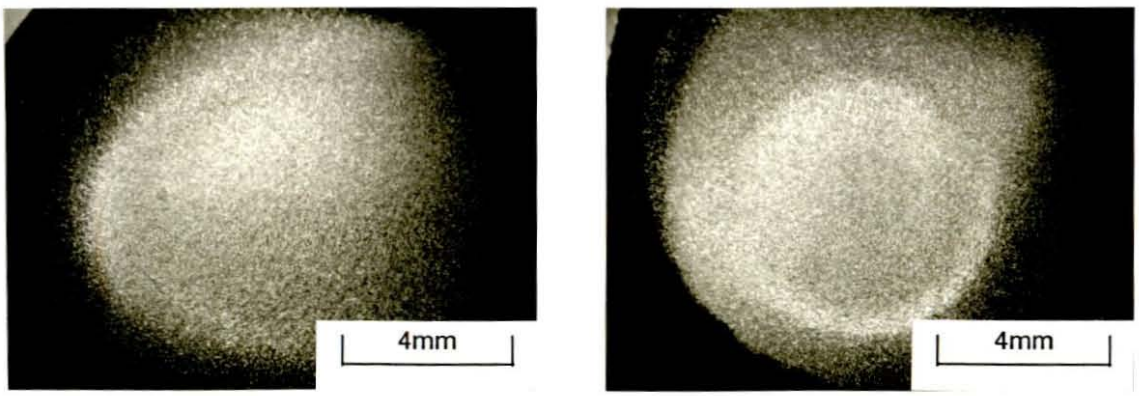

(a) (b)

Figure 5.5 The 5083 series alloy (105HV), (a) eroded from left to right at 40° and (b) eroded at 90°.

When an erodent particle impacts the surface the result is a local depression of the surface referred to as an impact crater. The impact craters are always smaller than

the erodent particles, implying that only a portion of a particle enters and exits the impact crater. For the aluminium alloys tested the average impact crater was typically 50μm in diameter, i.e. a tenth of the erodent diameter. For all the alloys tested the single impact crater diameters were roughly the same, however the amount of material extruded to the edges of the single impact craters decreased with increasing hardness.

When an erodent particle impacts the surface obliquely a crater is formed by a smearing (as opposed to ploughing) action and there is typically a ridge of material which has been pushed to the exit side. The ridge or lip may be strongly or weakly attached to the surrounding metal.

Ploughing craters occur when a projecting corner or a sharp point on a particle forces its way deeply into the surface and then translates along the surface for a distance. This results in projecting lips forming along either side of the crater formed. The traverse of the particle also forms a hump on the exit side of the crater.

Fig. 5.6(a) through to fig. 5.10(a) are SEM micrographs of single impact sites and steady state erosion surfaces of the aluminium alloys.

The single impact sites in figs. 5.6(a) to 5.10(a) were produced by eroding the specimens with 5 g of the silica sand erodent, while the steady state erosion surfaces in figs. 5.6(b) to 5.10(b) were produced after 10min. of erosion. The single impact sites on the softer alloys, such as the aluminium 1200 alloy in figs. 5.6(a) and 5.9(a), are visibly deeper, exhibiting a more ductile mode, than those on the harder alloys, figs. 5.7(a) and 5.10(a). A more brittle chipping mode of material removal appears to be responsible for the slurry erosion at the 90° for all the aluminium alloys, figs 5.9(a) and 5.10(a).

The surface morphology of all the samples eroded at 40°, figs 5.6(b) and 5.7(b), is such that individual impact events can be distinguished on the steady state surfaces, with small lips or platelets of material still attached or partially attached, to the impact craters. The platelet attached to front of the impact crater, on the surface of the relatively soft aluminium 1200 alloy, fig. 5.6(b), is significantly larger than the platelets that formed on the much harder aluminium 7017 alloy surface shown in fig. 5.7(b).

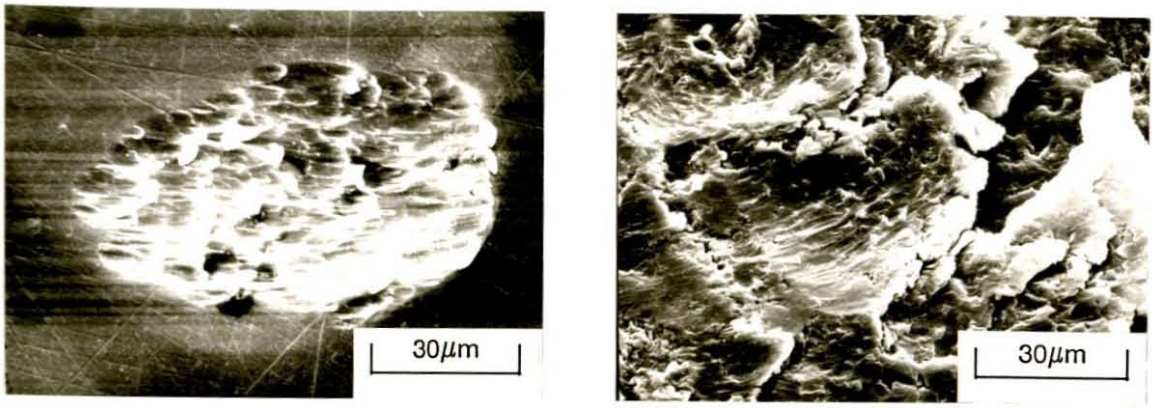

(a) (b)

Figure 5.6 SEM micrographs of the 1200 series alloy (31HV) eroded at 40° from left to right.(a) Single impact site and (b) steady state erosion surface.

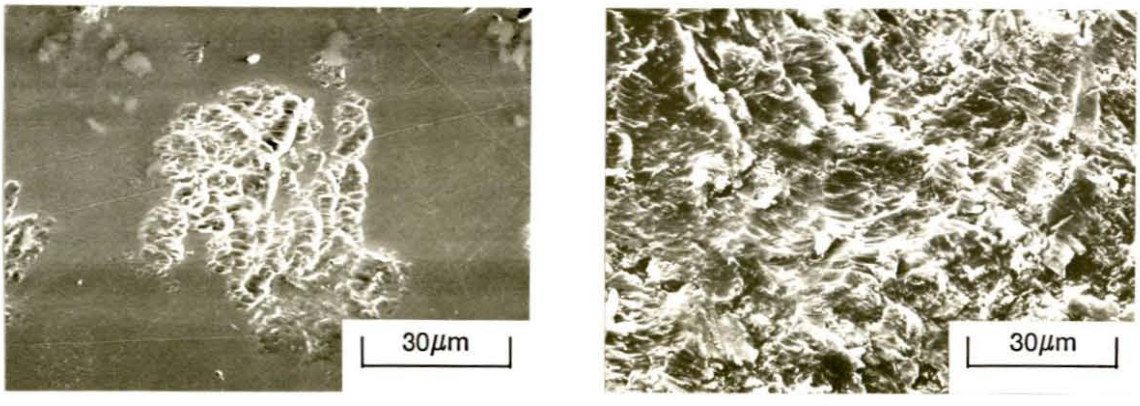

(a) (b)

Figure 5.7 SEM micrographs of the 7017 series alloy (136HV) eroded at 40° from left to right.(a) Single impact site and (b) steady state erosion surface.

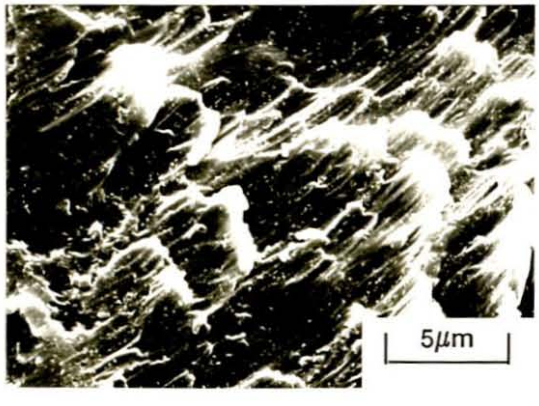

Figure 5.8 Highly magnified area within a single impact site on the surface of the 7017 series alloy (136HV) eroded at 40°.

The erodent particles impacting the target normal to the surface results in less ploughing and cutting than do those impacting the surface at 40°.

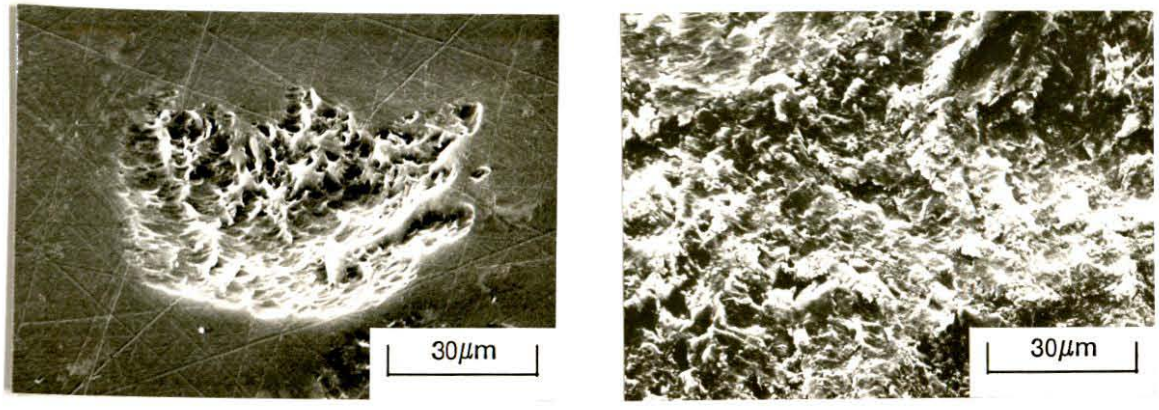

(a) (b)

Figure 5.9 SEM micrographs of the 1200 series alloy (31HV) eroded at 90°.(a) Single impact site and (b) steady state erosion surface.

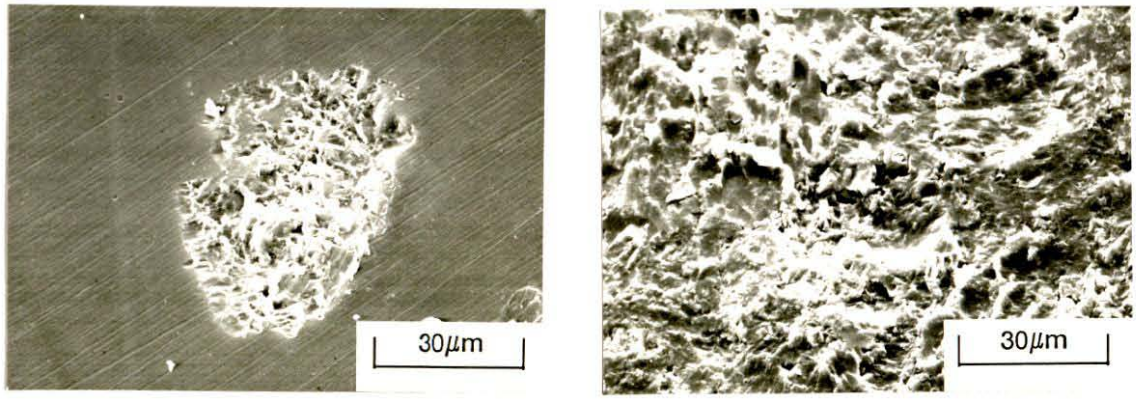

(a) (b)

Figure 5.10 SEM micrographs of the 7017 series alloy (136HV) eroded at 90°.(a) Single impact site and (b) steady state erosion surface.

The steady state erosion surfaces are characterised by a peak-and-valley morphology with attached platelets of material. Note the similar appearances of the steady state surfaces of the alloys tested at the two different angles, this suggests that the impact events at the two angles are similar. For both angles the impacts result in indentation, ploughing and cutting events. The indentation events do not remove material as can be seen from the single impact sites. Hutchings[14] has shown that ploughing events occasionally remove material by a micromachining or cutting action. The impact events most favourable for material removal are the impacts on attached platelets. For all the alloys the impact events are accompanied by extensive material displacement that occurs at the impact site, accompanied by high strains.

Table 5.1 gives a ranking of slurry erosion in distilled water, and erosion-corrosion resistance in synthetic mine water, together with the hardness and estimated corrosion current, i_{CORR}, values of the matrix alloys. The corrosion currents were graphically estimated from the Tafel slopes drawn on the current density vs. potential

graphs in the manner illustrated in fig. 5.11 below. The current density vs. potential graphs of the aluminium alloys can be seen given in fig. 5.13 and figs. A.17 to A.23.

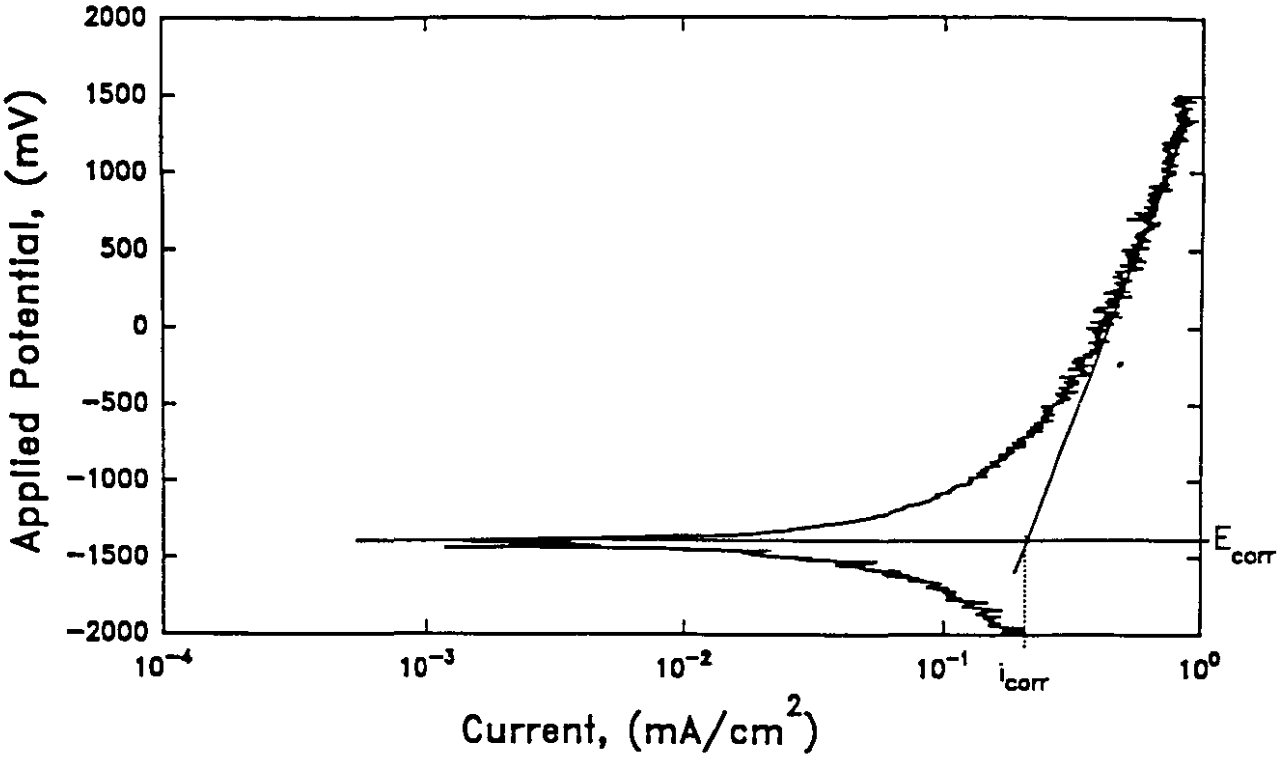

Figure 5.11 Graphs of the current density *vs.* potential scan done on the Al1200 alloy illustrating the method used to determine i_{CORR}: erodent, silica sand (500 μm); carrier fluid, synthetic mine water(pH 5.7); temperature, 55°C; impact angle, 90°; impact velocity, 11 m/s; rate of polarisation 4mV/sec.

Distilled Water				*Synthetic Mine Water*				
Alloy	*Hardness*	*Erosion Rate* $\times 10^{-6}$	i_{CORR}	*Alloy*	*Erosion Rate* $\times 10^{-6}$	i_{CORR}	*Erosion Rate Increase*	
	HV20	mm^3/g	nA/cm^2		mm^3/g	$\mu A/cm^2$	mm^3/g	%
Al1070	17	213	200	Al1070	295	500	82	38
Al6061	117	161	60	Al1200	200	200	59	42
Al1200	31	141	70	Al2014	173	200	40	30
Al6261	122	134	50	Al7075	173	700	41	31
Al2014	151	133	30	Al6061	164	500	3	2
Al7075	173	132	40	Al3004	161	300	36	29
Al3004	52	125	80	Al7017	159	200	38	31
Al7017	141	121	80	Al6261	148	200	14	10
Al5083	104	119	90	Al5083	139	200	20	17

Table 5.1 Slurry erosion rates of the aluminium alloys and their corrosion current(i_{CORR}) values in distilled water and synthetic mine water. The increments in slurry erosion rates in the mine water as compared with distilled water are also tabulated.

The results in Table 5.1, which are plotted in fig 5.12, illustrate the effect of the synthetic mine water on the slurry erosion rates. The materials tested experience significant increases in their slurry erosion rates due to the presence of the corrosive ions in the corrosive mine water. The erosion resistance rankings of the materials when subjected to the synthetic mine water are closely linked to the increase in erosion rate experienced due to the addition of the corrosive ions, with the exception of the aluminium 6061 alloy. Note also that the leaner alloys, those with less alloying additions, exhibit the greatest increases in their slurry erosion rates due to the presence of the corrosive ions in the corrosive mine water.

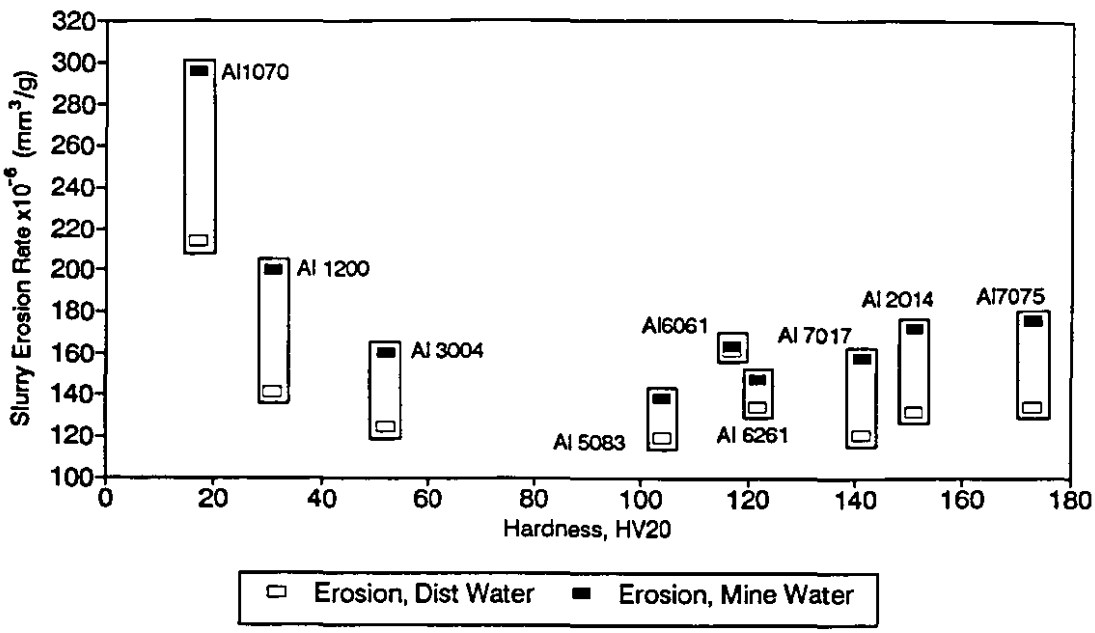

Figure 5.12 Slurry erosion rates of the aluminium alloys tested as function of initial surface hardness; erodent, silica sand (500 μm); carrier fluid, distilled water and synthetic mine water(pH 5.7); temperature, 55°C; impact angle, 90°; impact velocity, 11 m/s.

For all the materials tested their current densities increase by at least three orders of magnitude when tested in the synthetic mine water, in comparison to current densities observed in distilled water. This can be seen by the graphs, fig. 5.13, shifting towards the right, i.e. to higher current densities, when tested in synthetic mine water. The potentiodynamic scans for the other aluminium alloys also illustrate this, see figs. A.17 to A.23 in the Appendix.

The values of the corrosion current densities are also greater when measured during slurry erosion than when measured only in the fluid jet (i.e. with no entrained erodent). This can be seen from the potentiodynamic curves in fig. 5.13 (and figs. A.17 to A.23) which shift slightly to the right when subjected to slurry erosion by the

silica sand. Note also that the curves shift to more negative potentials, i.e. in the anodic direction, when subjected to the slurry jet.

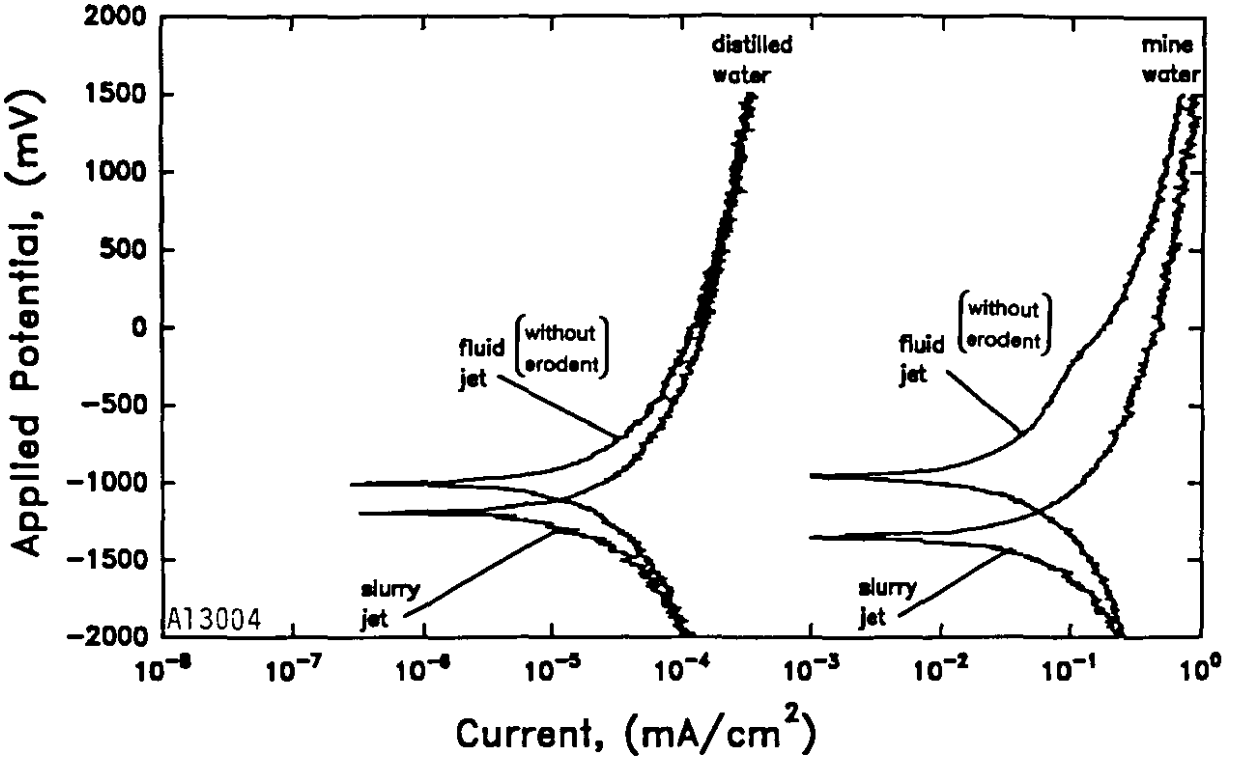

Figure 5.13 Al3004 - graphs of the current density *vs.* potential scans: erodent, silica sand (500 μm); carrier fluid, distilled water and synthetic mine water(pH 5.7); temperature, 55°C; impact angle, 90°; impact velocity, 11 m/s; rate of polarisation 4mV/sec. Similar effects are observed for all the alloys (see figs. A.17 to A.23 in the Appendix).

The current density *vs.* potential curves of the aluminium alloys presented above all exhibit the same general trends. To investigate the effect of impact angle on the corrosion rates, the 5083 aluminium alloy was used to generate current density *vs.* potential scans in the synthetic mine water subjected to erosion at 90° and 60°, (fig. 5.14). No significant differences can however be observed.

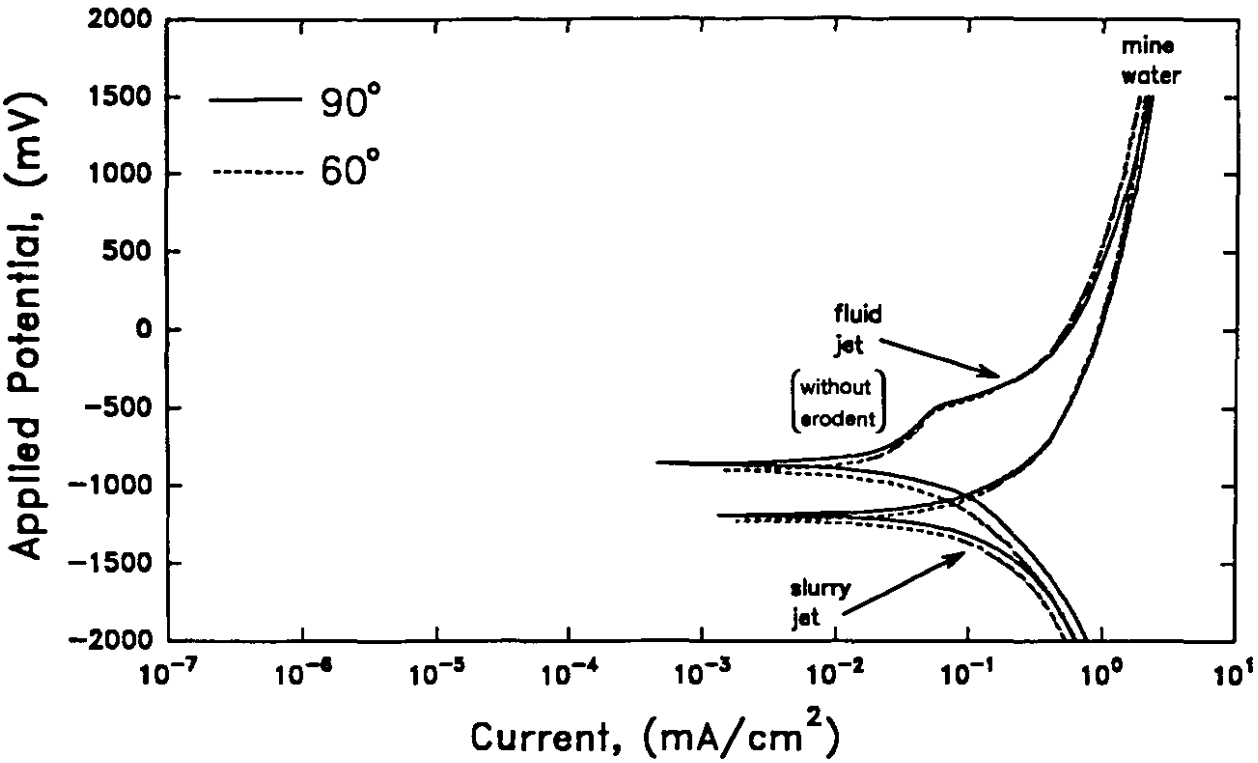

Figure 5.14 Graphs of the current density *vs.* potential scans of a selection of the 5083 aluminium alloy tested at an impact angle of 90° and 60°: erodent, silica sand (500 μm); carrier fluid, synthetic mine water(pH 5.7); temperature, 55°C; impact velocity, 11 m/s; rate of polarisation 4mV/sec.

The corrosion potential *vs.* time curves of the various aluminium alloys, presented in figs. 5.15 and 5.16 show that during the initial 20 minutes of the test there is a gradual drop in the corrosion potential, with the rest potential becoming gradually more negative until a steady state is reached. There is a distinct change in the rest potential at 60 min., when only the carrier fluid is left to impinge on the surface. When the erodent is once again added to the impacting jet, at 120 min. the rest potential immediately drops to more negative potentials.

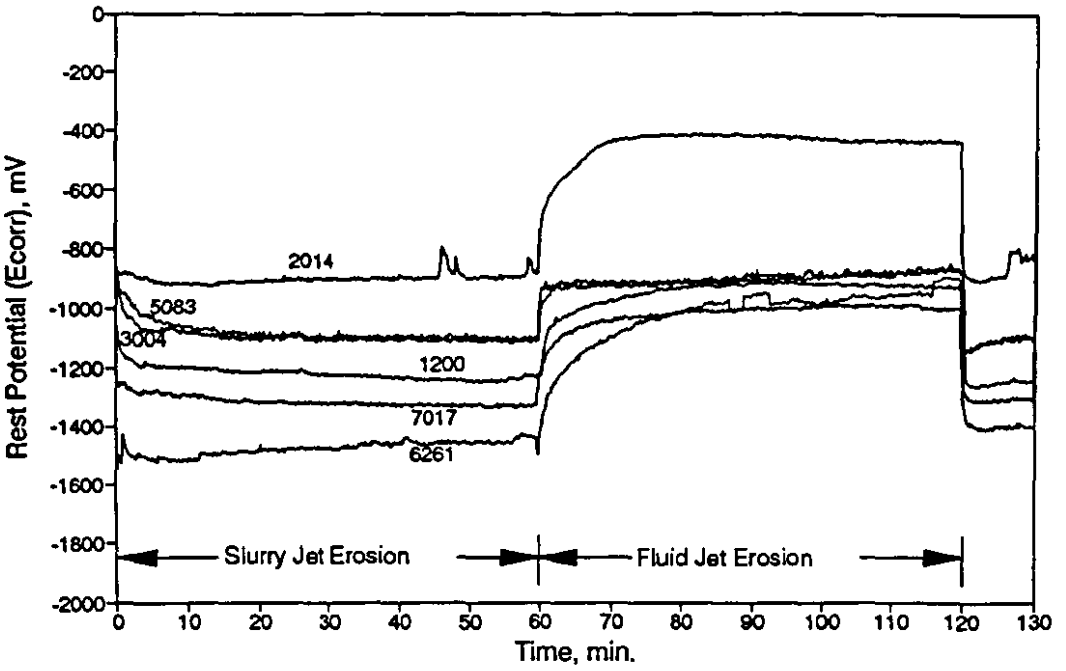

Figure 5.15 The potential *vs.* time curves of a selection of the aluminium alloys, tested in distilled water at 55°C with 500 μm silica sand as erodent using a 90° impact angle.

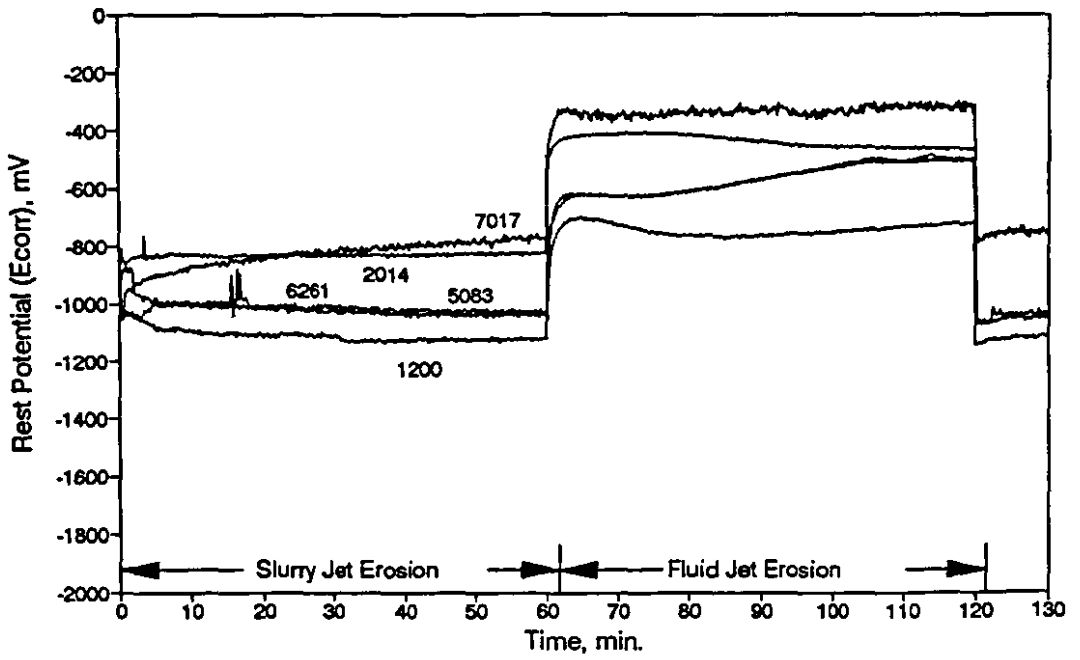

Figure 5.16 The potential *vs.* time curves of a selection of the aluminium alloys, tested in synthetic mine water at 55°C with 500 μm silica sand as erodent using a 90° impact angle.

5.2 Aluminium Metal Matrix Composites

The results of the slurry erosion tests, performed in distilled water, on the MMCs and their constituent alloys are presented in Table 5.2. In general the composites erode more rapidly than do the base alloys, despite their greater hardness values.

Alloy	*Volume Fraction*	*Particulate Diameter*	*Hardness*	*Erosion Rate 90° angle*	*Erosion Rate 60° angle*	*Work to fracture*
		μm	HV20	mm^3/g	mm^3/g	MJ/m^3
Al2014	0	-	151	133	162	49.9
"	15%Al_2O_3	14	174	142	181	5.42
"	20%Al_2O_3	21	197	158	185	2.23
Al6061	0	-	124	161	199	33.92
"	15%Al_2O_3	13	130	155	182	24.15
"	20%Al_2O_3	19	141	164	199	8.25

Table 5.2 The results of the slurry erosion tests performed in distilled water, on the MMCs and their constituent alloys at impact angles of 90° and 60°. The work to fracture results obtained by Wilson *et al.* [107] are also tabulated.

The results of the slurry-erosion tests performed on the MMC's at the 90° and 60° impact angles are presented graphically in figs 5.17 and 5.18, as a function of work to fracture. As in the case with the matrix alloys the aluminium metal matrix composites experience a significant increase in their slurry erosion rates because of the corrosion component. The erosive-corrosive wear rates, when tested in the synthetic mine water, are greater than the wear rates for the tests conducted in distilled water, this is illustrated graphically in figs 5.17 and 5.18.

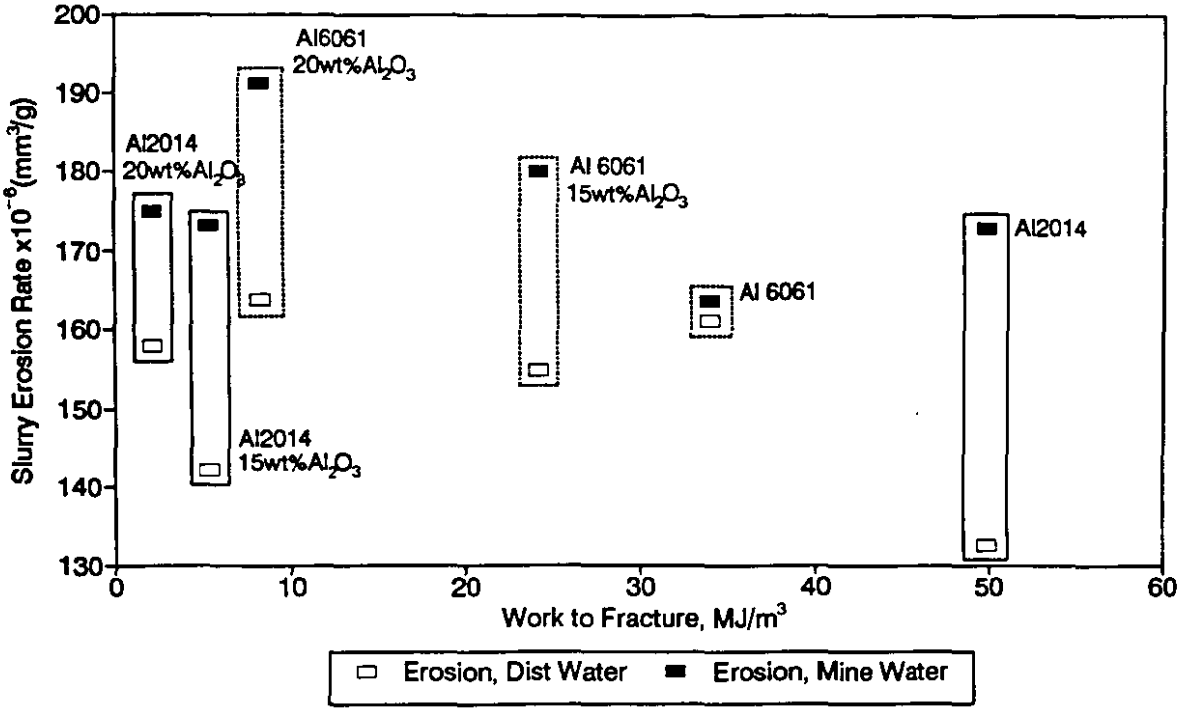

Figure 5.17 The slurry erosion rates of the aluminium MMCs and their constituent alloys tested at 90°. The work to fracture results are those obtained by Wilson *et al.*[107]. Slurry erodent, silica sand (500 μm); carrier fluid, distilled and synthetic mine water(pH 5.7); temperature, 55°C; impact velocity, 11 m/s.

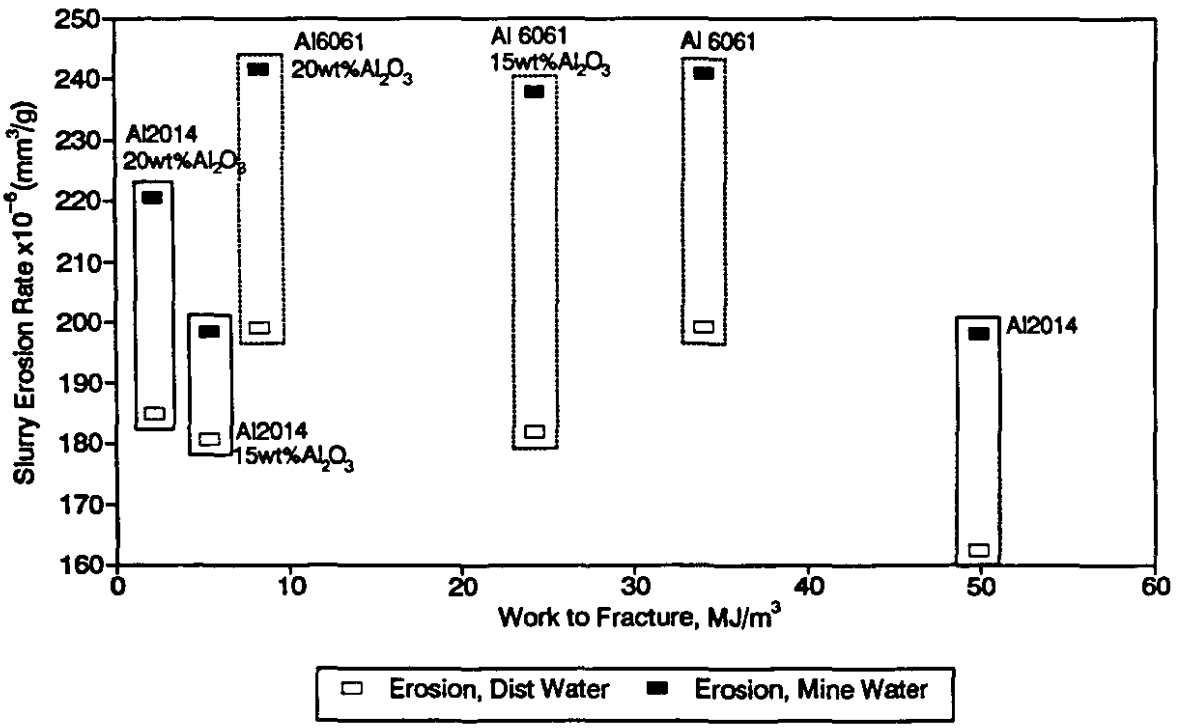

Figure 5.18 The slurry erosion rates of the aluminium MMCs and their constituent alloys tested at 60°. The work to fracture results are those obtained by Wilson *et al.*[107]. Slurry erodent, silica sand (500 μm); carrier fluid, distilled and synthetic mine water(pH 5.7); temperature, 55°C; impact velocity, 11 m/s.

Fracture of the reinforcing particles was observed at single impact sites on all the MMCs tested, see fig 5.19.

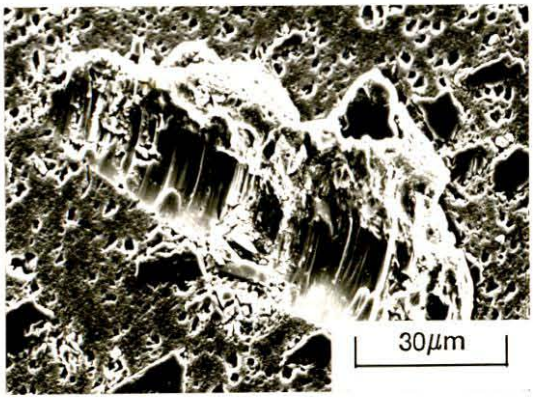

Figure 5.19 A single impact site on the surface of the Al6061 15wt% Al_2O_3 MMC. Note the fractured alumina reinforcing particle in the centre of the impact site. The MMC was eroded at 90° in the synthetic mine water.

Potentiodynamic tests were also performed on the MMCs to investigate the effect of the reinforcing particles on the corrosion rates of the alloys. The results are presented in figs. 5.20 (and A.25 in the Appendix).

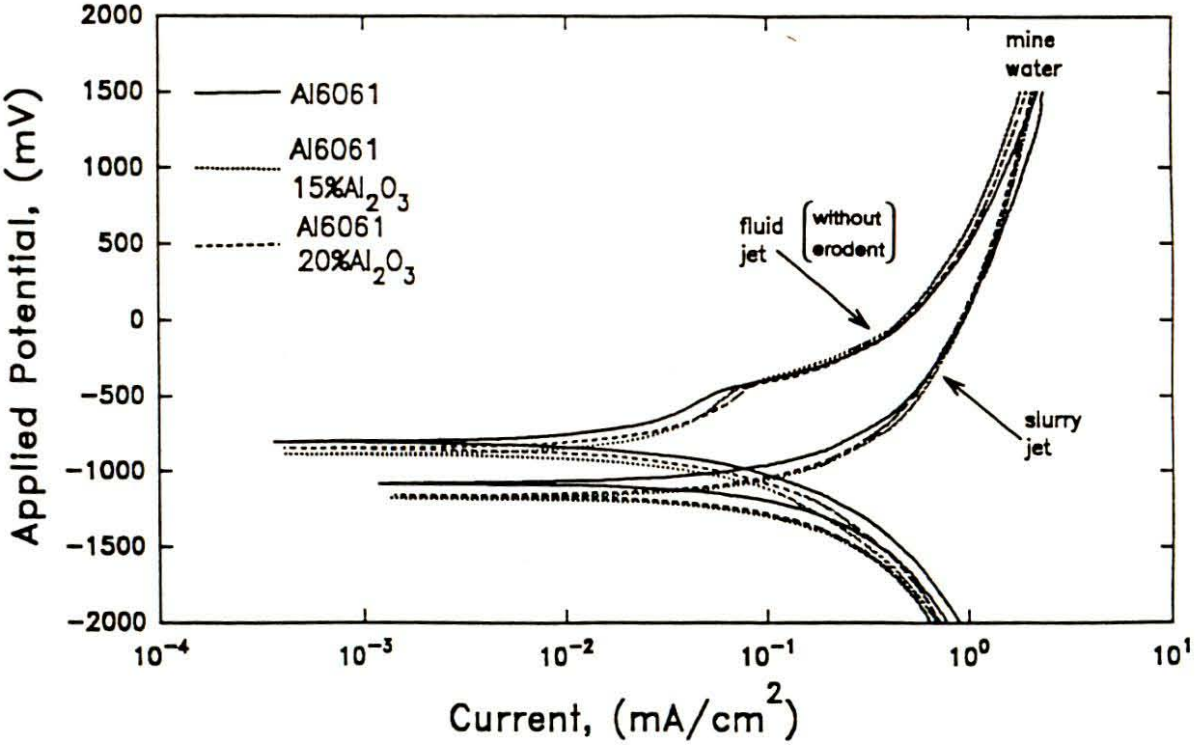

Figure 5.20 Graphs of the current density *vs.* potential scans of the 6061 aluminium matrix alloy and the Al6061 MMCs. Tested at an impact angle of 90°: erodent, silica sand (500 μm); carrier fluid, synthetic mine water(pH 5.7); temperature, 55°C; impact velocity, 11 m/s; rate of polarisation 4mV/sec.

5.3 Steels

The results of the slurry erosion tests performed on the steel specimens, in distilled water and synthetic mine water, are presented graphically below, fig. 5.21. The slurry erosion rates have been plotted as a function of hardness. The increasing hardness values of the EN8 specimens, due to their different heat treatments, result in very noticeable improvements in their erosion resistances. Note that the additional slurry erosion losses, due to the corrosion, is essentially constant for these different heat treatment conditions. Note the low erosion rate of the 304SS, tested in distilled water, considering its relatively low hardness in comparison to the other steels. As was the case for the aluminium alloys, all the steels tested experience higher material wastage rates when tested in the synthetic mine, as opposed to distilled water. The corrosivity of the carrier fluid has the largest effect on the three corrosion resistant steels.

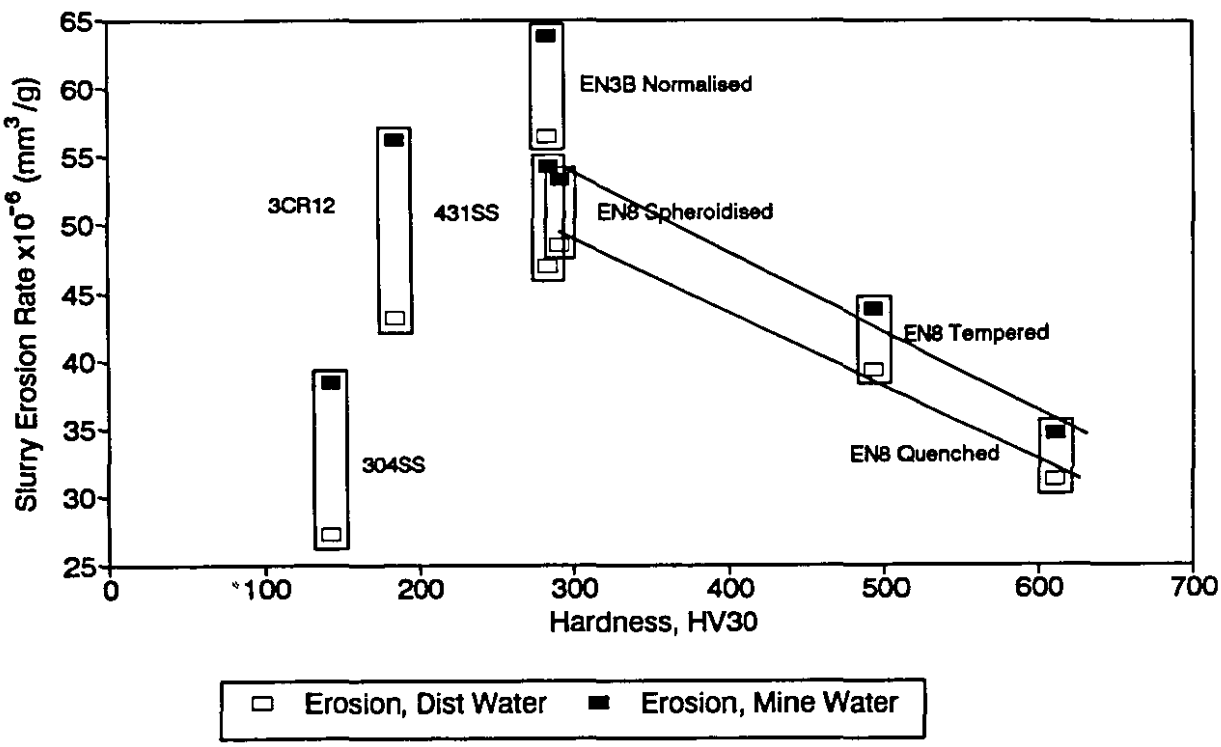

Figure 5.21 Slurry erosion rates of the steels plotted as a function of hardness; erodent, silica sand (500 μm); carrier fluid, distilled water and synthetic mine water(pH 5.7); temperature, 55°C; impact angle, 90°; impact velocity, 11 m/s.

Corrosion tests were conducted on the steel specimens by subjecting them to the synthetic mine water jet (with no entrained erodent particles). Each corrosion test was conducted for an hour, as was the case for the slurry erosion tests. The corrosion tests on the 304 and 431 stainless steels and the 3CR12 did not result in any measurable mass losses, (fig. 5.22). The corrosion losses experienced by the EN8 steel specimens, in all three heat treatment conditions, are similar, with the EN3B (mild steel) specimens exhibiting the highest corrosion rate. Evidence of corrosion

having taken place is apparent from the corrosion products that formed on the surface of the EN3B and EN8 specimens, under all heat treatment conditions. For the erosion-corrosion tests however the corrosion products were continuously being removed and were thus not in evidence, except for slight discolouration around the edges of the Teflon washer.

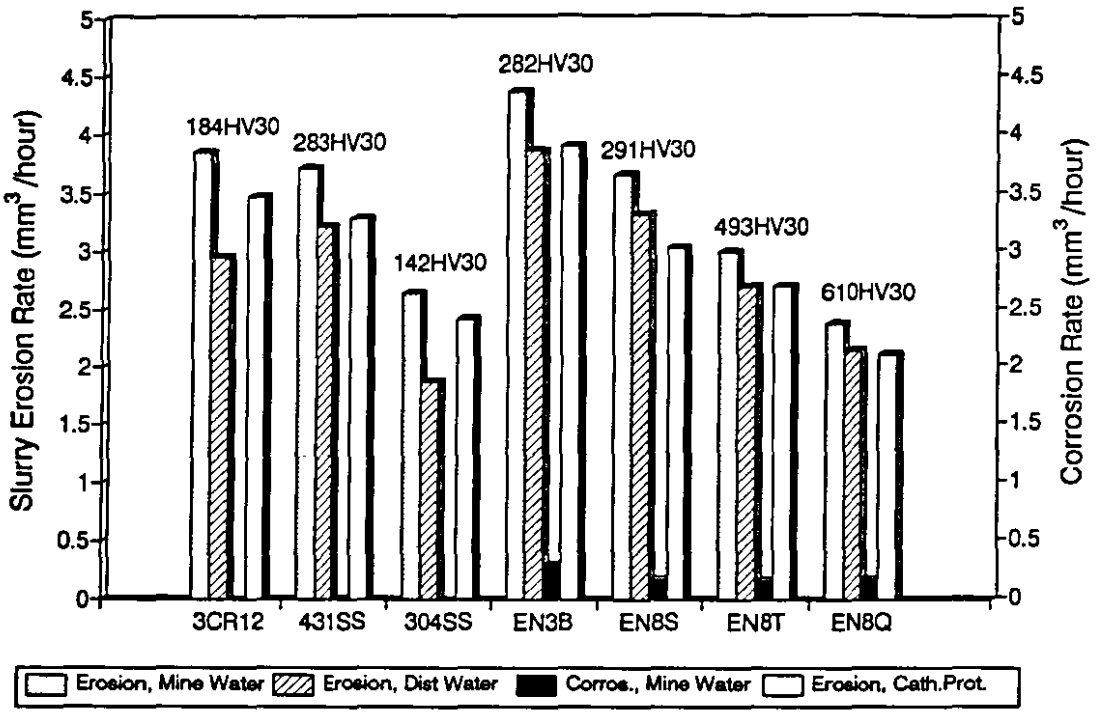

EN8S - EN8 spheroidised, EN8T - EN8 tempered and EN8Q - EN8 quenched

Figure 5.22 Slurry erosion rates of the steels tested under the various conditions; erodent, silica sand (500 μm); carrier fluid, distilled water and synthetic mine water(pH 5.7); temperature, 55°C; impact angle, 90°; impact velocity, 11 m/s. A voltage of -1000 mV was impressed on the specimens for the cathodic protection.

The bar graphs shown above illustrate the insignificant 'pure corrosion' losses experienced by the corrosion resistant steels. It should also be noted that the sum of the 'pure corrosion' components (Corros., Mine Water) of the corrosion resistant steels and their erosion components (Erosion, Dist Water) do not add up their erosion-corrosion losses (Erosion, Mine Water) experienced in the synthetic mine water. For the mild and medium carbon steels however, the 'pure corrosion' components (Corros., Mine Water) and their erosion components (Erosion, Dist Water) do add up to their respective erosion-corrosion losses (Erosion, Mine Water) experienced in the synthetic mine water.

Note also that when the erosion tests are conducted in distilled water, with the application of cathodic protection, there is no real decrease in the slurry erosion rates, in fact there is a significant increase in the erosion rates of the 3CR12 and the 304SS steels.

The nature and extent of the slurry-erosion damage results in there being no noticeable differences between the surfaces tested in distilled water or synthetic mine water. Although it is difficult to characterise the slurry eroded surfaces quantitatively, the micrographs appear to be similar for the steels that have been eroded in the slurry.

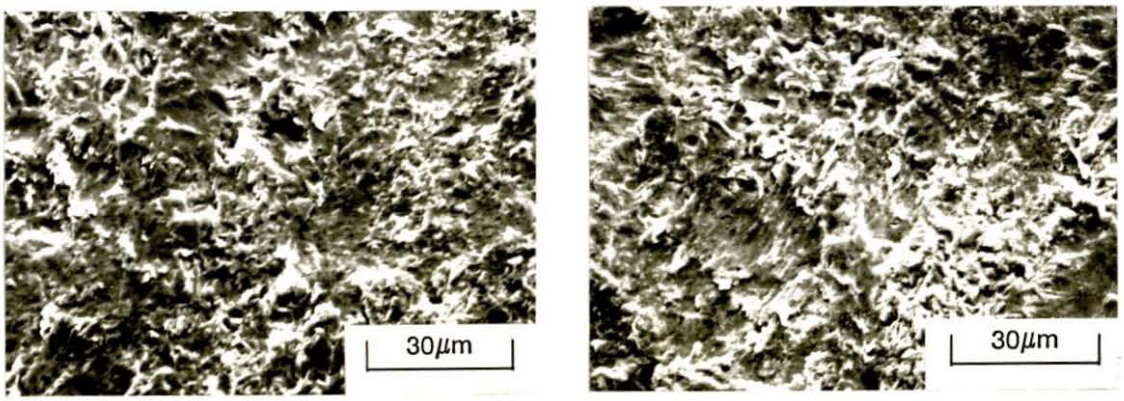

(a) (b)

Figure 5.23 SEM micrographs showing the slurry eroded surfaces of the 304SS specimens eroded at 90° for 60 min.; (a) in distilled water and (b) in synthetic mine water(pH 5.7). Erodent, silica sand (500 μm); temperature, 55°C; impact velocity, 11 m/s.

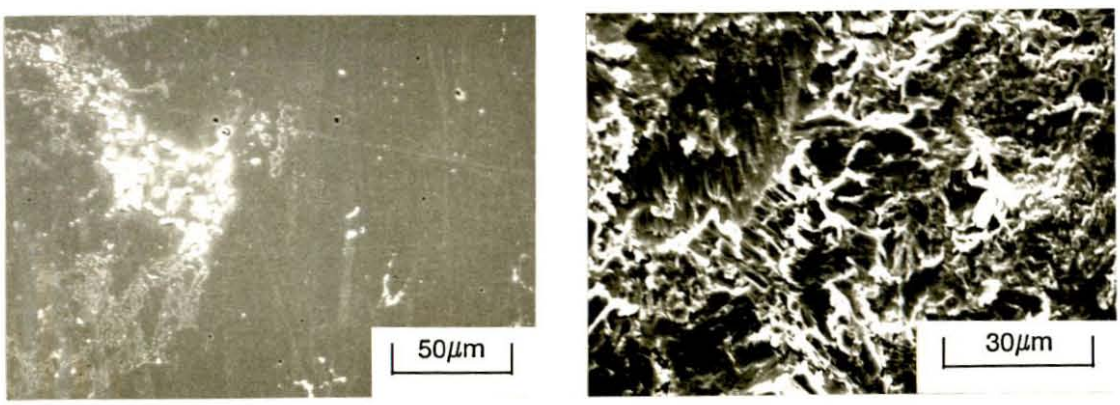

(a) (b)

Figure 5.24 (a) SEM micrograph showing the surface of the 304SS specimen after the corrosion test conducted in the synthetic mine water free from any erodent. (b) SEM micrograph showing the slurry eroded surface of the 304SS specimen eroded at 90° for 60 min. under cathodic protection. The erosion test was conducted in distilled water and a voltage of -1000 mV was impressed on the specimen for the cathodic protection.

There is evidence of considerable material displacement, with shear lips and attached platelets of deformed material being a common feature present on all the surfaces. Some of the platelets contain cracks or tears, suggesting that repeated impacts have occurred on the same material element.

For the corrosion tests conducted in the absence of erodent, on the 304 stainless steel, no noticeable corrosion damage is evident on the specimen surface as shown in fig. 5.24(a). The same unattacked surfaces were observed for the 431 stainless steel and the 3CR12 corrosion resistant steel specimens.

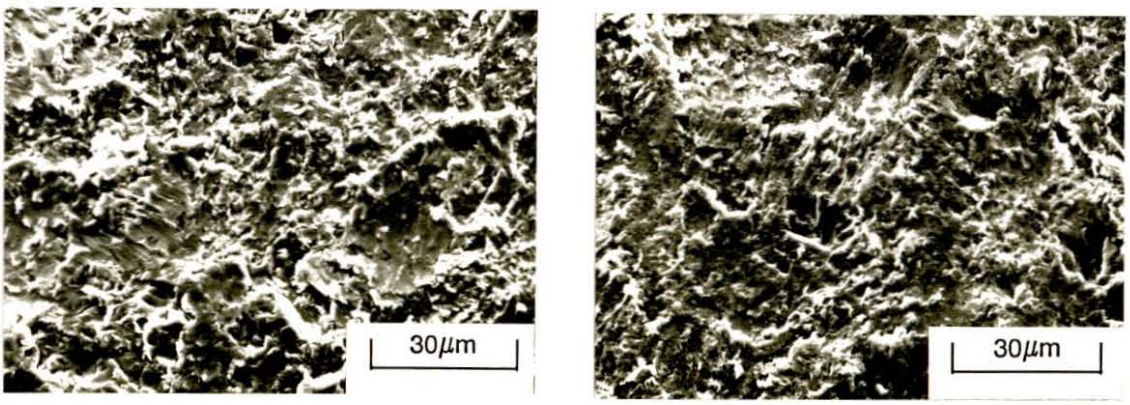

(a) (b)

Figure 5.25 SEM micrographs showing the slurry eroded surfaces of the EN3B (mild steel) specimens eroded at 90° for 60 min.; (a) in distilled water and (b) in synthetic mine water(pH 5.7). Erodent, silica sand (500 μm); temperature, 55°C; impact velocity, 11 m/s.

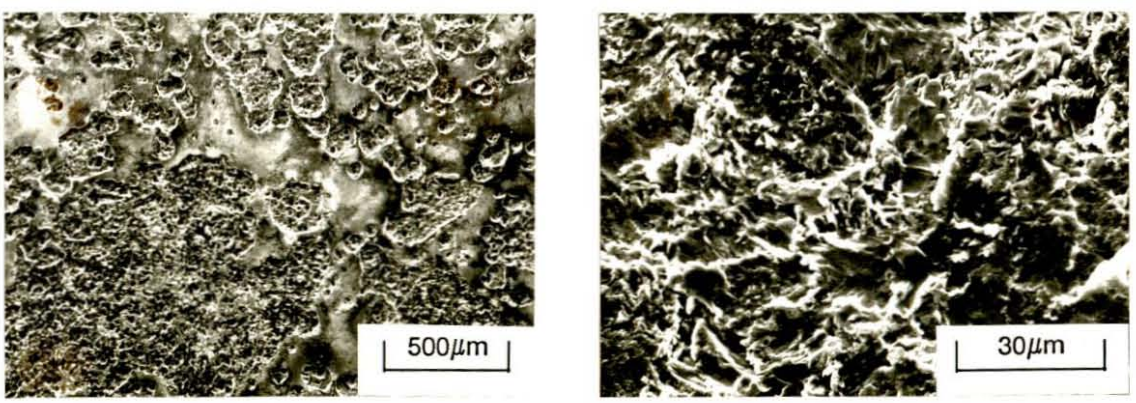

(a) (b)

Figure 5.26 (a) SEM micrograph showing the surface of the EN3B (mild steel) specimen after the corrosion test conducted in the synthetic mine water free from any erodent. (b) SEM micrograph showing the slurry eroded surface of the EN3B (mild steel) specimen eroded at 90° for 60 min. under cathodic protection. The erosion test was conducted in distilled water and a voltage of -1000 mV was impressed on the specimen for the cathodic protection.

In the corrosion tests conducted in the absence of erodent, the mild steel and the medium carbon steels all suffer extensive corrosion damage, mainly due to pitting see figs 5.26(a) and 5.28(a). The extent of the corrosion was similar for the medium carbon steels, in all three different heat treatment conditions.

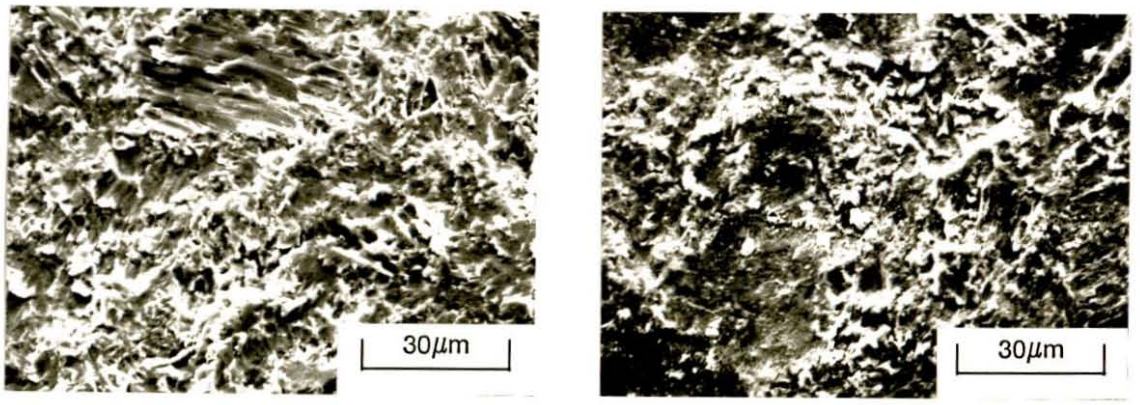

(a) (b)

Figure 5.27 SEM micrographs showing the slurry eroded surfaces of the EN8 spheroidised specimens eroded at 90° for 60 min.; (a) in distilled water and (b) synthetic mine water(pH 5.7). Erodent, silica sand (500 μm); temperature, 55°C; impact velocity, 11 m/s.

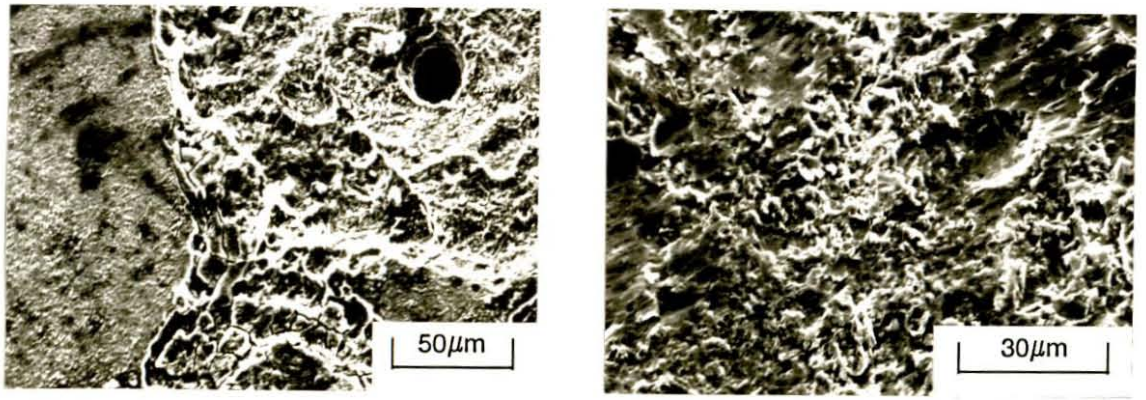

(a) (b)

Figure 5.28 (a) SEM micrograph showing the surface of the EN8 spheroidised specimen after the corrosion test conducted in the synthetic mine water free from any erodent. (b) SEM micrograph showing the slurry eroded surface of the EN8 spheroidised specimen eroded at 90° for 60 min. under cathodic protection. The erosion test was conducted in distilled water and a voltage of -1000 mV was impressed on the specimen for the cathodic protection.

Potentiodynamic tests were conducted on all the steel specimens, the results are presented in figs 5.29 to 5.32, the results for the other steels can be found in the Appendix figs A.27 to A.29. The stainless steels and the 3CR12 specimens both exhibited passivation when tested in the synthetic mine water jet (free of erodent particles).

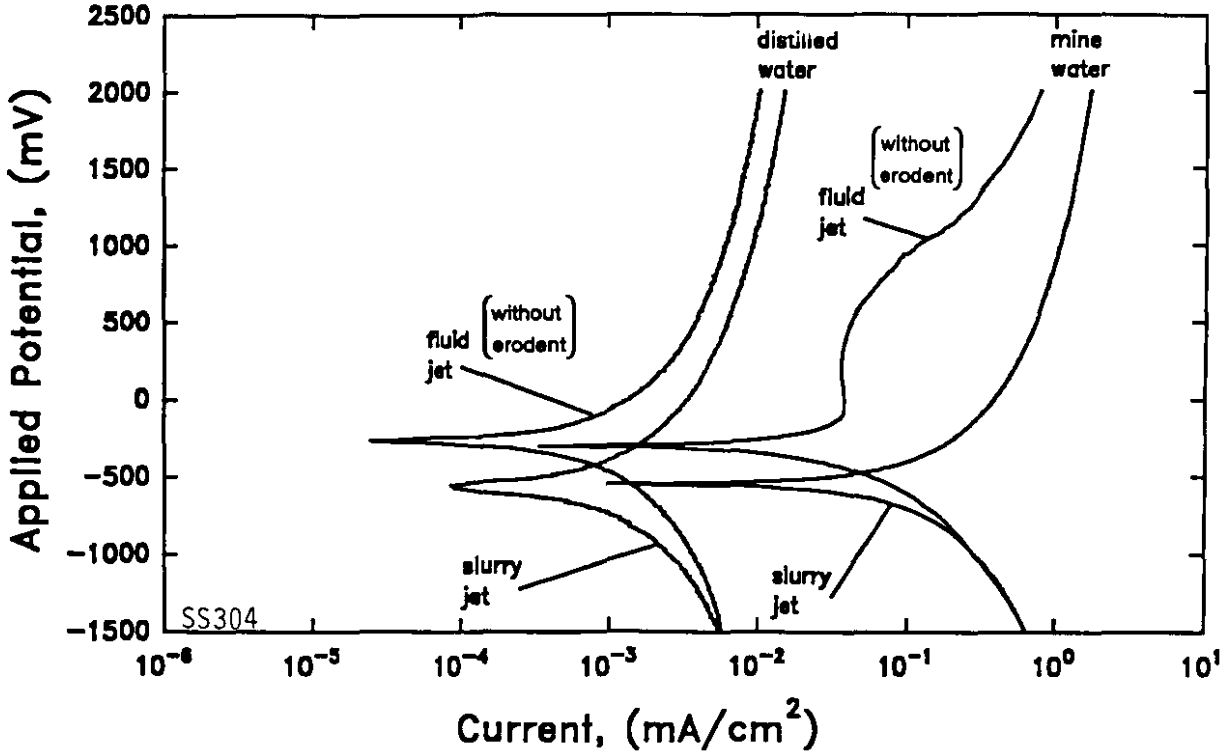

Figure 5.29 304SS - graphs of the current density *vs.* potential scans: Erodent, silica sand (500 μm); carrier fluid, distilled water and synthetic mine water(pH 5.7); temperature, 55°C; impact angle, 90°; impact velocity, 11 m/s; rate of polarisation 4mV/sec.

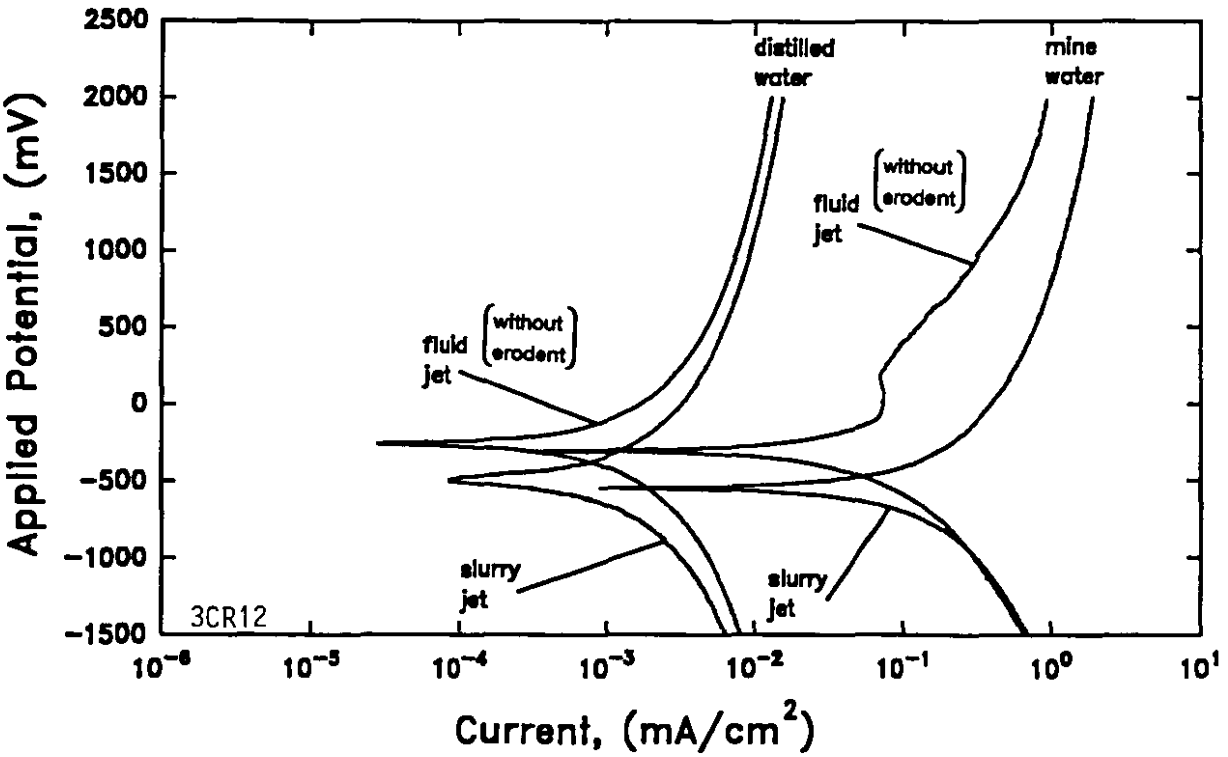

Figure 5.30 3CR12 - graphs of the current density *vs.* potential scans: Erodent, silica sand (500 μm); carrier fluid, distilled water and synthetic mine water(pH 5.7); temperature, 55°C; impact angle, 90°; impact velocity, 11 m/s; rate of polarisation 4mV/sec.

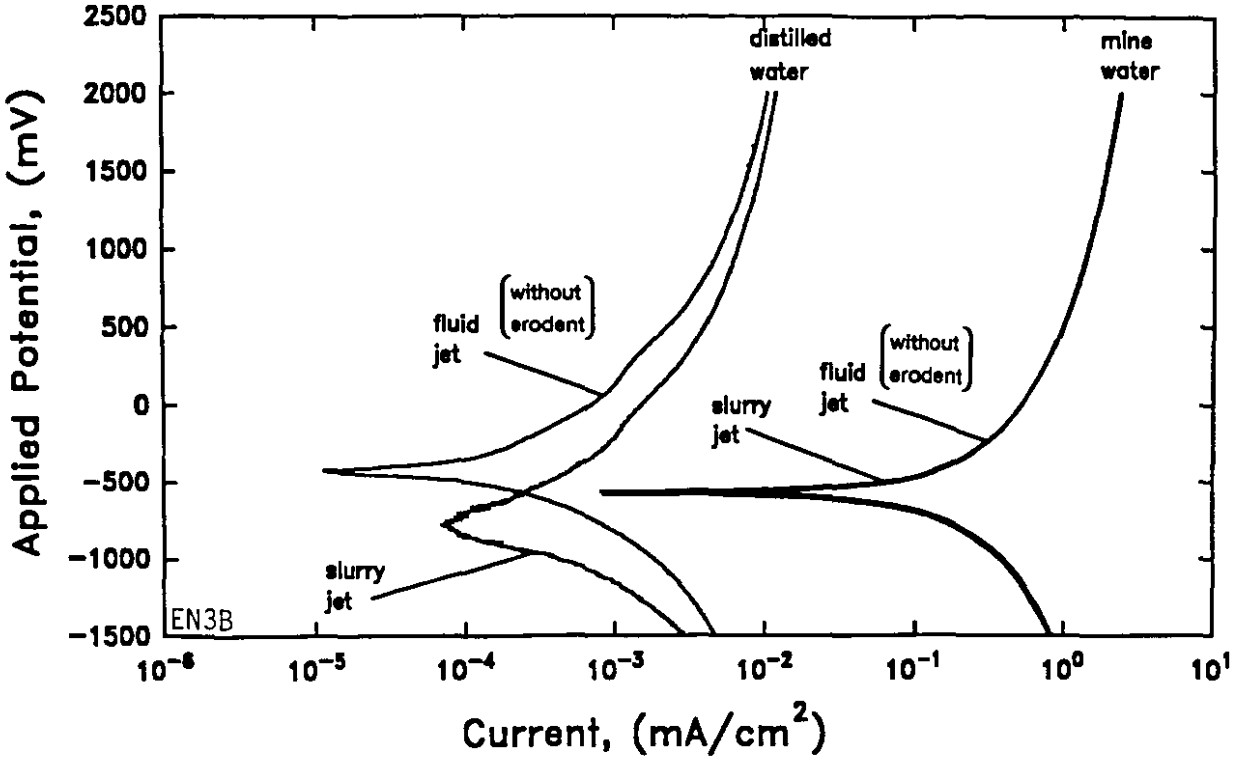

Figure 5.31 EN3B - graphs of the current density *vs.* potential scans: erodent, silica sand (500 μm); carrier fluid, distilled water and synthetic mine water(pH 5.7); temperature, 55°C; impact angle, 90°; impact velocity, 11 m/s; rate of polarisation 4mV/sec.

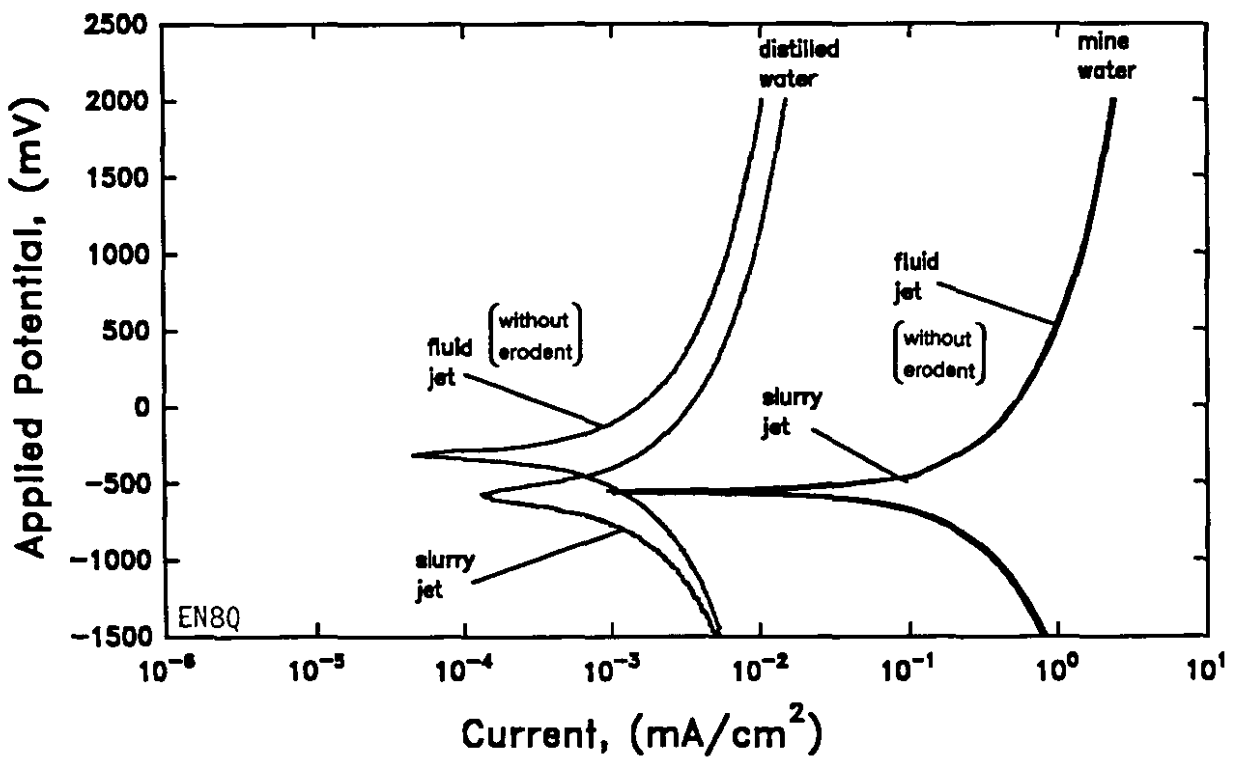

Figure 5.32 EN8 quenched - graphs of the current density *vs.* potential scans: erodent, silica sand (500 μm); carrier fluid, distilled water and synthetic mine water(pH 5.7); temperature, 55°C; impact angle, 90°; impact velocity, 11 m/s; rate of polarisation 4mV/sec.

In the potentiodynamic tests conducted, only the corrosion resistant stainless and 3CR12 steels show any form of passivation when tested in the synthetic mine water (free of erodent), see figs 5.29 to 5.30. Note that when tested in distilled water no passivation is observed for any of the steels.

When these corrosion resistant steels were however subjected to slurry erosion in the synthetic mine water their potentiodynamic behaviours were not much different from that of the low alloy steels under the same conditions, i.e. they had very similar corrosion currents and rest potentials.

The most significant result however is that the potentiodynamic curves of both the mild and the medium carbon steels are the same when tested in the synthetic mine water, with or without the presence of erodent. This trend however is not observed when the tests are conducted in distilled water because of the small corrosion rates experienced in this medium.

CHAPTER 6

DISCUSSION

The impact of a projectile with a metal surface can lead to recoverable, elastic deformation depending on whether the yield stress of the material is exceeded at any point during the impact. A useful guide to the extent of damage expected from projectile impact on a semi-infinite target is provided by the value of a dimensionless group, the Best or Metz number

$$B = \rho V^2/Y$$

where ρ is the density of the target material, V is the impact velocity (11 m/s for the present test conditions) and is a measure of the impact energy of an erodent particle, and Y is the yield stress of the target material and is a measure of the materials resistance to indentation[12].

Table 6.1 shows the type of deformation to be expected for projectile impacts over a wide range of Best numbers.

Best Number	*Damage Regime*
10^{-5}	Quasi-static, elastic
10^{-3}	Plastic deformation starts
10^{1}	Extensive plastic deformation
10^{3}	Hypervelocity phenomena

Table 6.1 Damage regimes expected for Best numbers listed. (after Hutchings[12]).

For the impact of the erodent particles on the aluminium alloys and the aluminium MMCs and the steels the average Best numbers are calculated at 2 and 3 respectively (see Table A.13 and A.14, in the Appendix). The erosion is therefore expected to lie within the plastic regime for the aluminium alloys and the steels tested. This is confirmed by the scanning electron micrographs of the slurry eroded surfaces,

which exhibit microploughing with associated platelet formation on the aluminium alloy and steel surfaces.

6.1 Aluminium Alloys

During the initial period of the slurry erosion the surface undergoes extensive plastic deformation. Until the damage to the surface reaches a steady state there is essentially no volume removal of material from the target. However, no incubation period is observed since this initial stage is very short and not measurable. It was calculated that, on average, the time between erodent particles impacting the same area is 0.1 s (see Appendix page 107). The erodent particles impacting the surface deform and flatten any lips or ridges that have formed, resulting in increasingly thinner platelets which become more vulnerable to being knocked off by subsequent particle impacts.

The ripples formed on the surface of the 1200 series alloy eroded at 40° are shown in fig. 6.1(a) and (b). This is evidence of the ductility which results in lateral displacement of material in the direction of the slurry flow, see also fig. 5.3(a) above. The wave crests are composed of extruded lips which are rather fragile in appearance. Observations by both Hutchings and co-worker[15,16] and Ives and Ruff[17] suggest that the individual crater lips are probably embrittled. Work by Carter, Nobes and Arshak[18] showed that wave crests are substantially hardened and thus concluded that they are embrittled. It is therefore suggested that the major erosive process occurs via removal of the embrittled wave crests rather than from a ductile surface. The material on the wave crests accumulates some critical strain which finally results in material removal.

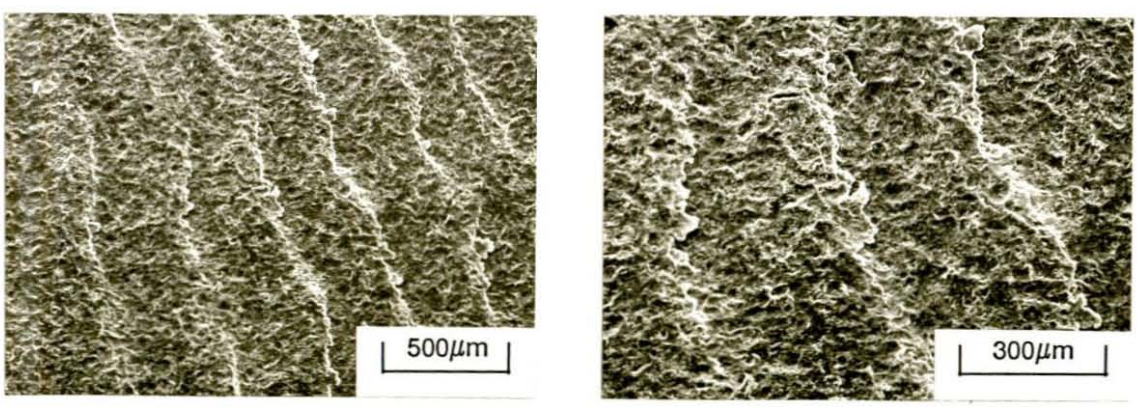

(a) (b)

Figure 6.1 SEM micrographs (a) and (b) showing the ripples that formed on the surface of the 1200 series alloy after slurry erosion at 40° for 10min..

Fig. 6.2(a) and (b) show the edge of the impact area of the 1200 series alloy after slurry erosion at 90°, see also fig. 5.3(b). It is evident from Fig. 6.2(b) that a large amount of material was displaced towards the edge of the impact area, due to the ductility of the 1200 series alloy. The material appears to be layered in this area.

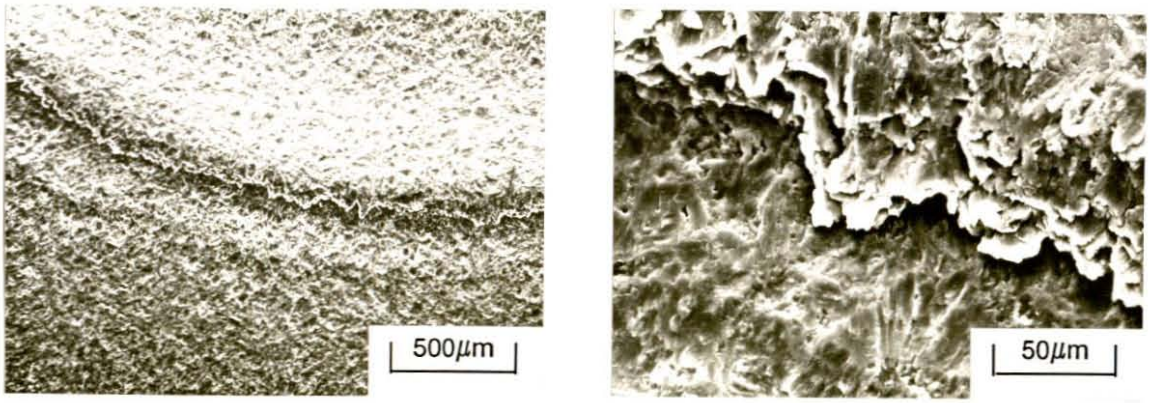

(a) (b)

Figure 6.2 SEM micrographs (a) and (b) showing the edge of the impact crater that formed on the surface of the 1200 series alloy after slurry erosion at 90° for 10min..

The impact sites in general have platelets or lips extruded at their edges, to a greater or lesser degree depending on the ductility of the alloy. The removal of the plastically extruded platelets or lips formed at the edges of the impact craters, as described above, is the mechanism which accounts for most of the target material volume loss from mechanical (as opposed to electrochemical) action.

It may be expected, under the steady state conditions, that the surface would work-harden rapidly, due to the high strains caused by the continuously impacting erodent particles. Material loss results when sufficient strain has been imparted to the material by the erosion events.

As noted earlier indentation hardness is frequently not a valid parameter to describe erosion rate variations within an alloy system. For this reason the erosion rates of the aluminium alloys have been related to the energy required to remove material from the target surface, since this parameter takes into account the materials resistance to indentation, its ductility and its strain to failure. The materials resistance to indentation or its resistance to plastic deformation determines the amount of material displaced and or removed by the impact events. The ductility and the strain to failure values determine whether any material will be removed by an impact event.

The work to fracture values obtained for the aluminium alloys have been used to produce the graph below, (fig. 6.3), showing the slurry erosion rates, measured in distilled water, *vs*. work to fracture. This is related to the area beneath a material's

tensile load-extension curve and is an indication of its toughness or work to fracture. The general trend that can be observed is that the slurry erosion rates decrease with increasing work to fracture values. This trend is particularly apparent in the case of the non heat treatable alloys (Al1200, .Al3004 and Al5083), that rely only on work hardening for strengthening.

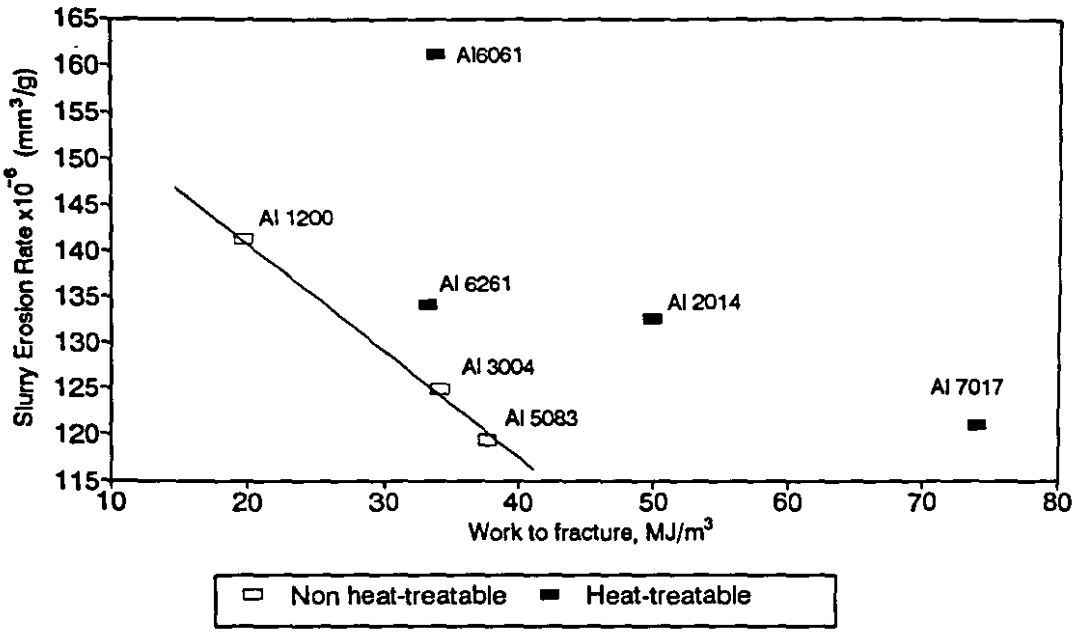

Figure 6.3 Slurry erosion rates of the aluminium alloys tested plotted as a function of work to fracture; erodent, silica sand (500 μm); carrier fluid, distilled water; temperature, 55°C; impact angle, 90°; impact velocity, 11 m/s.

In general lower slurry erosion rates were not observed for the non heat-treatable aluminium alloys (Al1070, Al1200, Al3004 and Al5083) as compared to the heat-treatable aluminium alloys (Al2014, Al6061, Al6261, Al7017 and Al7075), Table 5.1, as found for abrasion by Meyer-Rodenbeck and Ball[109].

In the abrasion tests performed by Meyer-Rodenbeck and Ball[109], the nonheat-treatable wrought alloys were found to exhibit ductile micro-deformation characteristics, whilst heat-treatable alloys, had the best dry abrasion resistance values, due to their better combinations of strength, hardness and toughness.

The slurry erosion resistance of the aluminium alloys may be maximised by designing an aluminium alloy with a good combination of hardness, strength and strain to fracture. High strength and strain to fracture values result in high work to fracture values.

Aluminium is a very reactive metal with a high affinity for oxygen. The metal is nevertheless highly resistant to most environments due to the inert and protective character of the aluminium oxide film which within seconds attains a thickness of

about 10Å on freshly exposed metal, in air [114]. In aqueous environments the oxide layer forms more rapidly and is thicker. A duplex film generally forms in wet environments; the continuous oxide layer closest to the metal surface changes to hydroxylated film at the solid/gas interface[84].

The addition of the salts to the distilled water, to create the synthetic mine water, results in an increase in electrical conductivity of the liquid, which promotes the mechanisms of electrochemical corrosion.

The increase in current density associated with the increased slurry erosion rates experienced in the synthetic mine water over the distilled water, illustrates the significance of the corrosion component when coupled with slurry erosion. The material loss increased by as much as 42% in the case of the 1200 aluminium alloy (Table 5.1) when eroded in the presence of synthetic mine water instead of distilled water. As mentioned above the aluminium alloys are generally known to be corrosion resistant, due to the rapid formation of a continuous protective oxide layer, but this layer is continuously damaged and removed by the erodent particles, resulting in the high slurry erosion-corrosion losses experienced.

Meyer-Rodenbeck *et al's* results show that as corrosion becomes the more predominant wear factor in an abrasive-corrosive wear environment, overall wear resistance is determined primarily by the corrosion properties of the alloy series, whilst the dry abrasion properties of individual alloys within that series becomes less important. Meyer-Rodenbeck *et al.*[109] found that the corrosion attack on the aluminium alloys is not uniform, but is confined to localised sites on the metal surface where heterogeneity of either the metal or the corrosive medium exists and passivation is discontinuous, (fig. 6.4). The more pure aluminium alloys have fewer heterogeneities and therefore have more complete and continuous passive films. In aqueous solutions the steady state thickness of the film is governed by its dissolution rate into the environment and by the rate at which the film can conduct ions. The integrity of the oxide film is a function of the metal composition and microstructure as well as the presence of stresses[123].

Damage of the passive film results in localised anodic attack of the exposed metal. The greater the corrosion protection provided by the passive layer, to the underlying material, that surrounds the impact damage site, the greater will be the potential driving the anodic reaction. This will be discussed in greater detail at the end of the chapter. The corrosion component of the erosion-corrosion wear damage is therefore very dependant on the nature and extent of the passive layer as well as the repassivation kinetics.

In the case of aluminium alloys, the most common form of corrosive attack is localised corrosion or pitting. However, under slurry erosion conditions the surface is constantly changing and hence localised conditions are not allowed to develop. This is illustrated by the fact that the rest potential gradually decreases, at the start of each potential *vs.* time test (figs. 5.15 and 5.16), due to the gradual breakdown of any existing passive film. The decrease in potential also occurs due to the increase in surface area brought about by the slurry erosion.

As a control the aluminium alloys were tested for 60 minutes in only the synthetic mine water jet (free of erodent particles), but there was no measurable mass loss, fig. 6.5. Discolouration of the surface was observed owing to build up of corrosion products and/or salts on the surface. The SEM micrograph in fig. 6.4, is typical of an aluminium alloy specimen surface after only 60 minutes of corrosion. Preferential corrosion of the matrix around a constituent particles as well as the build up of corrosion products was observed.

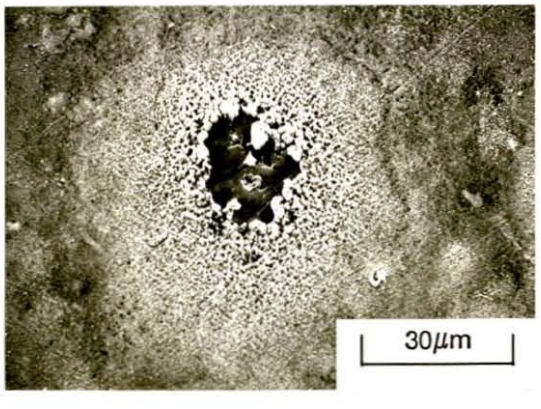

Figure 6.4 The corrosion on a polished Al5083 surface after 60 min. of corrosion in the synthetic mine water jet.

The value of the corrosion potential is a good indication of the electrochemical behaviour and state of the specimen surface during slurry wear. The potentials of the specimens are more negative under the slurry erosion-corrosion conditions as compared with corrosion potential. It can be seen from the potential *vs.* time curves of the various aluminium alloys, presented in figs. 5.15 and 5.16, that during the initial 20 minutes of the test there is a gradual drop in potential, with the rest potential becoming gradually more negative until a steady state is reached. There is a distinct change in the rest potential at 60 min., when only the carrier fluid is left to impinge on the surface. When the erodent is once again added to the impacting jet, at 120 min. the rest potential immediately drops to more negative potentials.

The aluminium 5083 alloy was used to generate a wear rate *vs.* time pattern, which is a qualitative description of the shape of the erosion-corrosion rate time curve, in

terms of the several stages of which it may be composed. It can be seen from fig. 6.5 that there is no incubation period for the slurry erosion and that the cumulative erosion loss is linear. The rest potential in distilled water and in synthetic mine water gradually becomes more negative and levels off after approximately 15 minutes. This is as a result of the oxide layer, which was present at the start of the test, being removed as well as a gradual increase in surface area due to the slurry erosion. There was no measurable mass loss while the 5083 alloy was only subjected to the synthetic mine water fluid jet, (fig. 6.5).

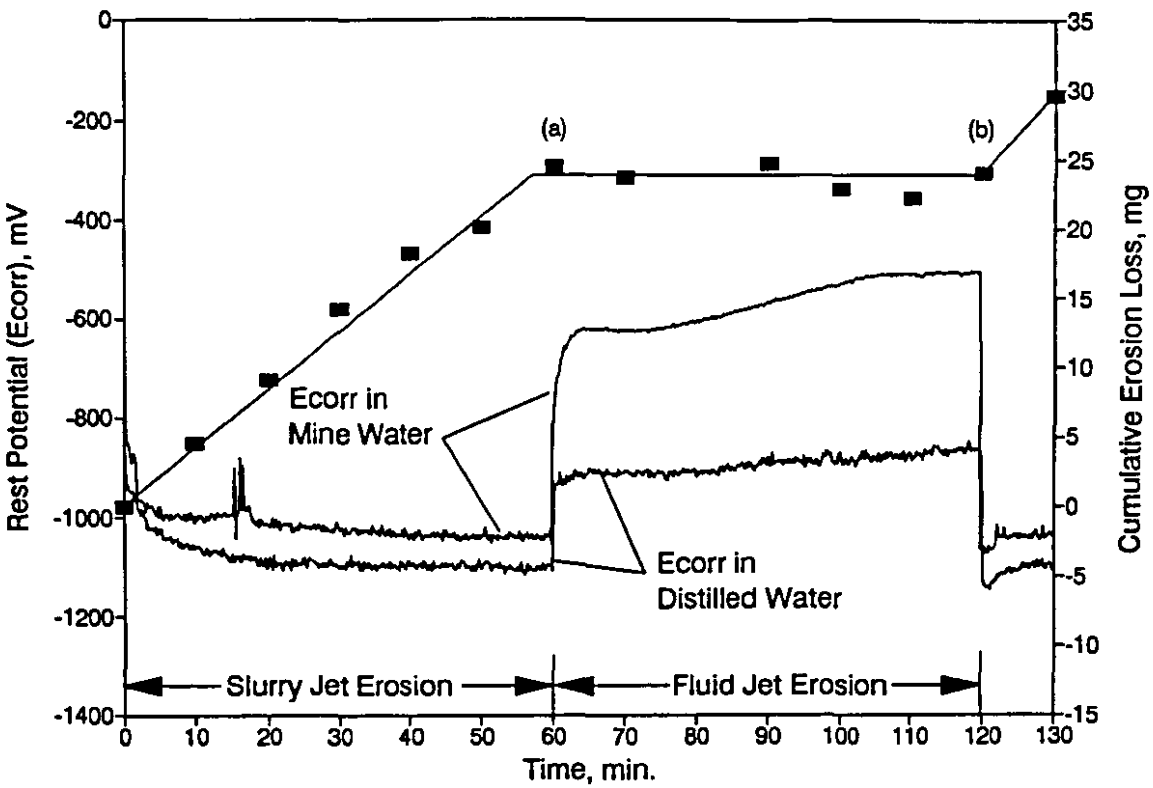

Figure 6.5 The potential *vs.* time curves of the 5083 aluminium alloy, tested in distilled water and synthetic mine water at 55°C with 500 μm silica sand as erodent, are presented with the cumulative slurry erosion loss measurements of the 5083 series alloy tested in synthetic mine water.

Scanning electron microscopy (SEM) micrographs of the steady state slurry eroded surfaces of the 5083 series alloy are presented in figs. 6.6(a) and (b). Figure 6.6(a) illustrates the eroded surface after the first 60 minutes of the test and fig. 6.6(b) illustrates the surface after 120 minutes, these correspond respectively to points (a) and (b) on the graph in fig. 6.5.

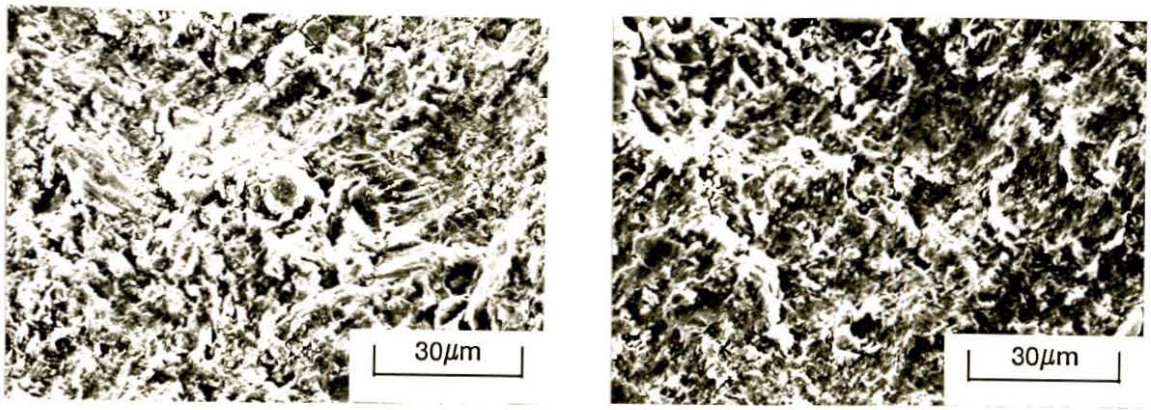

(a) (b)

Figure 6.6 SEM micrographs of the 5083 series alloy after, (a) 60 minutes of erosion-corrosion and (b) a further 60 minutes of corrosion.

6.2 Aluminium Metal Matrix Composites

For large impact angles the mechanism of slurry erosion is one of repeated impact wear. For ductile materials the impacting particles result in plastic deformation, which displaces material to the edges of the impact site, forming a lip. Subsequent particles that impact the edges, or lips that have formed, result in the surface layer being heavily deformed leading to microfractures. Further erodent particle impacts thereafter removes material. The softer aluminium alloys experience higher rates of material removal, (fig. 6.7), and those with higher work to fracture values exhibit lower slurry erosion rates, (fig. 6.3).

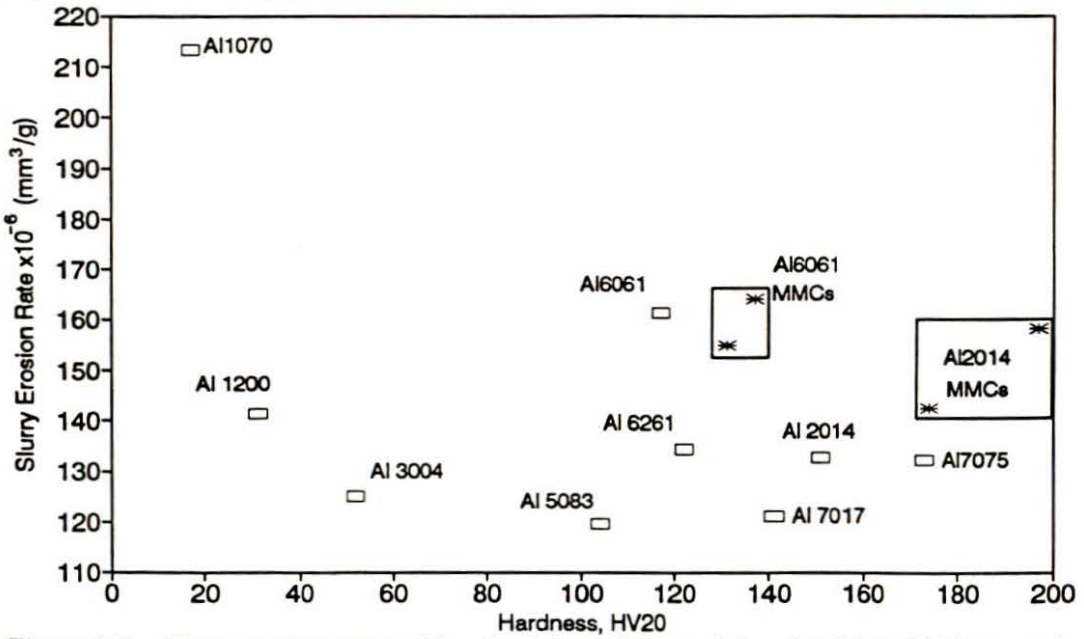

Figure 6.7 Slurry erosion rates of the aluminium alloys and the aluminium MMCs tested, plotted as a function of initial surface hardness; erodent, silica sand (500 μm); carrier fluid, distilled water; temperature, 55°C; impact angle, 90°; impact velocity, 11 m/s.

The aluminium metal matrix composites consisted of a ductile metal reinforced with a brittle ceramic. The addition of reinforcing ceramic particulates results in increased macrohardness values and reduced ductility[107] as a result of matrix constraint. This increase in hardness reduces the amount of plastic deformation experienced by the material and should be a factor resulting in reduced erosion rates experienced by the MMCs. Regions of matrix constrained by the reinforcing particles were more susceptible to wastage[82].

The Al6061 with 15wt% Al_2O_3 reinforcing particles experiences a substantial decrease in slurry erosion rate for both the 90° and the 60° impact angles, (figs 5.17 and 5.18). The Al6061 with 15wt% Al_2O_3 reinforcing particles does not experience as a large a drop in work to fracture, due to the presence of the reinforcement, as do the other MMCs tested. This, along with the increase in hardness and the matrix protection provided by the particles, results in this particular MMC showing improved slurry erosion resistance over the unreinforced 6061 aluminium matrix alloy.

The remaining aluminium MMCs all experience substantially reduced work to fracture levels, as compared with their respective matrix alloys. As a result the aluminium MMCs experience increased erosion rates with the addition of the reinforcement particles. This result is in agreement with previous studies[79,80,81]. The erosion rates of the MMCs are however still of the same order of magnitude as that of the matrix alloys, (fig. 6.7).

Reductions in the airborne erosion resistance of aluminium MMCs was also observed by Wilson *et al.*[107] and was found to relate to the strain energy required to initiate microfracture in a material. Both the Al2014 and the Al6061 composite materials displayed good correlations between their erosion rates and their work to fracture values[107]. The composites with small fracture energies exhibited rapid material losses, as opposed to the unreinforced alloys having the greater fracture energy values and minimal slurry erosion losses[107].

The lower slurry erosion rate of the matrix alloys compared with the MMCs tested is also a result of the reinforcing particles in the MMCs assisting microchip-formation rather than allowing material displacement. Fracture of the reinforcing particles also has a detrimental effect on the erosion resistance of the MMCs, (fig. 5.19).

Few reinforcement particles remained visible on the target surfaces, which implies that the reinforcement particles are being completely removed and play a principal part in the material-removal process. The overall appearances of the steady state surfaces are typical for erosion of the matrix alloys.

For slurry erosion the protrusion of the particulates on the surface are expected to make the formation of a coherent passivating layer difficult, however this insignificant in comparison to the damage to the passivating layer caused by the impacting erodent particles. No significant increases in corrosion rates were observed with the addition of reinforcement to the matrix alloys, figs 5.20 and A.25 (in the Appendix). However longer term corrosion tests without the presence of erosion may result in differing corrosion rates due to increased galvanic effects and pitting, resulting from the mismatched electrochemical potentials between the matrix and the reinforcement.

6.3 Steels

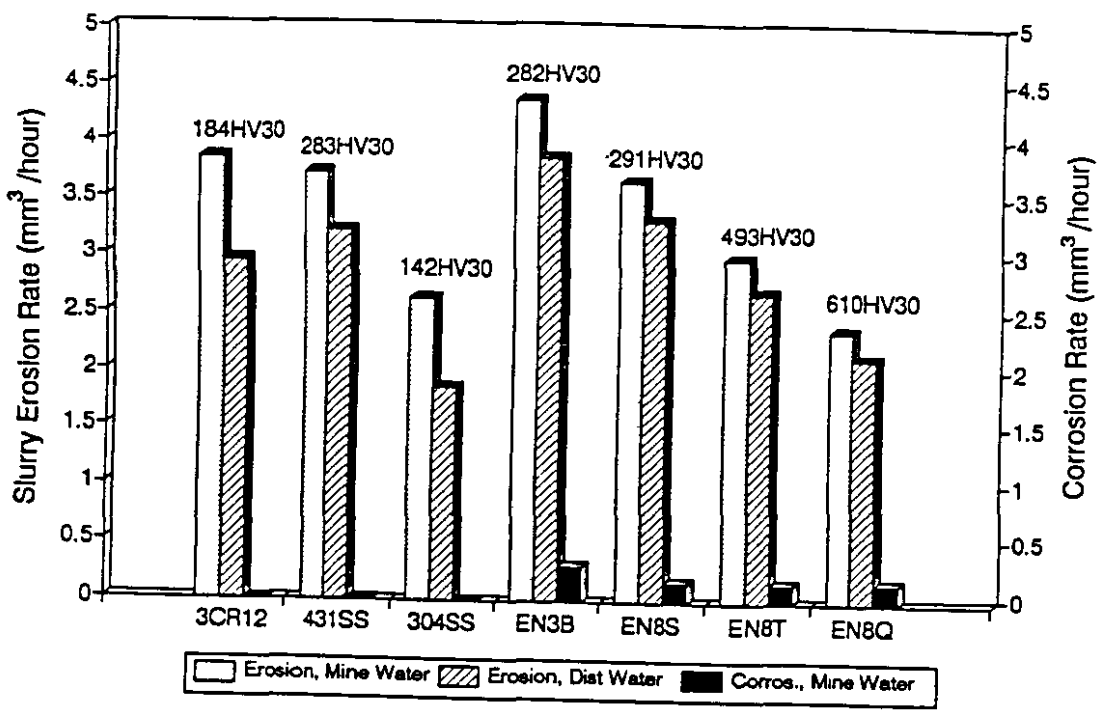

EN8S - EN8 spheroidised, EN8T - EN8 tempered and EN8Q - EN8 quenched

Figure 6.8 Slurry erosion rates of the steels tested under the various conditions; erodent, silica sand (500 μm); carrier fluid, distilled water and synthetic mine water(pH 5.7); temperature, 55°C; impact angle, 90°; impact velocity, 11 m/s.

The 304 stainless steel is an austenitic steel, hence the steel is strengthened by cold work and has a good work hardening capacity. The good slurry erosion resistance of the 304SS, considering its relatively low hardness (fig. 6.8), can be attributed to its good work hardening capacity.

The EN8 steels show improved slurry erosion resistances with increasing hardness. However McCabe *et al.*[162], reported increasing airborne erosion rates with increasing

hardness. These seemingly contradictory results could be because, in the tests conducted by McCabe *et al.*, very high strain rates were experienced, since the impact velocity was 99 m/s. At these very high strain rates the martensitic structure of the steel starts to behave like a brittle ceramic.

The presence of chromium greatly improves the corrosion resistance of the steel by forming a very thin stable oxide film on the surface[115]. The 304SS, the 431SS and the 3CR12 specimens depend on the integrity of their oxide layers for their corrosion resistant properties. It is as a result of these properties that no significant mass loss is recorded for the corrosion tests performed on the stainless steels or the 3CR12, fig. 6.8. The oxide layers in these materials act as diffusion barriers to the corrosive ions and oxygen.

During slurry erosion however the action of erodent particles damages the protective oxide layers on the 304SS, the 431SS and 3CR12 specimen surfaces. This results in areas of 'fresh' metal being continuously exposed to corrosion under the action of the slurry. These exposed areas are surrounded by areas protected by an oxide layer which act as cathodic sites in relation to the 'exposed, fresh' metal. Hence there is a substantial driving force for corrosion at the 'exposed' anodic sites.

It is for this reason that the 304SS and the 3CR12 specimens exhibit such increased slurry erosion rates, when eroded in the presence of the synthetic mine water as opposed to distilled water, see fig. 6.8. .

For the EN3B (mild) steel and EN8 (medium carbon) steel specimens the slurry erosion-corrosion rates are equal to the sum of their individual erosion rates in distilled water and their corrosion rates. Neither the EN3B nor the EN8 steels showed any signs of passivation in any of the potentiodynamic tests conducted in the synthetic mine water (free of erodent), figs 5.31 to 5.32. This is because the oxide layers that form on these steels do not act as a diffusion barrier to oxygen and/or the corrosive ions. Hence the removal of the oxide layers due to erosion does not cause an acceleration in the 'erosion-corrosion' rate in the synthetic mine water, i.e. the potentiodynamic scans conducted under slurry conditions are essentially the same as those conducted in the fluid jet only, see figs 5.31 to 5.32. In the case of the EN3B and the EN8 steels the metal wastage in the synthetic mine water slurry should be referred to as 'erosion + corrosion' not erosion-corrosion, i.e. the combined effect is not *synergistic* as in the case of the corrosion resistant 304SS and 3CR12.

The differences in corrosion behaviour between the corrosion resistant steels and the low alloy steels, when tested in the synthetic mine water, are illustrated below by superimposing the potentiostatic tests conducted on the 304SS and EN3B. Figure

6.9 shows that for the tests conducted in the fluid jet, the 304SS will passivate and the corrosion current densities are much smaller than those measured for the EN3B (mild steel). However when the 304SS is tested in the synthetic mine water slurry its has essentially the same current density *vs.* potential behaviour as the EN3B specimen.

As noted earlier the 304SS specimen exhibited the lowest slurry erosion rate when tested in distilled water, this however changes when tested in the synthetic mine water, see fig. 6.8. The slurry erosion rate of the 304 stainless steel increases by 41%, when tested in the synthetic mine water, due to the corrosion component. The EN8 steel has the best slurry erosion resistance of the steels tested in the synthetic mine water, because it does not exhibit the same synergistic behaviour as do the corrosion resistant steels.

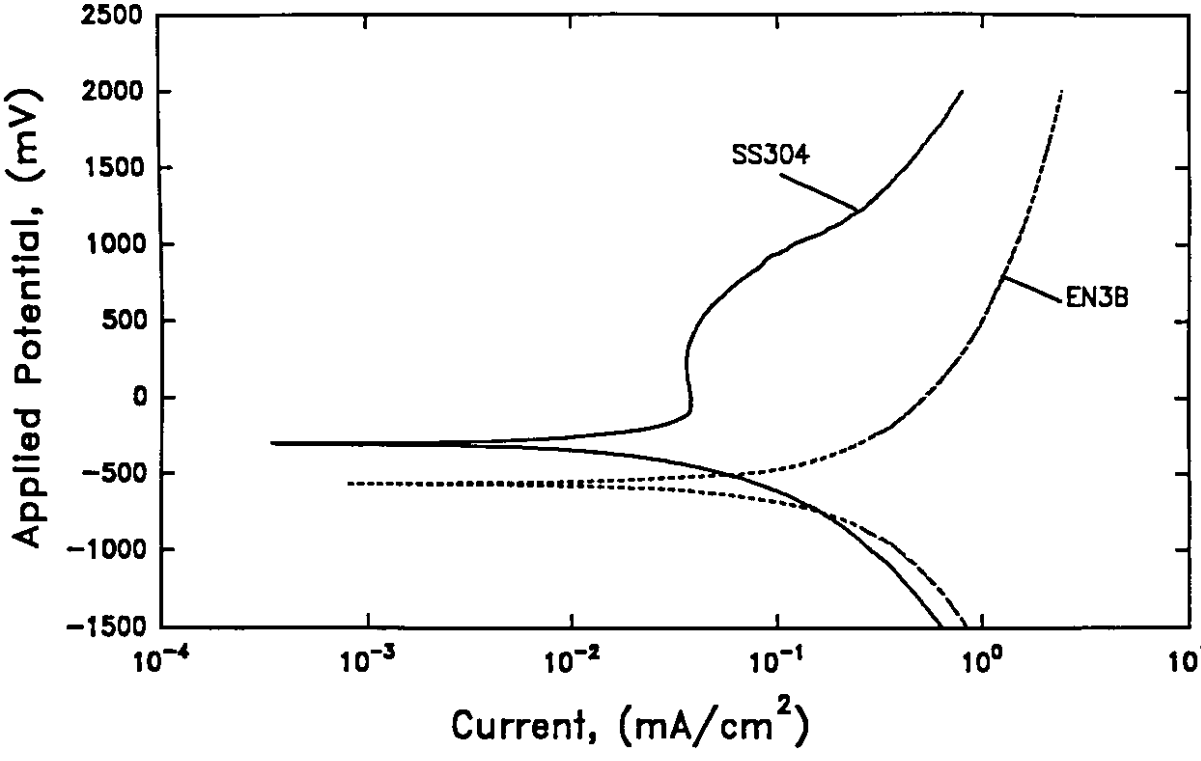

Figure 6.9 Graphs of the current density *vs.* potential scans of the 304SS and the EN3B tested in the synthetic mine water (free of erodent). Temperature, 55°C; impact angle, 90°; impact velocity, 11 m/s; rate of polarisation 4mV/sec.

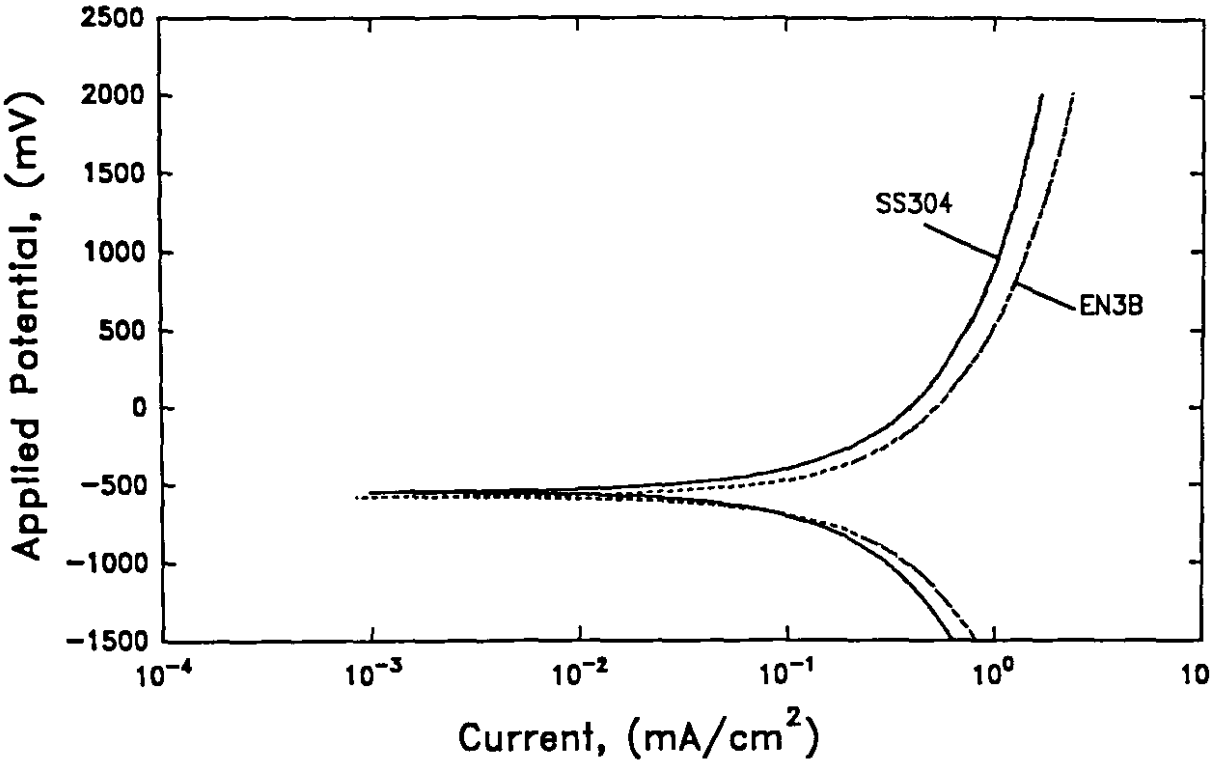

Figure 6.10 Graphs of the current density *vs.* potential scans of the 304SS and the EN3B tested in the synthetic mine water slurry. Erodent, silica sand (500 μm); temperature, 55°C; impact angle, 90°; impact velocity, 11 m/s; rate of polarisation 4mV/sec.

When the steels are tested in distilled water the driving force for corrosion is much smaller than for the tests conducted in synthetic mine water, due to the absence of corrosive ions. The corrosion currents are much smaller and for this reason there is not sufficient driving force for the corrosion resistant steels to exhibit passivation behaviour. It has been noted that the potentiodynamic curves of the mild and the medium carbon steels (in the different heat treated conditions) are the same, whether tested in the synthetic mine water jet with or without erodent, see figs. 5.31 and 5.32 as well as figs A.28 and A.29 in the Appendix. It is reasoned that the oxide layer that forms under the purely corrosive (free of erodent) conditions does not reduce the corrosion rate, i.e. the corrosion rate is the same in the corrosive slurry. This trend is not observed in distilled water, the corrosion currents are higher in the presence of the slurry than they are without any erodent. In distilled water the conductivity of the solution is lower and there are fewer corrosive species present, resulting in negligible corrosion, which is accelerated by erodent particles damaging the surface, exposing fresh metal to corrosion. When highly corrosive ions are added to the system, in sufficient quantities, such as chlorides and sulphates, the corrosion will also be accelerated. The potentiodynamic curves obtained indicate that the synthetic mine

water results in a corrosion rate that is sufficiently high that it is not noticeably accelerated by damage resulting from the erodent addition.

Under cathodic protection conditions the 304SS and 3CR12 specimens exhibit increased slurry erosion rates compared to their erosion rates in distilled water, see fig. 5.22. This may be ascribed to the hydrogen embrittlement of these steels due to the generation of hydrogen on the metal surface which in turn is tribosorbed into the metal lattice at the impact sites by dislocations, as described by Wandke *et al.*[155].

However Swisher[85] reports, in his work on alloy corrosion and slurry erosion in coal preparation plants, that success was achieved in cathodically protecting two wear-resistant alloys; Hadfield's manganese steel and high-Cr cast iron. The slurry erosion-corrosion metal wastage rate for the unprotected cast iron specimen was a factor of 30 higher and a factor of 10 improvement with cathodic protection of the Hadfield steel specimens was obtained.

6.4 General

Erosion rates are complex functions of impact conditions and specimen structure and properties[165].

The ability of a material to withstand strain and to resist microfracture is influenced by its strain hardening capacity, as described by Ball[165,166]. The hypothetical material II, representing a soft ductile metal, will have a much lower work to fracture value than the material III, having a good combination of strength and strain hardening-capacity. Material II will therefore have a lower erosion resistance than material III. Thus Ball's model which relates abrasive wear to the strain-hardening capacity for different classes of materials can also be applied to the erosive wear of metals.

The slurry erosion rates of the aluminium alloys (which can be likened to Material II) are about three times that of the steels tested (having characteristics of Material III).

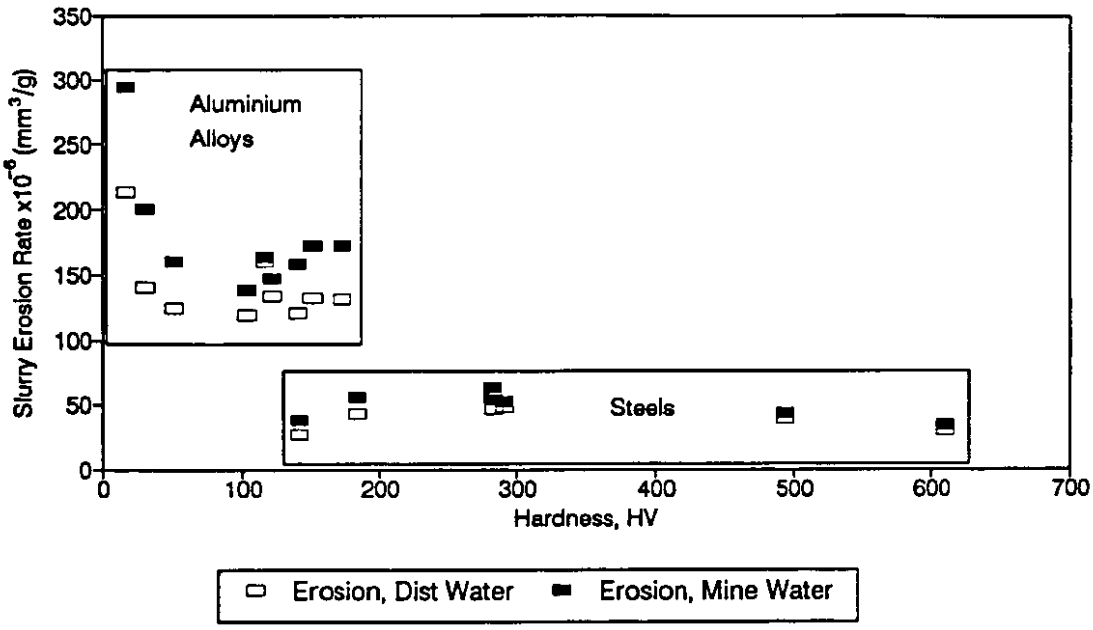

Figure 6.11 Graph showing the relative slurry erosion rates of the aluminium alloys and steels tested; erodent, silica sand (500 μm); carrier fluid, distilled water and synthetic mine water(pH 5.7); temperature, 55°C; impact angle, 90°; impact velocity, 11 m/s.

When the metal is subject to erosive wear each mechanical event will cause rupture or removal of the oxide film in a localised region of the surface thereby exposing bare metal to the environment. The electrochemical processes which occur when fresh metal surfaces are generated in the presence of aqueous electrolytes may simply involve repassivation of the metal. Alternatively the processes can lead to rapid

localised corrosion of the newly created metal surface or to accelerated hydrogen evolution[123].

A fundamental principle of corrosion is that the sum of the cathodic reactions must equal the sum of the rates of the anodic reactions, irrespective of whether the attack is uniform or localised,

$$\Sigma I_a = \Sigma I_c \,, \tag{6.1}$$

where I_a is the anodic current and I_c is the cathodic current. If the attack is uniform, assuming that there is only a single predominantly anodic and cathodic reaction, then

$$\frac{I_a}{S_a} = \frac{I_c}{S_c} \quad \text{or,} \quad i_a = i_c \tag{6.2}$$

since the area of the cathode S_c equals the area of the anode S_a, i_a and i_c being the anodic and cathodic current densities respectively. On the other hand if the attack is localised $S_a < S_c$, and

$$i_a > i_c \quad \text{or,} \quad \frac{i_a}{i_c} > 1 \tag{6.3}$$

and the larger the ratio $i_a : i_c$ the more intense the attack.

Thus the localised attack involves a corrosion cell consisting of a large cathodic area and a small anodic area, and since I_a must equal I_c, the effect will become more pronounced the higher the rate of the cathodic process and the larger the effective area of the cathode[114].

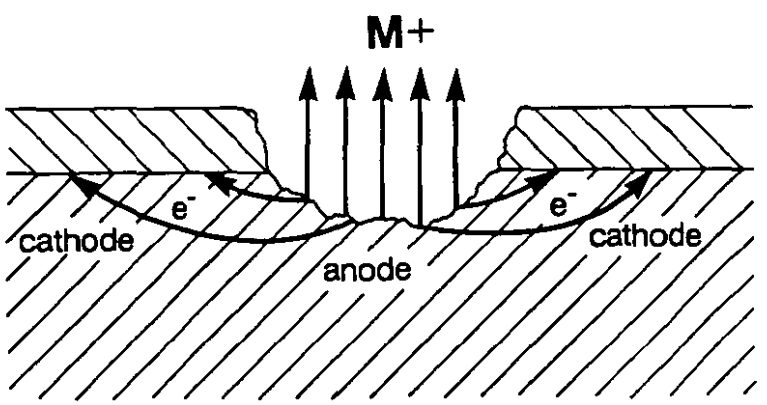

Figure 6.12 A discontinuity in the oxide film, due to erosion damage, results in an active-passive cell which leads to intense localised attack on the active area.

Shreir[114] states that the most significant form of erosion-corrosion is the constant removal of protective films from the metal's surface, thus resulting in localised attack at the areas at which the film is removed.

Evidence of the increased in the corrosion currents as a result of the damage to the passive layers can be seen in the potentiodynamic scans generated under fluid jet only and slurry jet conditions, (figs 5.13, A.17 to A.24, 5.29, 5.30 and A.27). The corrosion currents are shown to increase, i.e. the curves shift to the right when subjected to erosion damage as well as corrosion. The potentials also become more negative under the slurry conditions.

This change in potential is also observed for the potential *vs.* time curves. The changes in potential cannot be used to quantify the changes in reaction rates, but serve to illustrate that there is a change in the electrochemical behaviour when changing from erosion-corrosion to corrosion.

A graphical explanation for this can given by comparing the E *vs.* log$i$ curves of a hypothetical corrosion resistant metal with the potentiodynamic scans performed. The potential *vs.* log$i$ curves for the corrosion of the metal in a reducing environment is depicted in fig. 6.13.

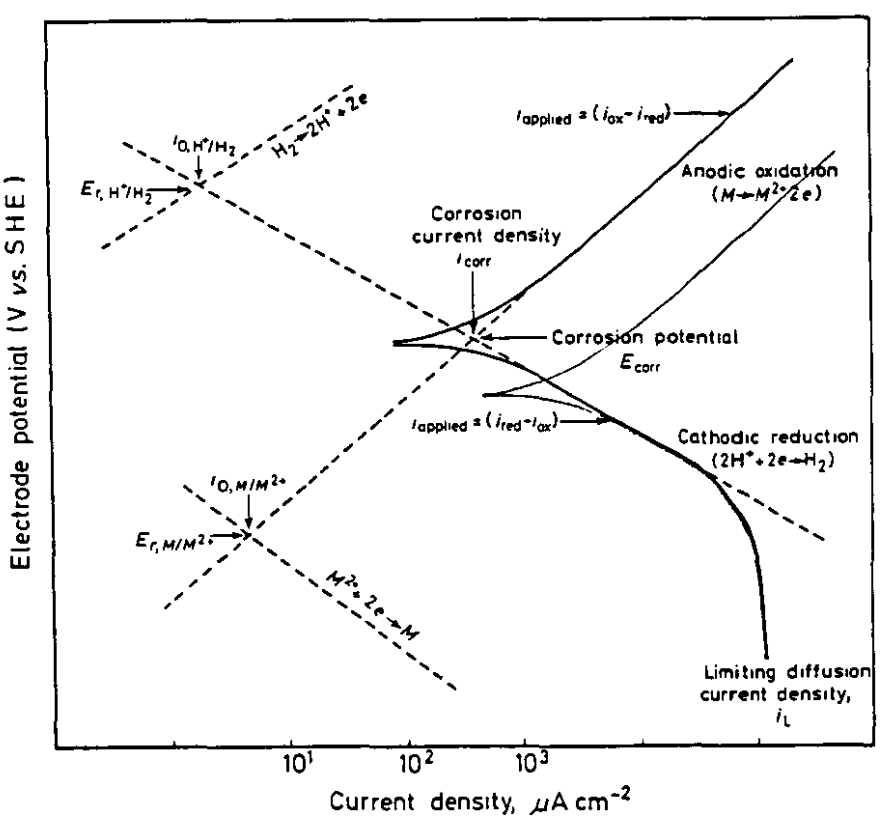

Figure 6.13 E *vs.* log$i$ curves for the corrosion of a metal in a reducing environment. (after Shreir[114])

There are two exchange processes involving oxidation of M & M^{2+} and reduction of H^+ & H_2. The reverse reactions for exchange processes however are negligible at potentials removed from E_r (the reversible potential) and will be neglected.

Under slurry erosion the oxygen transport to the metal surface is accelerated, which shifts anodic oxidation E *vs.* log$i$ curve towards the right, i.e. to increased current densities, indicated in red. The hydrogen evolution reaction remaining unaffected. The intersection of the E *vs.* log$i$ curves for the anodic and cathodic reaction is now at higher current densities and at a lower potential, (fig. 6.13). This mirrors the behaviour of the aluminium alloys and the corrosion resistant steels. The EN3B (mild steel) and the EN8 (medium carbon) steels do not form corrosion products that act as diffusion barriers to oxygen. Therefore in the case of the EN3B and the EN8 steels subjected to slurry erosion the oxidation reaction remains unchanged in the synthetic mine water.

CHAPTER 7

CONCLUSIONS AND RECOMMENDATIONS

Slurry erosion can cause extensive metal loss in aluminium alloys, aluminium metal matrix composites and steels.

Under the test conditions used the addition of reinforcement to the matrix alloys did not improve the erosion resistance of the matrix alloys. This was as a result of reduced work to fracture values and microfractures associated with the reinforcement fracture.

Both the Al5083 and the Al7017 aluminium alloys exhibited good hardness and work to fracture values, accompanied with low erosion rates. The addition of less than 15% by volume of reinforcement particulates to an Al5083 or Al7017 matrix warrants evaluation in terms of its expected improved slurry erosion resistance.

The effect of corrosion, on the aluminium alloys and the corrosion resistant steels, alone is insignificant, but the combined action of the slurry erosion and corrosion mechanisms result in a mutual or synergistic reinforcement of their effects.

The erosion component of the erosive-corrosive wear is the major mode of metal loss, under the conditions tested.

Improved slurry erosion-corrosion performance is not necessarily achieved by upgrading to more corrosion-resistant alloys or by using cathodic protection. Alloys that rely on the integrity of their oxide layers, for corrosion resistance, may be subject to the synergistic effects of erosion and corrosion, to much greater degree than far less corrosion resistant alloys.

The equipment can be useful to explore methods of corrosion control. These may include corrosion inhibitors and emulsifying oils. Cathodic protection should be considered for some systems.

REFERENCES

1 C. Subramanian, Some considerations towards the design of a wear resistant aluminium alloy, *WEAR, 155* (1982) 193-205.

2 A. Ball, S. Willmott and A. Resente, The erosion of candidate materials for valves in coal gasification systems, *Department of Materials Engineering, University of Cape Town*, South Africa (1985-) 753-761.

3 J.G.A. Bitter, *WEAR, 6* (1963) 169-190.

4 R. Brown and J. Edington, Mechanisms of Material Loss During the Threshold Period of Erosion by Solid Particles, *WEAR, 77* (1982) 347-353.

5 R.A. Doyle and A. Ball, On thermomechanical effects during solid particle erosion, *Department of Materials Engineering*, University of Cape Town, South Africa.

6 J. Fan, D. Zhou, J. Jin and K. Cen, Numerical Simulation of Tube Erosion by Particle Impaction, *WEAR, 142* (1991) 171-184.

7 J.E. Field and I.M. Hutchings, Impact Erosion Processes, *Paper presented at 3rd Conference of Mechanical Properties Under High Rates of Strain*, Oxford, (1984), Institute of Physics.

8 I. Finnie, Erosion of Surfaces by Solid Particles, *WEAR, 3*, (1960) 87-103.

9 J.E. Goodwin, W. Sage and G.P. Tilly, Study of Erosion by Solid Particles, *Proceedings of the Institution of Mechanical Engineers, 184*, (1969-1970) 279-292.

10 M.E. Gulden, Influence of Brittle to Ductile Transition on Solid Particle Erosion Behaviour, *Proc. 5th Int. Conf. Erosion by Sloid and Liquid Impact*, Cambridge, Cavendish Lab., (1979), 31-1 - 31-9.

11 Å. Hammarsten, S. Söderberg and S. Hogmark, Study of Erosion Mechanisms By Recovery and Analysis of Wear Fragments, *Uppsala University, Institute of Technology*, Uppsala, Sweden, (1981-) 373-381.

12 I.M. Hutchings, Mechanical and Metallurgical Aspects of the Erosion of Metals, *NACE Conference on Erosion-Corrosion in Coal Conversion Systems*, Berkeley, Jan. 1979.

13 I.M. Hutchings, Strain Rate Effects in Microparticle Impact, *Journal of Physics D: Applied Physics, 10*, (1977) L179-L184.

14 I.M. Hutchings, In W.F. Adler (ed.), *Erosion: Prevention and Useful Application*, ASTM Special Technical Publication 664, 1979, (ASTM Philadelphia, PA).

15 I.M. Hutchings and R.E. Winter, *WEAR, 27* (1974) 121.

16 R.E. Winter and I.M. Hutchings, *WEAR, 29* (1974) 181.

17 L.K. Ives and A.W. Ruff, Transmission and Scanning Electron Microscopy Studies of Deformation at Erosion Impact Sites, *WEAR, 46,* (1978) 149-162.

18 G. Carter, M.J. Nobes and K.I. Arshak, The Mechanism of Ripple Generation on Sandblasted Ductile Solids, *WEAR, 65* (1980), 151-174.

19 J.A. Laitone, Aerodynamic Effects in the Erosion Process, *WEAR, 56* (1979), 239-246.

20 B. Lamy, Effect of Brittleness Index and Sliding Speed on the Morphology of Surface Scratching in Abrasive Erosive Processes, *TRIBOLOGY International, 17* (1984), 35-38.

21 A.V. Levy, The Erosion Properties of Alloys for the Chemical Processing Industries, *WEAR, 151,* (1991) 337-350.

22 A.V. Levy and P. Crook, The erosion properties of alloys for the chemical processing industries, *WEAR, 151,* (1991) 337-350.

23 S. Malkin, Correlation Between Solid Particle Erosion of Metals and their Melting Energies, *WEAR, 68* (1981) 391-396.

24 M. Naim and S. Bahadur, Workhardening in erosion due to single particle impacts, *Mechanical Engineering Department, Iowa State University,* Iowa, USA, (1983?) 340-345.

25 R.C. Pennefather, S.E. Hankley, R.Hutchings and A. Ball, *Materials Science and Engineering, A105/106* (1988) 389-394.

26 C.M. Preece and N.H. Macmillan, *Annual Review of Materials Science, 7* (1977) 95-121.

27 E. Raask, Particle Impaction Erosion in Coal-fired Boiler Plants, *VGB KRAFTWERKSTECHNIK, 59,* (1979) 458-464.

28 A.W. Ruff, Analysis of Interlaboratory Test Results of Solid Particle Impingement Erosion, *WEAR, 108,* (1986) 323-335.

29 A.W. Ruff and S.M. Wiederhorn, Erosion by solid particle impact, *Treatise on Materials and Technology, 16,* Academic Press, (1979) 69-126.

30 G.L. Sheldon, Similarities and Differences in the Erosion Behaviour of Materials, *Journal of Basic Engineering,* Transactions of the ASME, September (1970) 619-626.

31 G.L. Sheldon and A. Kanhere, An Investigation of Impingement Erosion Using Single Particles, *WEAR, 21,* (1972) 195-209.

32 S. Söderberg, S. Hogmark, U. Engman and H. Swahn, Erosion classification of materials using a centrifugal erosion tester, *TRIBOLOGY international,* (1981) 333-343.

33 S. Söderberg, S. Hogmark and H. Swahn, Mechanisms of Material Removal During Erosion of a Stainless Steel, Presented at the 37th *American Society of Lubrication Engineers* Annual Meeting in Cincinnati, Ohio, May 10-13, (1982) 1-11.

34 N.P. Suh, Relationship of solid particle erosion to other types of wear, *M.I.T.,* Cambridge.

35 G.P. Tilly, Erosion Caused by Impact of Solid Particles, in *Treatise on Materials Science and Technology, 13,* D. Scott, ed., Academic Press, New York (1979) 287-319.

36 H. Uuemóis and I. Kleis, A Critical Analysis of Erosion Problems which have been Little Studied, *WEAR, 31* (1975) 359-371.

37 V.N. Vinogradov and I.B. Cherviakov, Physical/Mathematical Model of Interaction Between Hard Spherical Particle and Metal Surface at High Rates of Strain, *Inst. Phys. Conf. Ser. No.70, presented at 3rd Conf. Mech. Prop. High Rates of Strain, Oxford,* (1984) 405-412.

38 K.-H. Zum Gahr, Microstructure and Wear of Materials, *Tribology Series, 10* (1987) Elsevier Science Publishers.

39 G. Sundararajan, A comprehensive model for the solid particle erosion of ductile materials, *WEAR, 149* (1991) 111-127.

40 J.A.C. Humphrey, A Transition State Model for Predicting the Rate of Erosive Wear of Ductile Materials by Solid Particles, *WEAR, 65* (1980) 207-214.

41 I. Finnie, G.R. Stevick and J.R. Ridgely, The influence of impingement angle on the erosion of ductile metals by angular abrasive particles, *WEAR, 152* (1992) 91-98.

42 I. Finnie and D.H. McFadden, On the Velocity Dependence of the erosion of Ductile Metals by Solid Particles at Low Angles of Incidence, *WEAR, 48* (1978) 181-190.

43 I. Finnie, Some observations on the erosion of ductile metals, *WEAR, 19* (1972) 81-90.

44 W.A. Brainard and J. Salik, An Investigation into the Role of Adhesion in the Erosion of Ductile Metals, *ASLE TRANSACTIONS, 24* (1980) 302-306, presented at the 35th Annual Meeting in Anaheim, California, May 5-8 1980.

45 R. Bellman,Jr. and A. Levy, Erosion mechanisms in ductile metals, *WEAR, 70* (1981) 1-27.

46 T. Quadir and P. Shewmon, Solid Particle Erosion Mechanisms in Copper and Two Copper Alloys, *Metallurgical Transactions A, 12A,* (1981) 1163-1176.

47 J. Salik, D. Buckley and W.A. Brainard, The Effect of Mechanical Surface and Heat Treatments on the Erosion Resistance of 6061 Aluminium Alloy, *WEAR, 65,* (1981) 351-358.

48 S. Dosanjh and J.A.C. Humphrey, The Influence of Turbulence on Erosion by a Particulate-Laden Fluid Jet, *WEAR, 102* (1985) 309-330.

49 C. Forse and A. Ball, Solid Particle Erosion in Hydraulic Machinery, *Proc. 6th Int. Conf. on Erosion by Liquid and Solid Impact,* (1983-) 61-1 - 61-7.

50 D.H. Graham and A. Ball, Particle erosion of candidate materials for hydraulic valves, *WEAR, 133* (1989) 125-132.

51 S.H.D. Joffe and C. Allen, The Wear of Pump Valves in Fine Particulate Quartzite Slurries, *WEAR, 135* (1990) 279-291.

52 A. Karimi and R.K. Schmid, Ripple formation in solid-liquid erosion, *WEAR, 156* (1992) 33-47.

53 S. Ka-Keung Li, J.A.C. Humphrey and A.V. Levy, Erosive Wear of Ductile Metals by a Particulate-Laden High Velocity Liquid Jet, *WEAR, 73* (1981) 295-309.

54 A.V. Levy and P. Yau, Erosion of Steels in Liquid Slurries, *WEAR, 98,* (1984) 163-182.

55 A.V. Levy, J. Yan and Arora, V.D., Sand-Water Slurry Erosion of Carburised AISI 8620 Steel, *WEAR, 101,* (1985) 117-126.

56 F.Y. Lin and H.S. Shao, Effect of Impact Velocity on Slurry Erosion and a New Design of a Slurry Erosion Tester, *WEAR, 143,* (1991) 231-240.

57 H.Q. Lou and A. Krizman, Erosion of Materials by Alumina Slurry - Part 1, *WEAR, 134* (1989), 253-269.

58 H.Q. Lou and A. Krizman, Erosion of Materials by Alumina Slurry - Part 2, *WEAR, 134* (1989), 271-281.

59 R.S. Lynn, K.K. Wong and H.McI. Clark, On the particle size effect of slurry erosion, *WEAR, 149* (1991), 55-71.

60 F. Pourahmadi and J.A.C. Humphrey, Modeling Solid-Fluid Turbulent Flows with Application to Predicting Erosive Wear, *Physico Chemical Hydrodynamics, 4* (1983) 191-219.

61 W. Qiongli, X. Peien, S. Shiumei and X. Cuizhen, On the mechanism of wet abrasive erosion, *TRIBOLOGY International, 18,* (1985) 113-119.

62 A.S. Rao and D. Kung, Sand Erosion and Cavitation Behaviour of Hydraulic Turbine Runner Materials, *Proc. Conf. Surface Engineering,* Toronto, Canada, 25-27 June (1990) 615-624, Elsevier Appl. Sci., New York.

63 M.C. Roco, Wear Mechanisms in Centrifugal Slurry Pumps, *Corrosion-NACE, 46* (1990) 424-431.

64 S. Turenne, M. Fiset and J. Masounave, The Effect of Sand Concentration on the Erosion of Materials by a Slurry Jet, *WEAR, 133,* (1989) 95-106.

65 J.B. Zu, G. T. Burstein and I.M. Hutchings, A Comparative Study of the Slurry Erosion and Free-Fall Particle Erosion of Aluminium, *WEAR, 149* (1991) 73-84.

66 J.B. Zu, Bridging slurry erosion and airborne solid particle erosion, Department of Materials Science and Metallurgy, University of Cambridge.

67 R. Badruddin and S. Bahadur, Erodent Particle Characterisation and the Effect of Particle Size and Sharpness on Erosion, 1-17, Department of Mechanical Engineering, Iowa State University, Ames, IA 50011, USA.

68 J.C. Charenton, P. Rombeaux, B. Hurtaud and J.M. Hauser, Stainless steel, with 11 per cent Chromium and High Yield Strength, for Welded Constructions Resistant to Corrosion and Abrasion, *INFACON 6. Proceedings of the 1st International Chromium Steel and Alloys Congress, Cape Town,* Vol.2. Johannesburg, South African Institute of Mining and Metallurgy, 1992 229-234.

69 T. Christman, and P.G. Shewmon, The effect of abrasive particle size on the slurry erosion resistance of particulate-reinforced aluminium alloy, *WEAR, 54* (1979) 145-155.

70 S.K. Hovis, J.E. Talia and R.O. Scattergood, Erosion mechanisms in aluminium and Al-Si alloys, *WEAR, 107* (1986) 175-181.

71 V.F. Kocks, Laws for Work-Hardening and Low-Temperature Creep, *Journal of Engineering and Materials Technology, 98* (1976) 76-85.

72 M. Liebhard and A. Levy, The effect of erodent particle characteristics on the erosion of metals, *WEAR, 151,* (1991) 381-390.

73 C.T. Morrison, R.O. Scattergood and J.L. Routbort, Erosion of 304 Stainless Steel, *WEAR, 111,* (1986) 1-13.

74 P.G. Shewmon, Particle size threshold in the erosion of metals, *WEAR, 68,* (1981) 253-258.

75 P.H. Shipway and I.M. Hutchings, The influence of particle properties on the erosive wear of sintered boron carbide, *WEAR, 149,* (1991) 85-98.

76 G. Sundararajan, The depth of plastic deformation beneath eroded surfaces: the influence of impact angle and velocity, particle shape and material properties, *WEAR, 149* (1991) 129-153.

77 R. Angers, B. Champagne, M. Fiset and P. Chollet, A new wear resistant composite, *R&HM,* June (1984) 79-85.

78 Y.A. Ballout, S.K. Hovis and J.E. Talia, Erosion in Glass-Fibre Reinforced Epoxy Composites, *Scripta METALLURGICA et MATERIALIA, 24* (1990) 195-200.

79 S. Srinivasan, R. O. Scattergood and R. Warren, Erosion of Fibre Reinforced Al-4 Pct Cu Composites, *Metallurgical Transactions A, 19A* (1988) 1785-1793.

80 A.J. Ninham and A.V. Levy, The Erosion of Carbide-Metal Composites, *WEAR, 121* (1988) 347-361.

81 K.C. Goretta, W. Wu, J.L. Routbort and P. K. Rohatgi, Solid-Particle Erosion of Aluminium/Particulate Ceramic Composites, in P. K. Rohatgi, C. S. Yust and P. J. Blau (eds.), *Proc. Conf. Tribology of Composite Materials,* Oak Ridge TN., May 1-3, 1990, ASM Int., (1990) 147-155.

82 W. Wu, K.C. Goretta and J.L. Routboart, Erosion of 2014 Al reinforced with SiC or Al_2O_3 particles, *Materials Science and Engineering,* A151 (1992) 85-95.

83 T.H. Kosel, R.O. Scattergood and A.P.L. Turner, in K.C. Ludema, W.A Glaeser and S.K. Rhee (eds.), *Wear of Materials 1979,* American Society of Mechanical Engineering, New York, 1979.

84 J.E. Hatch, Aluminium - Properties and physical metallurgy, Aluminium Association, *American Society for Metals,* Metals Park, Ohio, (1984).

85 J.H. Swisher, Alloy Corrosion and Erosion in Coal Preparation Plants, *Corrosion-NACE, 47,* (1991) 397-404.

86 B.Q. Wang, G.Q. Geng and A. Levy, Effect of microstructure on the erosion-corrosion of steels, *WEAR, 151* (1991) 351-364.

87 S.X. Xie and J.P. Hirth, Permeation of hydrogen, trapping, and damage in spheroidized AISI 1090 steel, *Corrosion-NACE, 38* (1982) 486-493.

88 T. Zakroczymski, Z. Szklarska-Smialowska and M. Smialowski, Adsorption of hydrogen by austenitic steels, *Corrosion-NACE, 39* (1983) 207-212.

89 M.S.N. Bhat, M.K. Surappa and H.V. Sudhaker Nayak, Corrosion Behaviour of silicon carbide particle reinforced 6061/Al alloy composites, *Journal of Materials Science, 26* (1991) 4991-4996.

90 S. Lin, H. Greene, H. Shih and F. Mansfeld, Corrosion Protection of Al/SiC Metal Matrix Composites by Anodising, *Corrosion-NACE, 48* (1992) 61-67.

91 J.F. McIntyre, R.K. Conrad and S.L. Golledge, The Effect of Heat Treatment on the Pitting Behaviour of SiC_w/AA2124, *Corrosion-NACE, 46* (1990) 902.

92 D. Nath and T.K.G. Namboodhiri, Corrosion of an aluminium alloy-mica particulate composite in 3.5% NaCl, *Composites, 19* (1988) 237-243.

93 R.C. Paciej and V.S. Agarwala, Metallurgical Variables Influencing The Corrosion Susceptibility of a Powder Metallurgy SiCw/Al Composite, *Corrosion-NACE, 42* (1986) 718-729.

94 H. Sun, E.Y. Koo and H.G. Wheat, Corrosion Behaviour of SiCp/6061 Al Metal Matrix Composites, *Corrosion-NACE, 47* (1991) 741-753.

95 C.R. Schmitt, Corrosion Behaviour of Aluminium in Water, *Reviews on Coatings and Corrosion, 4* (1979) 95-112.

96 J.E. Draley and W.E. Ruther, Aqueous Corrosion of Aluminium, Part 1 - Behaviour of 1100 Alloy , *Corrosion, 12* (1956) 441-448.

97 A.A. Adams, *et al.*, Synergistic Effects of Anions in the Corrosion of Aluminium Alloys, *Journal of Electrochemical Society, 119* (1972) No.12.

98 W.W. Binger and C.M. Marstiller, Aluminium Alloys for Handling High-Purity Water, *Corrosion, 13* (1957) No.9.

99 P.P. Trzaskoma, *Corrosion-NACE, 42*, (1986) 609-613.

100 E.H. Dix, Corrosion of Light Metals, *American Society for Metals*, (1946) 131-176.

101 S.K. Hovis, J.E. Talia and R.O. Scattergood, Erosion in multiphase systems, *WEAR, 108* (1986) 139-155.

102 I.M. Hutchings and A. Wang, Wear of Aluminium-alumina metal-matrix composites by abrasion and erosion, *Proc. Conf. New Materials and their Applications*, Warwick, April(1990), to be published in *Institute of Physics Conference Series*.

103 S.V. Prasad and B.D. McConnell, Tribology of Aluminum Metal-Matrix Composites: lubrication by graphite, *WEAR, 149* (1991) 241-253.

104 S. Turenne and M. Fiset, Evaluation of Abrasive Particle Trajectories in a Slurry Jet during Erosion of Metal Matrix Composites, *Wear Testing of Advanced Materials Symposium, San Antonio, Texas*, Nov. 14, 1990.

105 S. Turenne, C. LeDéoré and J. Masounave, Slurry erosion of Al_2O_3-SiO_2/Al-4Mg metal matrix composites, *Industrial Materials Research Institute, National Research Council Canada*, (1987-) 39-45.

106 S. Turenne, D. Simard and M. Fiset, Influence of structural parameters on the slurry erosion resistance of squeeze-cast metal matrix composites, *WEAR, 149* (1991) 187-197.

107 S. Wilson and A. Ball, Performance of metal matrix composites under various triblological conditions, Advances in Composite Tribology in K. Friedrich (ed.), *Composite Materials Series* (B. Pipes ed.), Elsevier Sci. Publ. (in press), 1992/1993.

108 S. Wilson and A. Ball, The Abrasive Wear of an Aluminium Metal Matrix Composite, *Electron Microscopy Society of Southern Africa Proceedings, 19* (1989) 171-172.

109 G.D Meyer-Rodenbeck, T. Hurd, and A. Ball, On the abrasive-corrosion wear of aluminium alloys, *WEAR, 154* (1992) 305-318.

110 R.E. Nöel and A. Ball, On the synergistic effects of abrasion and corrosion during wear, *WEAR, 87* (1983) 351-361.

111 K. Sotoudeh, T.H. Nguyen, R.T. Foley and B.F. Brown, The Chemical Nature of Aluminium Corrosion: I Corrosion of Aluminium Surfaces by Aluminium Salts, *Corrosion-NACE, 37* (1981) 358-362.

112 R.C. Selly, *An introduction to sedimentology*, Academic Press, (1982) 230.

113 B.C. Syrett and S.S. Wing, Effect of Flow on Corrosion of Copper Nickel Alloys in Aerated Sea Water and in Sulphide-Polluted Sea Water, *Corrosion-NACE, 36* (1980) 73-84.

114 L.L. Shreir, Corrosion, Vol. 1 and 2, second edition 1979, Newnes-Butterworths.

115 R.W.K. Honeycombe, Steels - Microstructure and Properties, *Metallurgy and Materials Science Series*, Edward Arnold (Publishers) Ltd, 1981.

116 M.B. Abuzriba, R.A. Dodd, F.J. Worzala and J.R. Conrad, Wear Corrosion: Separation of the Components of Corrosion and Wear, *Corrosion-NACE, 48* (1992) 2-4.

117 K.C. Barker and A. Ball, Synergistic abrasive-corrosive wear of chromium containing steels, *British Corrosion Journal, 24* (1989) 222-228.

118 A. Ball and H. Böhm, The design and performance of steels in an abrasive-corrosive mining environment, C189/87 *Journal of the Institute of Mechanical Engineering*, (1987) 595-602.

119 S. Bhattacharyya, V.S. Agarwala and K.Y.Kim, Wear-Corrosion of Steels Under Cyclic Operation in Corrosive Liquid Environment, *Wear of Materials* (1985) 162-172.

120 G.N. Blount, R.T. Moule and W.J. Tomlinson, Environmental Aspects of Cavitation Erosion in Simulated Industrial Waters, *Corrosion-NACE, 46* (1990) 340-347.

121 R.J. Brigham, Elechtrochemical Study of the Mechanisms of Corrosive Wear, *Canadian Metallurgical Quarterly, 15* (1976) 389-393.

122 A.J. Bursle, Effective Abrasion and Corrosion Control Using Corrosion Resistant Alloys, *Report by Comsteel Stainless Flat Products, Unanderra.*

123 G.T. Burstein, G.W. Ashley, P.I. Marshall and R.D.K. Misra, Corrosion of Metals Under Conditions of Erosive Wear, *Proceedings of the 6th International Conference on Erosion by Liquid and Solid Impact*, (1983), 49-1 - 49-8.

124 G.T. Burstein, G.W. Ashley and P.I. Marshall, Reactivity of Metals in Aqueous Solutions Under Conditions of Abrasion, *Industrial Water Treatment and Conditioning*, 36th International Conference CEBEDEAU-LIEGE, May 25-27, 1983.

125 G.T. Burstein and R. J. Cinderey, The Potential Of Freshly Generated Metal Surfaces Determined From The Guillotined Electrode-A New Technique, *Corrosion-NACE, 32* (1991) 1195-1211.

126 R.J. Cinderey and G.T. Burstein, The Repassivation of Aluminium in Water, *Corrosion Science, 33* (1992) 449-502.

127 A. Coulon and G. Thauvin, Erosion and Erosion Corrosion of Metals, *Proc. 5th Int. Conf. on Erosion by Solid and Liquid Impact,* 25-1 - 25-11.

128 D.J. Dunn, Metal removal mechanisms comprising wear in mineral processing, *Proceedings of the International Conference on Wear of Materials,* Vancouver, Canada, ASME, (1985) 501-508.

129 R. El-Kousy, S.M. El-Raghy and A.E. El-Mehairy, *Tribology International, 14* (1981) 216.

130 S.M. El-Raghy, H. Abd-El-Kader and M.E. Abou-El-Hassan, Electrochemistry of Abrasion Corrosion of Low Alloy Steel in 1% NaCl Solution, *Corrosion-NACE, 40* (1984) 60-61.

131 G. Geng, B. Wang, P.Y. Hou and A.V. Levy, The effect of additional silicon on the corrosion and erosion-corrosion of low chromium steels, *WEAR, 150* (1991) 89-105.

132 G.A. Gehring,Jr. and M.H. Peterson, Corrosion of 5456-H117 Aluminium in High Velocity Sea Water, *Corrosion-NACE, 37,* (1981) 232-242.

133 Ph. Gimenez, J.J. Rameau and M.C. Reboul, Experimental pH Potential Diagram of Aluminium for Sea Water, *Corrosion-NACE, 37* (1981) 673-682.

134 E. Heitz, Chemo-Mechanical Effects of Flow on Corrosion, *Corrosion-NACE, 47* (1991) 135-145.

135 A. Iwabuchi, T. Tsukamoto, Y. Tatsuyanagi, N. Kawahara and T. Nonaka, Electrochemical Approach to Corrosive Wear of SKD61 die Steel in Na_2SO_4 Solution, *WEAR, 156* (1992) 301-313.

136 D.A. Jones, Corrosive Wear in Ore Grinding Systems, *Journal of Metals,* (1985) 20-23.

137 D.A. Jones, Effect of Water Chemistry on the Erosion-Corrosion of Aluminium in High Temperature High Velocity Water, *Corrosion-NACE, 37* (1981) 563-569.

138 G.E. Lazarev, T.E. Charlamova and V.J. Vevejkin, Speciality of friction and wear of materials in aggressive media, *Trenie Iznoz, 2* (1981) 43-52.

139 A.V. Levy, The abrasion/erosion and erosion-corrosion characteristics of steels, *WEAR, 138,* (1990) 111-123.

140 H. Lin and Z.Quingde, The Behavior of 28% Chromium White Cast Iron in Abrasion and Corrosion-Abrasion Wear, *Mechanical Engineering Department,* Xian Jiaotong University, Xian, China, (1982-) 653-659.

141 D. Lloyd, Erosion - Corrosion Control in an Iron Ore Benefication Plant, *paper presented at the UK Corrosion '83 Conference,* (1983) 10-12.

142 B.W. Madsen, Measurement of erosion-corrosion synergism with a slurry wear test apparatus, *WEAR, 123* (1988) 127-142.

143 H. Nanjo, Y. Kurata, O. Asano, N. Sanada and J. Ikeuchi, The Effects of Velocity and Pressure Vibration on Erosion-Corrosion of Mild Steel in Water, *Corrosion-NACE, 46* (1990) 837-842.

144 S. Nesic, and J. Postlethwaite, Relationship Between the Structure of Disturbed Flow and Erosion-Corrosion, *Corrosion-NACE, 46* (1990) 874-880.

145 A.J. Ninham, I.M. Hutchings and J.A. Little, Erosion/Oxidation of Austenitic and Ferritic Alloys, *Corrosion-NACE, 46* (1990) 296-301.

146 Y. Oka, M. Matsumara and M. Yamawaki, Slurry erosion-corrosion on commertially pure iron in a vibratory testing facility - mechanism of erosion-corrosion under

predominanatly erosion conditions, *Proceedings of the 7th International Conference on Erosion by Liquid Solid Impact,* University of Cambridge, 1987, Paper 39.

147 J.A. Peters, G. Wright, J.V. Bee and G.G. Garrett, Alloy Design For Abrasion-Corrosion Resistance in Mineral Transportation Systems, *Proceedings of the International Conference on Fracture Prevention in Energy and Transport Systems, Rio de Janeiro,* December 1983 81-90.

148 J. Postlethwaite, Effect of Chromate Inhibitor on the Mechanical and Electrochemical Components of Erosion-Corrosion in Aqueous Slurries of Sand, *Corrosion-NACE, 37* (1981) 1-5.

149 J. Postlethwaite, B.J. Brady, M.W. Hawrylak and E.B. Tinker, Effect of Corrosion on the Wear Patterns in Horizontal Slurry Pipelines, *Corrosion-NACE, 34* (1978) 245-250.

150 J. Postlethwaite, M.H. Dobbin and K. Bergevin, The Role of Oxygen Mass Transfer in the Erosion-Corrosion of Slurry Pipelines, *Corrosion-NACE, 42* (1986) 514-521.

151 J. Postlethwaite and M.W. Hawrylak, Effect of Slurry Abrasion on the Anodic Dissoltion of Iron in Water, *Corrosion-NACE, 31* (1975) 237-240.

152 B. Poulsen, Electrochemical Measurements in Flowing Solutions, *Corrosion Science, 23* (1983) 391-430.

153 H.M. Shalaby, S. Attari, W.T. Riad and V.K. Gouda, Erosion-Corrosion Behavior of Some Cast Alloys in Seawater, *Corrosion-NACE, 48* (1992) 206-217.

154 W.J. Tomlinson and M.G. Talks, Erosion and corrosion of cast iron under cavitation conditions, *Tribology International, 24* (1991) 67-75.

155 E. Wandke, M. Möser and S. Tscherny, The influence of corrosion and hydrogen cracking on blast wear in wet media, *WEAR, 121* (1988) 15-26.

156 R.J.K. Wood and S.P. Hutton, The synergistic effect of erosion and corrosion: trends in published results, *WEAR, 140* (1990) 387-394.

157 R.W.K. Honeycombe, Steels - Microstructure and Properties, *Metallurgy and Materials Science Series,* Edward Arnold (Publishers) Ltd, 1981.

158 D.G. Rickerby, Correlation of erosion with mechanical properties in metals, *WEAR, 84* (1983) 393-395.

159 I. Finnie, Wolak J. and Y. Kabil, Erosion of Metals by Solid Particles, *Journal of Materials, 2* (1967) 682-700.

160 A.K., Vijh, Resistance of metals to erosion by solid particles in relation to the solid state cohesion of metals, *WEAR, 39* (1976) 173-175.

161 C.E., Smeltzer, M.E. Gulden and W.A. Compton, Mechanisms of metal removal by impacting dust particles, *Journal of Basic Engineering, 92* (1970) 639-654.

162 L.P. McCabe, G.A. Sargent and H. Conrad, Effect of Microstructure on the erosion of steel by solid particles, *WEAR, 105* (1985) 257-277.

163 L. Brass, Effects of Microstructure of Ductile Alloys on Solid Particle Erosion, In LBL - 7355, *Annual Report of Materials and Molecular Research Division,* Lawrence Berkeley Laboratory, (1977).

164 G.L. Sheldon, Effects of Surface Hardness and Other Material Properties on Erosive Wear of Metals by Solid Particles, *Journal of Engineering Materials and Technology,* Transactions of the ASME, April (1977) 133-137.

165 A. Ball, On the importance of work hardening in the design of wear resistant materials, *WEAR, 91* (1983) 201-207.

166 A. Ball, The mechanisms of wear, and the performance of engineering materials, *Journal of the South African Institute of Mining and Metallurgy, 86* (1986) 1-13.

167 G.E., Dieter, *Mechanical Mettalurgy,* McGraw-Hill, New York, 2nd edn., 1976, p. 336.

168 *Metals Handbook,* Vol.1, American Society for Metals, Metals Park, OH, 8th. edn., 1961.

169 L., Northcott, *Molybdenum,* Butterworths, London, 1956, p. 59.

170 G.L., Miller, *Tantalum and Niobium,* Butterworths, London, 1956, p. 398.

171 S.H. Avner, Introduction To Physical Metallurgy, 2nd Edition, *McGraw-Hill Kogakusha, Ltd,* (1974).

172 Erosion and Wear; Metal Corrosion, *Annual Book of ASTM Standards,* 03.02 (1985) 134-138, 242-249.

APPENDIX

C	*Si*	*Mn*	*S*	*P*	*Cr*	*Cu*	*Mo*
0.85	0.4	0.75	0.02	0.03	1.04	0.17	0.28

Table A.1 Composition of low alloy steel specimens used by El-Raghy, Abd-El-Kader and Abou-El-Hassan[130].

Mg	*Mn*	*Cr*	*Cu*
4.7-5.5	0.50-1.0	0.05-0.20	0.10max

Zn	*Ti*	*Si + Fe*	*Other*
0.25max	0.20max	0.40max	0.15max

Table A.2 Composition of aluminium alloy specimens used by Gehring and Peterson[132].

Metal	*Yield* σy	*UTS* σu	*Elongation*
	(MPa)	(MPa)	(%)
Al alloy 1100	35	90	45
Ag	55	125	48
Cu	69	220	45
Fe	126	283	47
Mg	103	193	15
Mo	345	549	55
Pb	9	17	52
Sn	9	15	45
Ta	271	343	45

Table A.3 Mechanical properties of annealed materials used by Rickerby[158].

Grading Limits		
Max 2% > 850 μm Max 4% < 425 μm		
Typical Grading Analysis		
Aperture size (μm)	*U.S. Mesh*	*% Retained*
1000	18	0.1
850	20	0.2
710	25	0.7
600	30	23.5
500	35	67.4
425	40	6.6
355	45	1.2
300	50	0.3
250	60	0

Table A.4 Grading limits and grading analysis for the silica sand erodent, type 20/40 density sand from Consul Industrial Minerals.

Density	2564 kg/m^3
Loose bulk density	1594 kg/m^3
Effective size	0.50 mm
Coefficient of uniformity	1.15
A.F.S. number	28
Typical chemical analysis	*wt%*
SiO_2	99.74
Al_2O_3	0.09
Fe_2O_3	0.018
TiO_2	0.032
ZrO_2	0.005
CaO	0.003
MgO	traces

Table A.5 Further typical erodent data and chemical analysis.

pH	*5.7*
sulphates chlorides	715ppm 350ppm

Table A.6 Corrosive synthetic mine water solution based on an analysis of mine water[110].

Alloy	*Alloying elements (%wt)*								
	Cu	Fe	Mg	Mn	Si	Ti	Zn	Cr	Other
1070	0.03	0.25	0.03	0.03	0.2	0.03	0.07	-	0.03
1200	0.05	0.7	-	0.05	0.5	0.05	0.1	-	0.15
2014	3.9-5.0	0.7	0.20-0.8	0.4-1.2	0.5-1.2	0.15	0.25	0.10	0.15
3004	0.25	0.7	0.8-1.3	1.0-1.5	0.3	0.05	0.25	0.1	0.01
5083	0.10	0.40	4.0-4.9	0.40-1.0	0.40	0.15	0.25	0.25	0.15
6061	0.15-0.4	-	0.8-1.2	-	0.40-0.8	-	-	0.35	
6261	0.15-0.4	0.40	0.7-1.0	0.20-0.35	0.40-0.70	0.10	0.20	0.10	0.15
7017	0.20	0.45	2.0-3.0	0.05-0.50	0.35	0.15	4.0-5.2	0.35	0.15
7075	1.2-2.0	0.50	2.1-2.9	0.30	0.40	0.20	5.1-6.1	0.28	0.15

Table A.7 Compositions, of the aluminium alloys used in the investigation.

C	*Mn*	*Si*	*Cr*	*Ni*	*P*	*S*	*N*
0.08max	2.0max	1.0max	18.0-20.0	8.0-10.5	0.045max	0.030max	0.10max

Table A.8 Composition, %wt(max), of the 304 (ASTM A240) stainless steel specimens. The specimens were solution treated at 1000°C for half an hour and then quenched in oil.

C	*Cr*	*Ni*
0.19	16.0	1.7

Table A.9 Composition, %wt(max), of the 431 (ASTM A240) stainless steel specimens.

C	*Mn*	*Si*	*Cr*	*Ni*	*P*	*S*	*Ti*
0.03max ax	1.5max	1.0max	11.0-12.0	1.5max	0.030max	0.030max	0.6m

Table A.10 Composition, %wt(max), of the 3CR12 (SX specification) "corrosion resistant" steel specimens. The specimens tested in the as received, annealed condition.

Element	Min.	Max.
Carbon	0.16	0.24
Silicon	0.10	0.40
Manganese	0.50	0.90
Sulpher	-	0.05
Phosphorous	-	0.05

Table A.11 Composition, %wt(max), of the EN3B (070M20) "20" carbon steel specimens.

Element	Min.	Max.
Carbon	0.36	0.44
Silicon	0.10	0.40
Manganese	0.60	1.00
Sulpher	-	0.05
Phosphorous	-	0.05

Table A.12 Composition, %wt(max), of the EN8 (080M40) "40" carbon axle steel specimens (AISI 1043).

Aluminium Alloy	*Density* (g/cm^3)	*Yield Strength* (MPa)	*Best No.* $\times 10^{-3}$
1070	2.71	35	9.4
1200	2.71	70	4.7
2014	2.82	460	0.7
2014 15vol. $\%Al_2O_3$	3.03	430	0.9
2014 20vol. $\%Al_2O_3$	3.06	420	0.9
3004	2.72	145	2.3
5083	2.66	175	1.8
6061	2.71	330	1.0
6061 15vol. $\%Al_2O_3$	2.92	350	1.0
6061 20vol. $\%Al_2O_3$	2.99	300	1.2
6261	2.71	290	1.1
7017	2.76	531	0.63
7075	2.85	540	0.6
Average Best No. for the aluminium alloys			2.0

Table A.13 Best Nos for the aluminium alloys.

Steel	*Density* (g/cm^3)	*Yield Strength* (MPa)	*Best No.* $\times 10^{-3}$
3CR12	7.61	280	3.3
431SS	7.70	695	1.3
304SS	7.90	205	4.7
EN3B	7.82	215	4.4
EN8 Spheroidised	7.76	245	3.8
EN8 Tempered	7.76	385	2.4
EN8 Quenched	7.76	465	2.0
Average Best No. for the steels			3.1

Table A.14 Best Nos for the steels.

ALLOY	Density (g/cm^3)	Hardness (HV20)	Charpy Impact energy (J)	Work to fracture (MJ/m^3)	Erosion rate (mg/hour)			
					Distilled water		Synthetic mine water	
					90°angle	60°angle	90°angle	60°angle
1070	2.71	17	21	-	39.60	-	54.67	-
1200	2.71	31	50	19.71	26.24	-	37.19	-
2014	2.82	151	7	49.90	25.62	31.38	33.41	38.27
2014 15%Al_2O_3	3.03	174	1	5.42	29.52	37.50	35.95	41.17
2014 20%Al_2O_3	3.06	197	1	2.23	33.11	38.78	36.68	46.25
3004	2.72	52	36	34.20	23.28	-	29.95	-
5083	2.66	104	14	37.77	21.76	-	25.30	-
6061	2.71	117	20	33.92	29.91	36.96	30.37	44.72
6061 15%Al_2O_3	2.92	131	2	24.15	30.96	36.36	36.00	47.56
6061 20%Al_2O_3	2.99	137	2	8.25	33.54	40.80	39.17	49.48
6261	2.71	122	22	33.28	24.91	-	27.47	-
7017	2.76	141	10	74.02	22.90	-	29.97	-
7075	2.85	173	4	-	25.80	-	33.85	-

Table A.15 Results of the experimental work performed on the aluminium alloys.

ALLOY	Erosion rate x10^{-6}(mm /g)			
	Distilled water		Synthetic mine water	
	90°angle	60°angle	90°angle	60°angle
1070	213	-	295	-
1200	141	-	200	-
2014	133	162	173	198
2014 15%Al_2O_3	142	181	173	198
2014 20%Al_2O_3	158	185	175	221
3004	125	-	161	-
5083	119	-	139	-
6061	161	199	164	241
6061 15%Al_2O_3	155	182	180	238
6061 20%Al_2O_3	164	199	191	242
6261	134	-	148	-
7017	121	-	159	-
7075	132	-	173	-

Table A.16 Slurry erosion rates of the aluminium alloys.

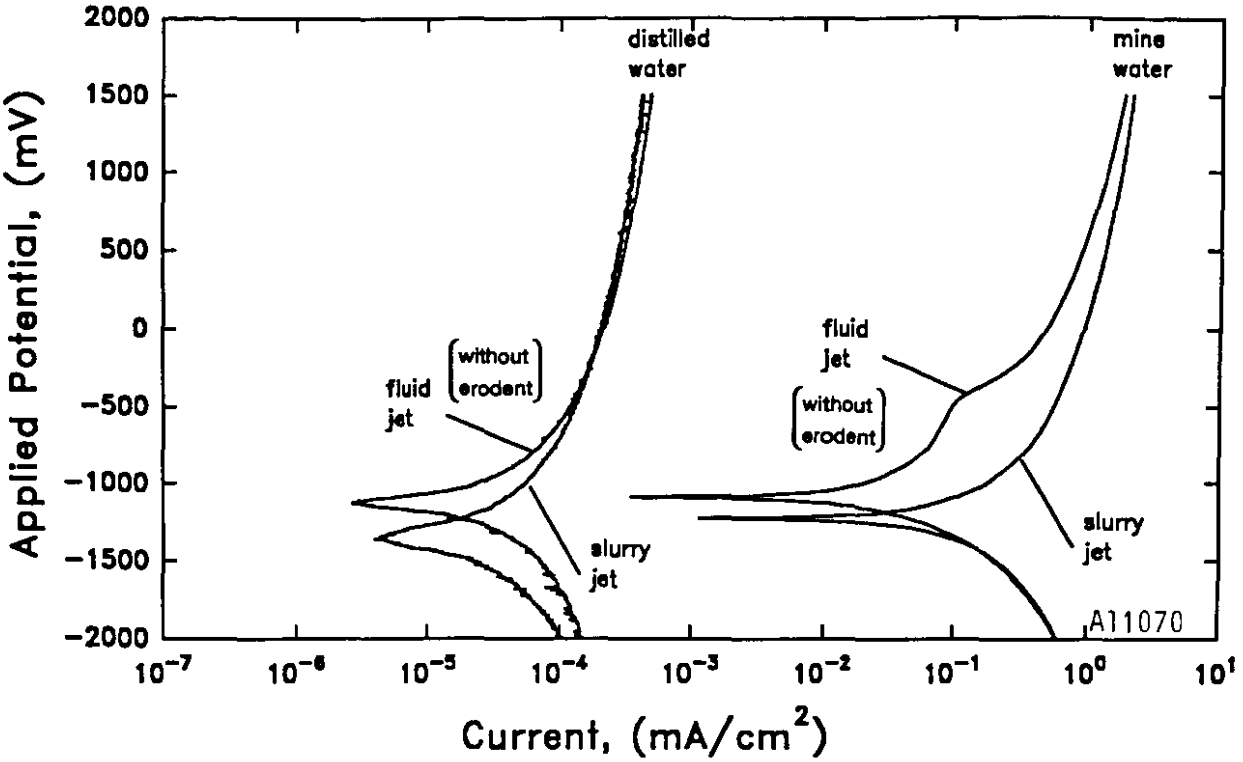

Figure A.17 Al1070 - graphs of the current density *vs.* potential scans: erodent, silica sand (500 μm); carrier fluid, distilled water and synthetic mine water(pH 5.7); temperature, 55°C; impact angle, 90°; impact velocity, 11 m/s; rate of polarisation 4mV/sec.

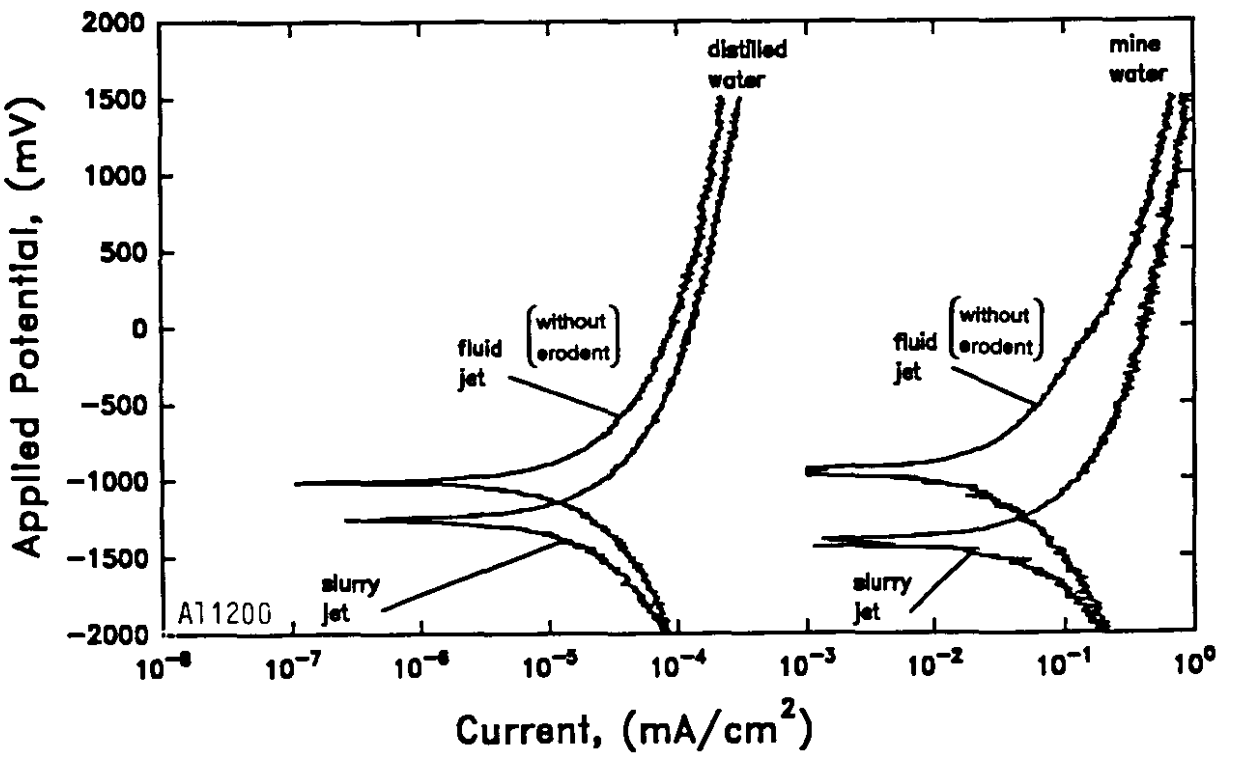

Figure A.18 Al1200 - graphs of the current density *vs.* potential scans: erodent, silica sand (500 μm); carrier fluid, distilled water and synthetic mine water(pH 5.7); temperature, 55°C; impact angle, 90°; impact velocity, 11 m/s; rate of polarisation 4mV/sec.

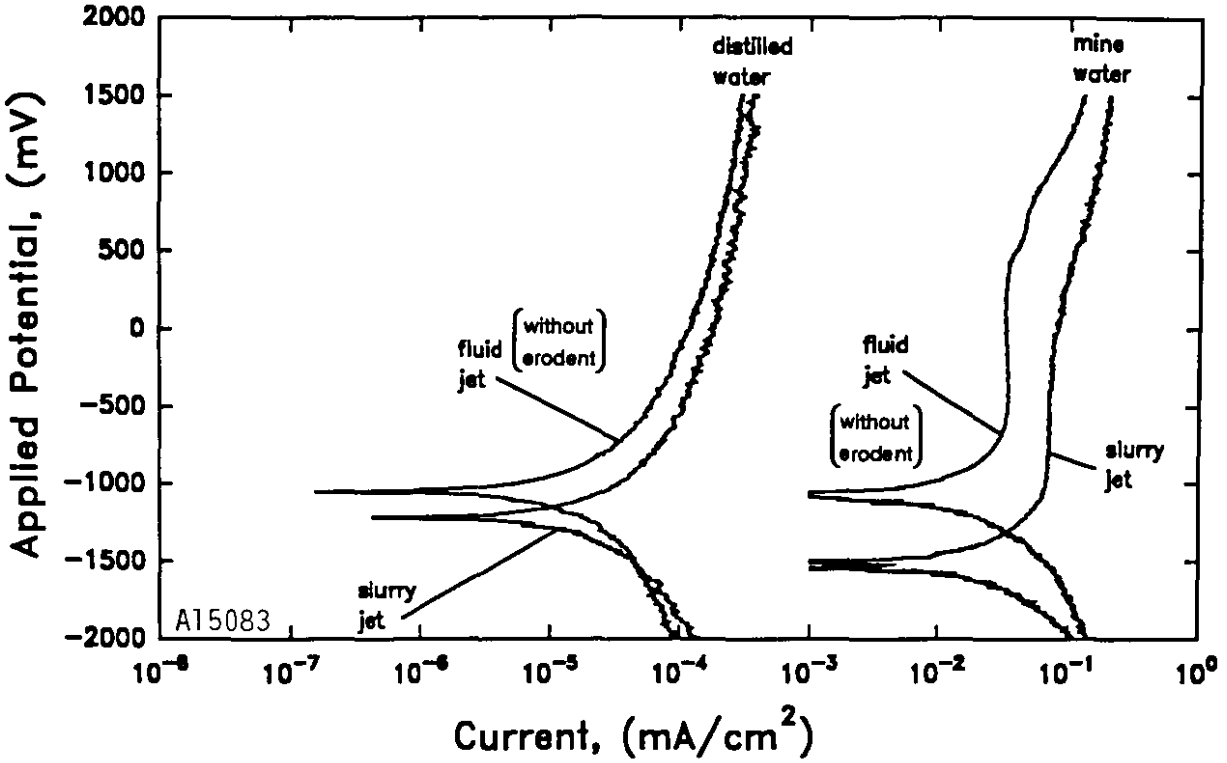

Figure A.19 Al5083 - graphs of the current density *vs.* potential scans: erodent, silica sand (500 μm); carrier fluid, distilled water and synthetic mine water(pH 5.7); temperature, 55°C; impact angle, 90°; impact velocity, 11 m/s; rate of polarisation 4mV/sec.

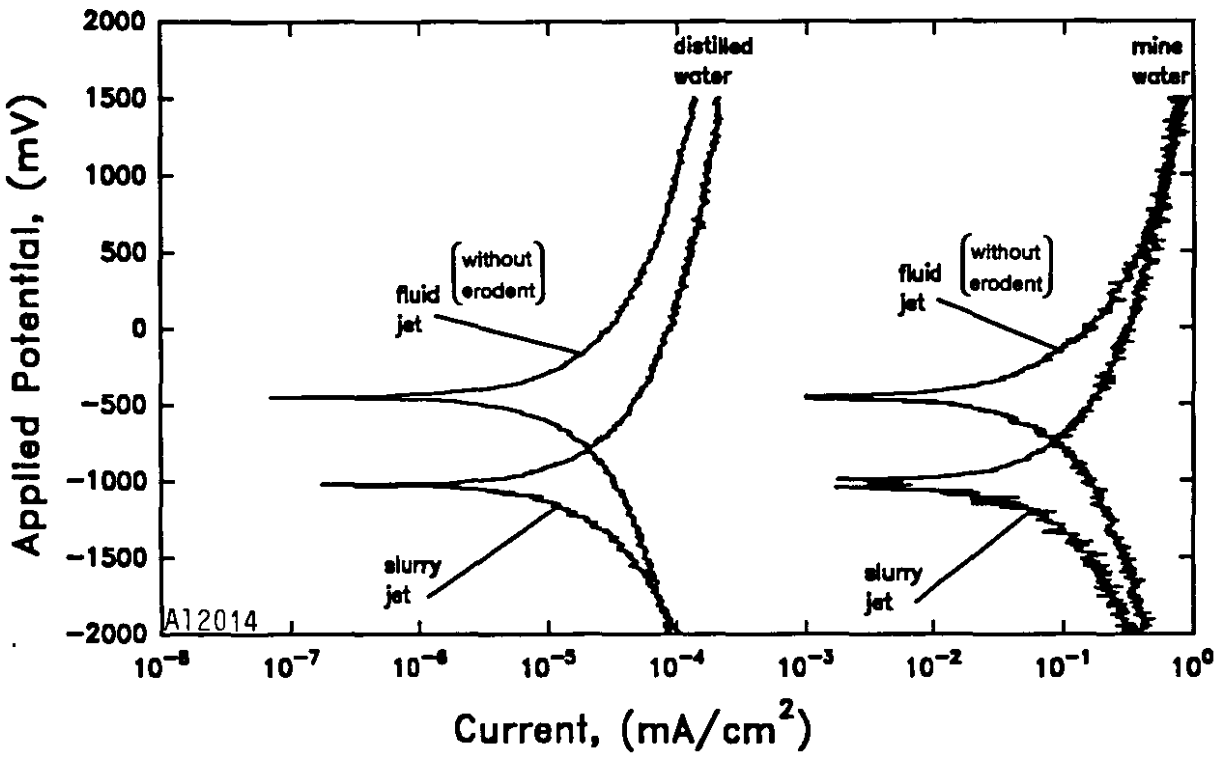

Figure A.20 Al2014 - graphs of the current density *vs.* potential scans: erodent, silica sand (500 μm); carrier fluid, distilled water and synthetic mine water(pH 5.7); temperature, 55°C; impact angle, 90°; impact velocity, 11 m/s; rate of polarisation 4mV/sec.

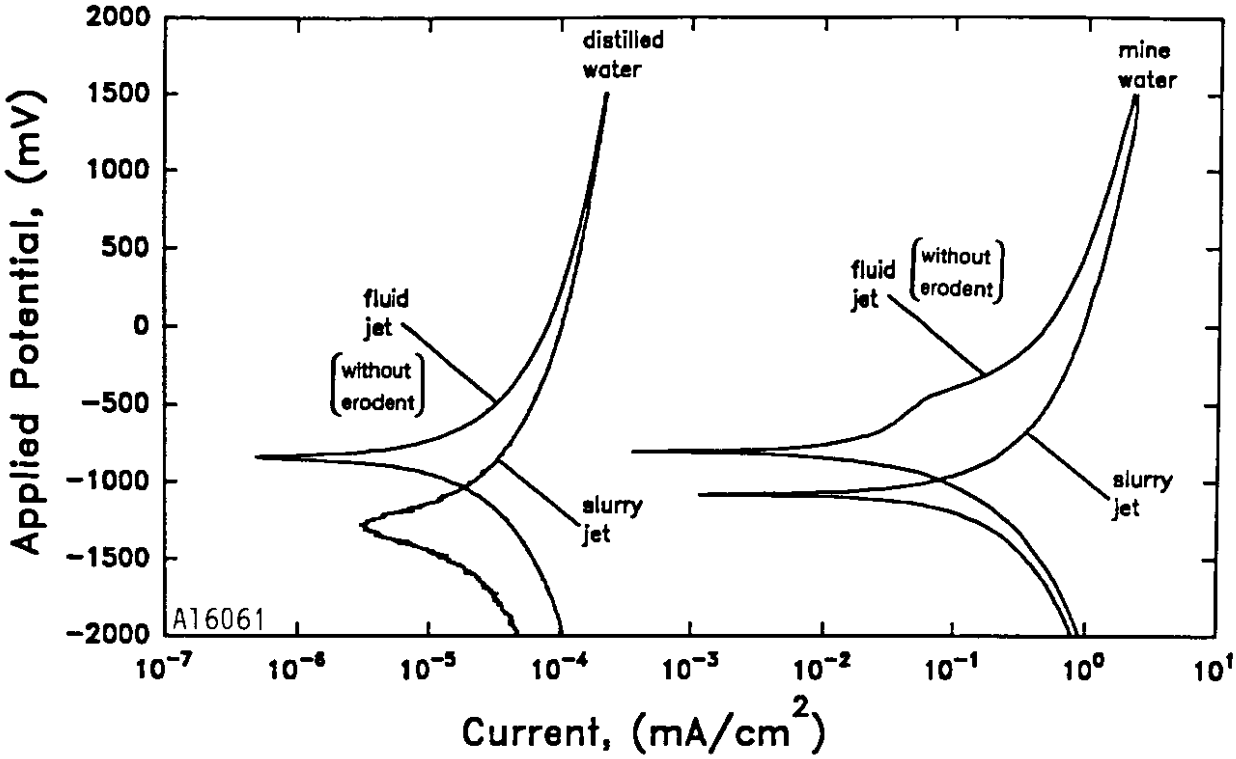

Figure A.21 Al6061 - graphs of the current density *vs.* potential scans: erodent, silica sand (500 μm); carrier fluid, distilled water and synthetic mine water(pH 5.7); temperature, 55°C; impact angle, 90°; impact velocity, 11 m/s; rate of polarisation 4mV/sec.

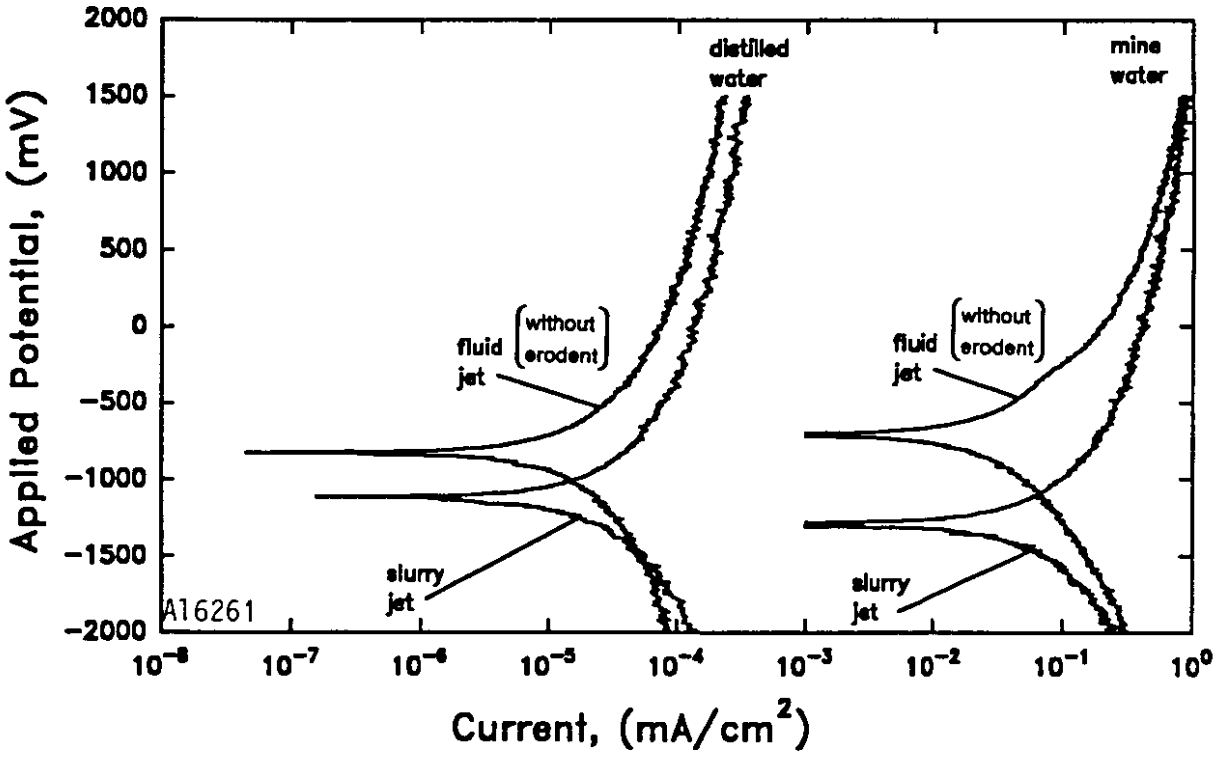

Figure A.22 Al6261 - graphs of the current density *vs.* potential scans: erodent, silica sand (500 μm); carrier fluid, distilled water and synthetic mine water(pH 5.7); temperature, 55°C; impact angle, 90°; impact velocity, 11 m/s; rate of polarisation 4mV/sec.

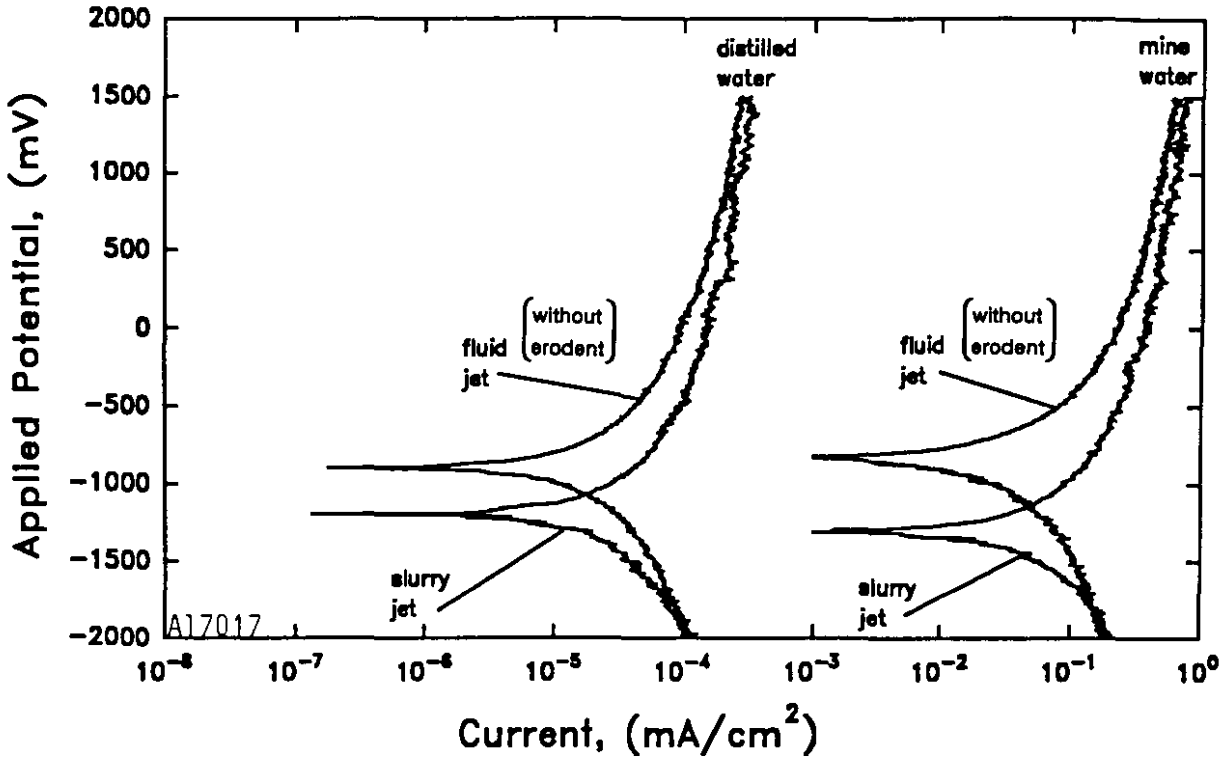

Figure A.23 Al7017 - graphs of the current density *vs.* potential scans: erodent, silica sand (500 μm); carrier fluid, distilled water and synthetic mine water(pH 5.7); temperature, 55°C; impact angle, 90°; impact velocity, 11 m/s; rate of polarisation 4mV/sec.

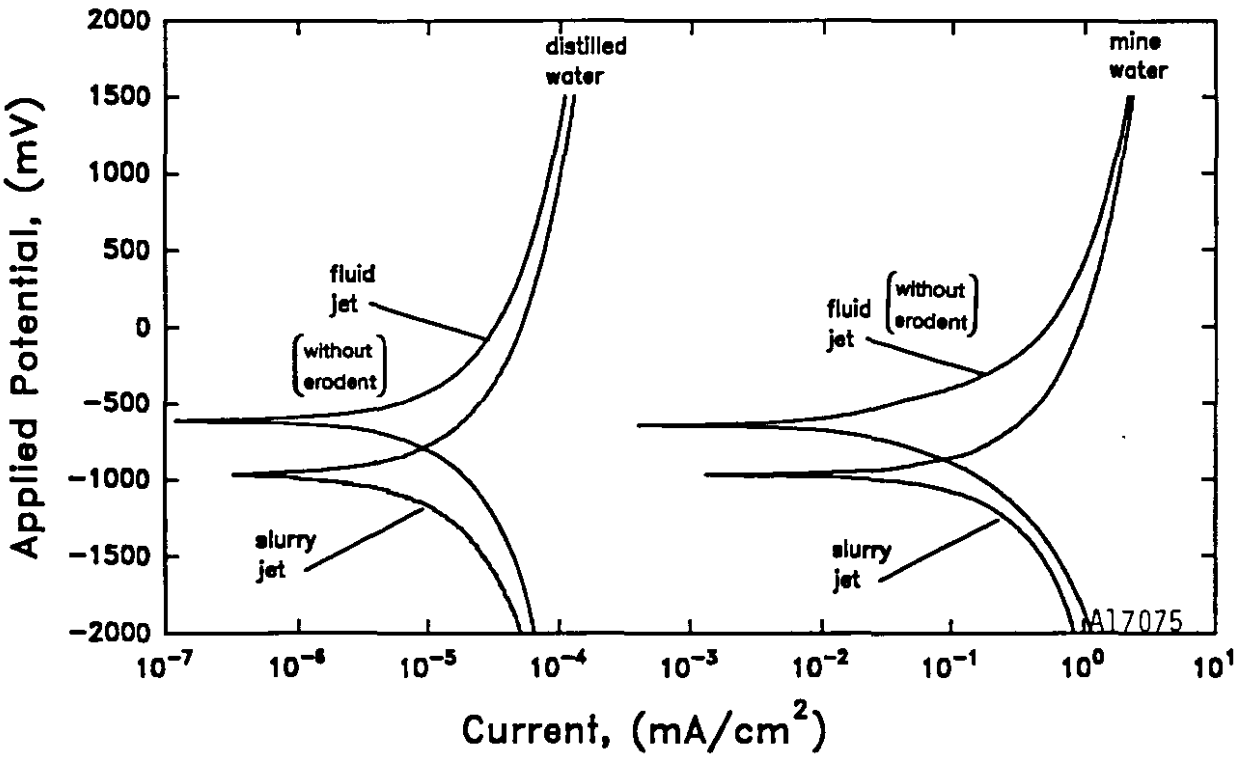

Figure A.24 Al7075 - graphs of the current density *vs.* potential scans: erodent, silica sand (500 μm); carrier fluid, distilled water and synthetic mine water(pH 5.7); temperature, 55°C; impact angle, 90°; impact velocity, 11 m/s; rate of polarisation 4mV/sec.

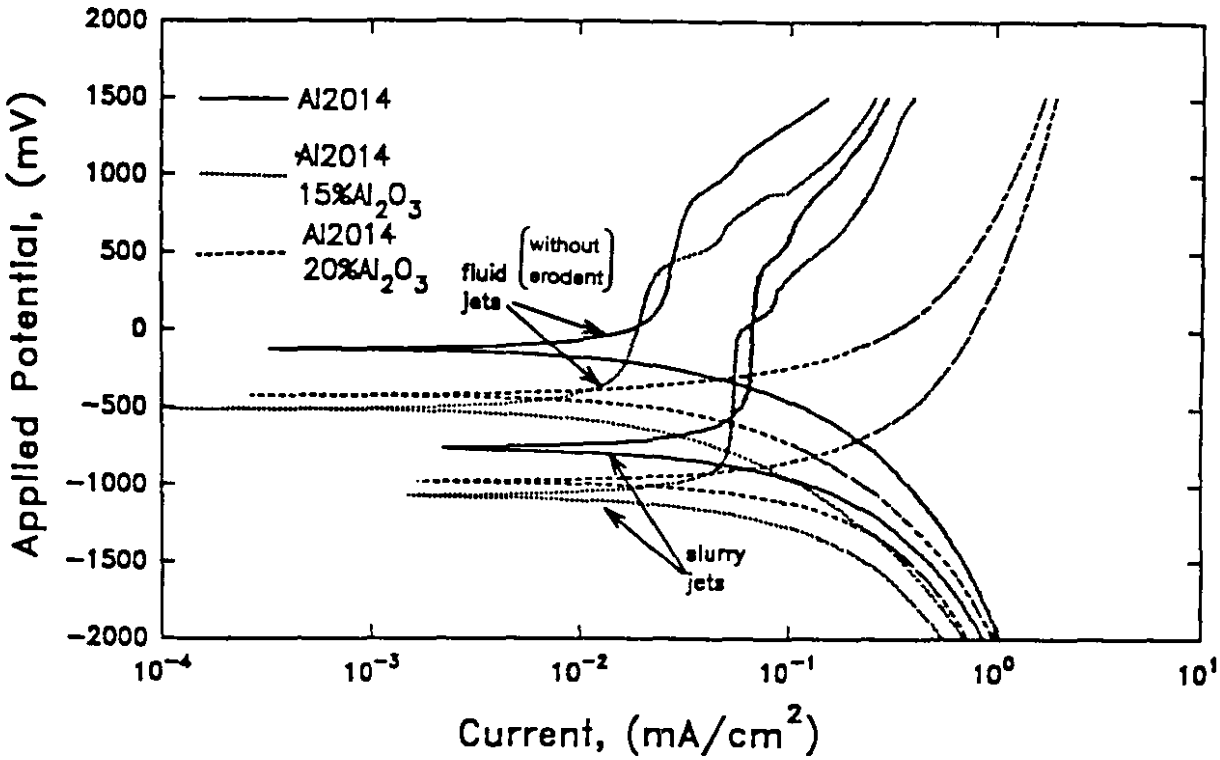

Figure A.25 Graphs of the current density *vs.* potential scans of the 2014 aluminium matrix alloy and the Al2014 MMCs. Tested at an impact angle of 90°: erodent, silica sand (500 μm); carrier fluid, synthetic mine water(pH 5.7); temperature, 55°C; impact velocity, 11 m/s; rate of polarisation 4mV/sec.

ALLOY	Density (g/cm^3)	Hardness (HV30)	Erosion rate (mg/hour)			Corrosion rate (mg/hour)
			Distilled water	Synthetic mine water	Cathodic protection	
3CR12	7.61	184	22.54	29.34	26.47	0.00
431SS	7.7	283	24.76	28.64	25.37	0.04
304SS	7.9	142	14.74	20.82	19.09	0.00
EN3B	7.82	282	30.28	34.20	30.60	2.41
EN8 Spheroidised	7.76	291	25.79	28.38	23.56	1.30
EN8 Tempered	7.76	493	20.95	23.28	20.93	1.22
EN8 Quenched	7.76	610	16.62	18.44	16.41	1.32

Table A.25 Results of the experimental work performed on the steels.

ALLOY	Erosion rate (mm^3/hour)			Corrosion rate (mm^3/hour)
	Distilled water	Synthetic mine water	Cathodic protection	
3CR12	43.24	56.28	50.78	0.00
431SS	46.94	54.30	48.10	0.08
304SS	27.24	38.47	35.28	0.00
EN3B	56.53	63.85	57.12	4.50
EN8 Spheroidised	48.52	53.39	44.32	2.45
EN8 Tempered	39.41	43.80	39.37	2.30
EN8 Quenched	31.27	34.69	30.87	2.48

Table A.26 Slurry erosion rates of the steels.

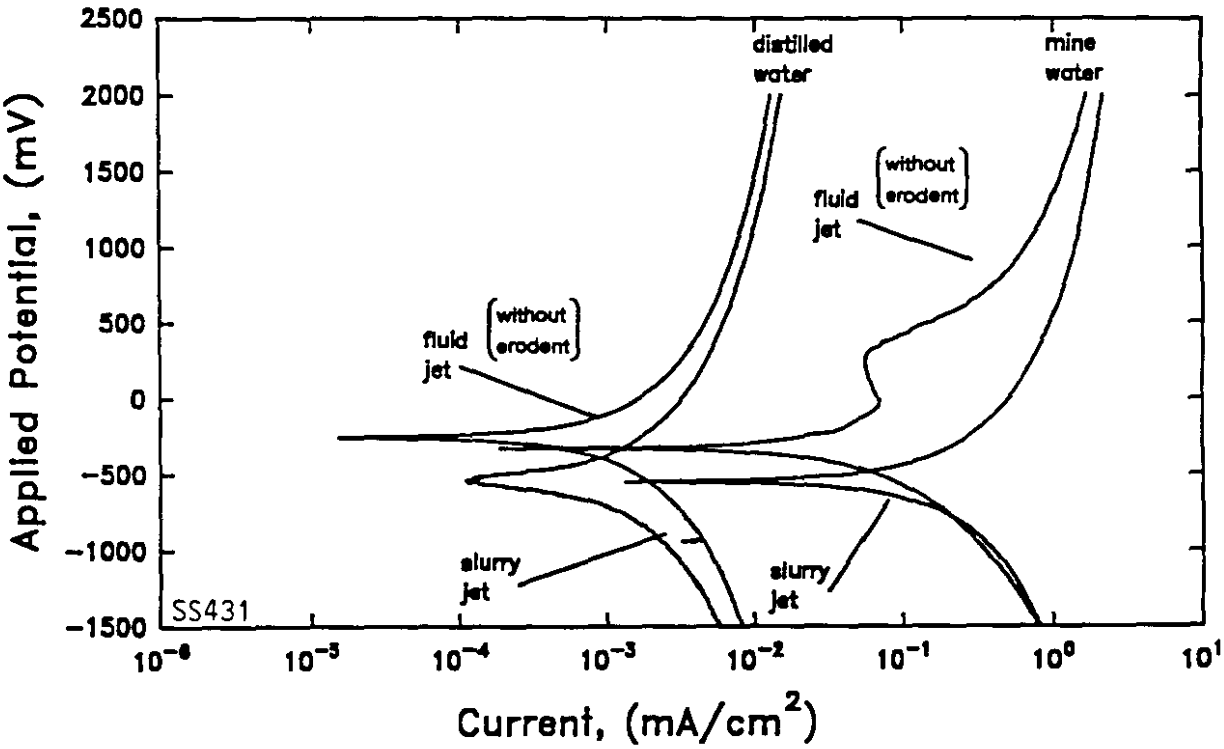

Figure A.27 431SS - graphs of the current density *vs.* potential scans: Erodent, silica sand (500 μm); carrier fluid, distilled water and synthetic mine water(pH 5.7); temperature, 55°C; impact angle, 90°; impact velocity, 11 m/s; rate of polarisation 4mV/sec.

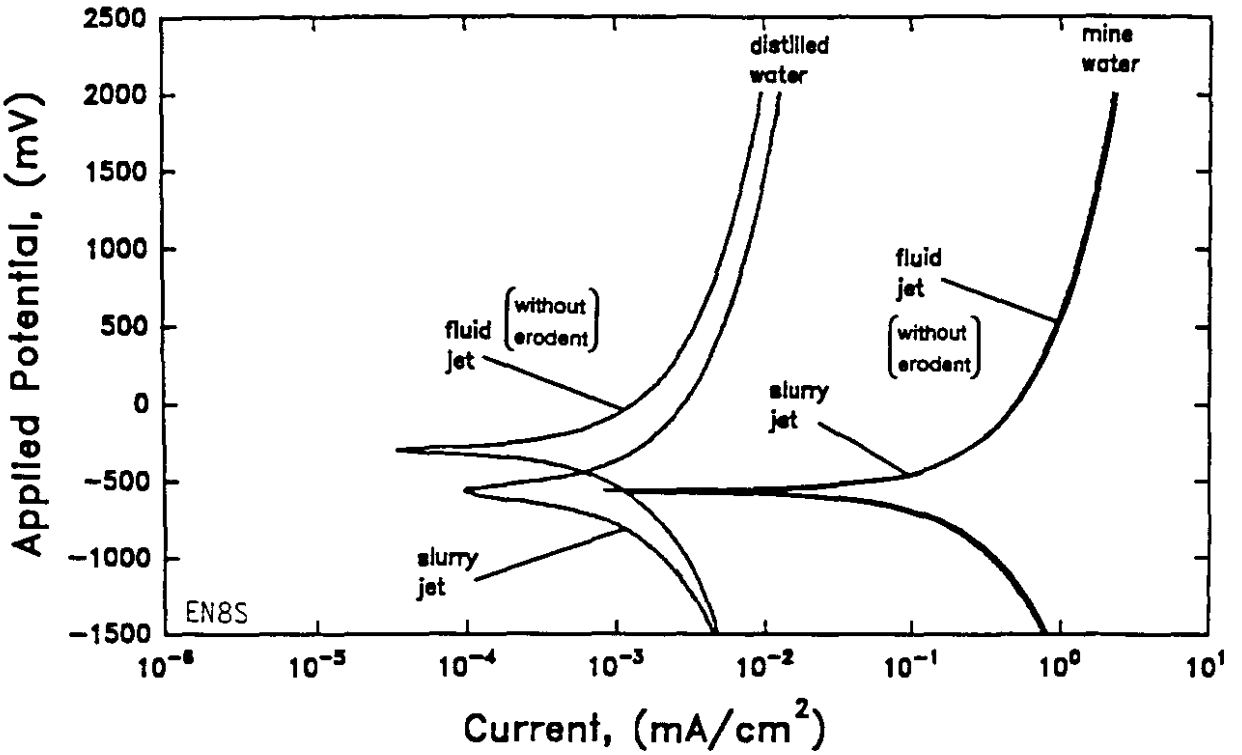

Figure A.28 EN8 spheroidised - graphs of the current density *vs.* potential scans: erodent, silica sand (500 μm); carrier fluid, distilled water and synthetic mine water(pH 5.7); temperature, 55°C; impact angle, 90°; impact velocity, 11 m/s; rate of polarisation 4mV/sec.

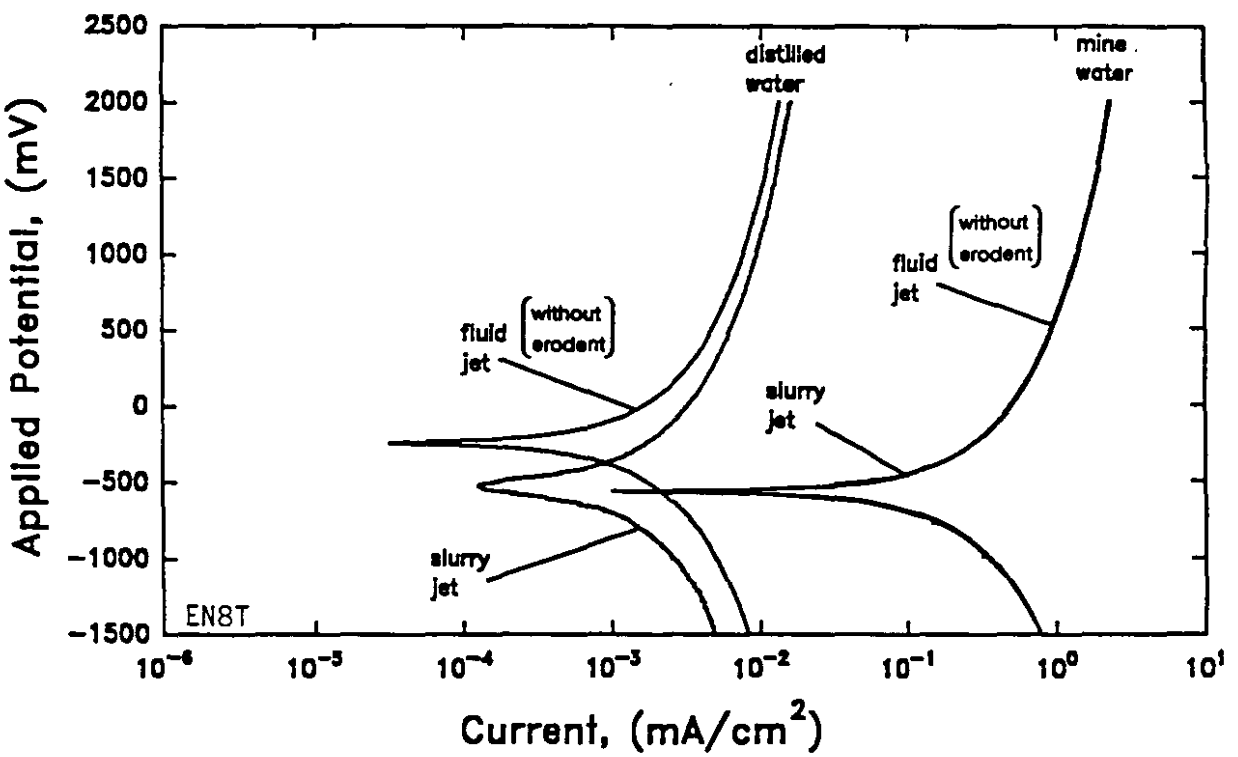

Figure A.29 EN8 tempered - graphs of the current density *vs.* potential scans: erodent, silica sand (500 μm); carrier fluid, distilled water and synthetic mine water(pH 5.7); temperature, 55°C; impact angle, 90°; impact velocity, 11 m/s; rate of polarisation 4mV/sec.

The time between impacts on the same spot is been estimated in the calculation below:

$$\frac{\text{number of impacts to damage entire surface}}{\text{number of impacts per second}}$$

= time between impacts, in seconds.

The following symbols and units have been adopted:

$\varnothing_n$ = ejector nozzle diameter (mm), eroded area ≈ slurry jet cross section
$\varnothing_i$ = diameter of impact site (μm), from figs 5.9(a)-5.10(a)
E_f = 'erodent flow rate' (kg/hour), calculated from slurry concentration
ρ_e = erodent density (kg/m^3), see Appendix, Table A.5
$\varnothing_e$ = erodent particle diameter (mm), see Appendix, Table A.5

number of impacts to damage surface:

$$= \frac{\text{area of damage on specimen}}{\text{area of one impact site}}$$

$$= \frac{\pi(\tfrac{1}{2}\varnothing_n)^2}{\pi(\tfrac{1}{2}\varnothing_i)^2} \qquad \text{(A.1)}$$

number of impacts per second:

$$= \frac{\text{volume of erodent impacting surface per second}}{\text{volume of one erodent particle}}$$

$$= \frac{E_f/\rho_e \cdot 60 \cdot 60}{{}^4/_3\pi(\varnothing_e/2)^3} \quad (s^{-1}) \qquad \text{(A.2)}$$

Combining equations A.1 and A.2,

= time between impacts, in seconds

$$= \frac{\pi(\tfrac{1}{2}\varnothing_n)^2 \cdot {}^4/_3\pi(\varnothing_e/2)^3}{\pi(\tfrac{1}{2}\varnothing_i/2)^2 \cdot E_f/\rho_e \cdot 60 \cdot 60} \quad (s) \qquad \text{(A.3)}$$

$$= \frac{\pi\,(5.5/2)^2 \cdot {}^4/_3\pi\,(0.50/2)^3}{\pi(50/2)^2 \cdot 68.5/2564 \cdot 60 \cdot 60} \times 10^{-3}\ s$$

= 0.1 second

TERMS AND DEFINITIONS

Terms which are relative to this thesis are listed alphabetically below. The following terminology is based on the Standard Terminology Relating to WEAR AND EROSION from ASTM Designation: G40-83[172].

angle of incidence/attack/impingement -- the angle between the direction of motion of an impinging liquid or solid particle and the tangent to the surface at the point of impact.

carrier fluid -- fluid medium that transports the impinging solid/erodent and that gives the particles their momentum relative to the solid surface on which they are impinging.

cumulative erosion-time curve -- a plot of cumulative erosion versus cumulative exposure duration.

erosion -- progressive loss of original material from a solid surface due to mechanical interaction between that surface and a fluid, a multicomponent fluid, or impinging liquid or solid particles.

erosion rate -- any determination of the rate of loss of material (erosion) with exposure duration.

incubation -- the initial stage of the erosion rate-time pattern during which the erosion rate is zero (or even negative) or negligible compared to the later stages of erosion.

particle concentration -- a measure of the solid particle content (by mass) in a mixture of particles and fluid.

The following terminology is based on Standard Definitions of Terms Relating to CORROSION AND CORROSION TESTING from ASTM Designation: G15-86 [172].

active-passive cell -- a corrosion cell in which the anode is a metal in the active state and the cathode is the same metal in the passive state.

anode -- the electrode of an electrolytic cell at which oxidation is the principal reaction.

cathode -- the electrode of an electrolytic cell at which reduction is the primary reaction.

cathodic protection -- a technique to reduce the corrosion rate of a metal surface by making it the cathode of an electrochemical cell.

corrosion fatigue -- the process in which a metal fractures prematurely under conditions of simultaneous corrosion and repeated cyclic loading at lower stress levels or fewer cycles than would be required in the absence of the corrosive environment.

corrosion potential -- the potential of a corroding surface in an electrolyte relative to a reference electrode measured under open-circuit conditions.

current density -- the current flowing to or from a unit area of an electrode surface.

electrochemical cell -- an electrochemical system consisting of an anode and a cathode in metallic contact and immersed in electrolyte. The anode and cathode may be dissimilar areas on the same metal surface.

impressed current -- an electric current supplied by a device employing a power source that is external to the electrode system, such as the d-c current for cathodic protection.

local corrosion cell -- an electrochemical cell created on a metal surface because of a difference in potential between adjacent areas on the surface.

open-circuit potential -- the potential of an electrode measured with respect to a reference electrode or another electrode when no current flows to or from it.

polarization -- the change from the open-circuit electrode potential as the result of the passage of current.

potentiodynamic -- the technique for varying the potential of an electrode in a continuous manner at a preset rate.

Tafel slope -- the slope of the straight line portion of a polarization curve.